HIGH-TEMPERATURE STEAM AND PRESSURISED WATER CORROSION BEHAVIOURS OF NITRIDE CERAMIC COATINGS FOR ACCIDENT TOLERANT FUEL CLADDINGS

A thesis submitted to The University of Manchester for the degree of

Master of Philosophy

in the Faculty of Science and Engineering

2019

Xi YU

School of Materials

List of contents

List of contents *1*

List of figures *4*

List of tables *10*

Abstract *11*

Declaration *12*

Copyright statement *13*

Acknowledgement *14*

Introduction *15*

Aim & Objectives *16*

1. Background and literature review *18*

1.1. Overview of nuclear energy **18**

1.2. Overview of Zirconium fuel claddings **18**

1.2.1. Requirements and developments of fuel cladding materials 18

1.2.2. Development of zirconium claddings 20

1.2.3. Problems with Zirconium cladding 22

1.2.3.1. Corrosion mechanism under PWR 23

1.2.3.2. Hydrogen embrittlement 27

1.2.3.3. The control factors of corrosion 30

1.2.3.4. High-temperature corrosion by steam 31

1.2.3.5. Steam oxidation mechanism 35

1.3. Development of ATF **38**

1.3.1. Requirements for ATF 38

1.3.2. Potential ATF designs and problems 41

1.3.2.1. Complete replacement of Zr claddings 41

1.3.2.2. Protective coating system 43

1.3.2.2.1. Zr-containing coatings 43

1.3.2.2.2. Aluminium and chromium coatings 44

1.3.2.2.3. Silicon coatings 46

1.4. Coating materials selection for ATF design....47

1.4.1. Transition metal nitride coatings....47

1.4.2. Nano-composite TiN based coatings....48

1.4.2.1. Morphology of TiSiN and TiAlN....48

1.4.2.2. Corrosion resistance of TiSiN and TiAlN....49

1.4.3. Interlayer Double layer structure....50

1.4.4. Coating deposition technique....51

2. Experimental procedures....58

2.1. Substrate preparation....58

2.2. Magnetron sputtering process....59

2.3. Simulated LOCA steam test and PWR Corrosion test....60

2.4. Characterisation....62

2.4.1. GIXRD phase characterisation....62

2.4.2. Microstructure and element characterisation....63

3. Results and discussion....64

3.1. Characterisation of as-deposited nitride coatings....65

3.1.1. Phase identification....65

3.1.2. Composition and microstructure characterisation....68

3.2. High-temperature steam oxidation....74

3.2.1. Macro-surface analysis and compositional analysis....75

3.2.2. 600°C steam oxidation characterisation....76

3.2.2.1. Phase identification....76

3.2.2.2. Surface and cross-section analysis of ZrN....79

3.2.2.3. Surface and cross-section analysis of $TiSi_xN$/Ti....80

3.2.3. 800°C steam oxidation characterisation....84

3.2.3.1. Phase identification....84

3.2.3.2. Surface morphology and elemental analysis....86

3.2.3.3. Cross-section and Oxidation kinetics....87

3.2.4. 1000°C steam oxidation characterisation....92

3.2.4.1. Phase identification....92
3.2.4.2. Surface morphology and elemental analysis....94
3.2.4.3. Oxidation kinetics....95
3.2.5. Summary....101
3.3. Corrosion behaviour in autoclave....102
3.3.1. Corrosion behaviour of ZrN....102
3.3.2. Corrosion behaviour of TiN and TiSiN....105
3.3.3. Autoclave corrosion behaviour of $TiSi_xN$/Ti bilayer coating....106
3.3.3.1. Phase identification....106
3.3.3.2. Morphology and elemental analysis after 2 days autoclave test....108
3.3.3.3. Morphology and elemental analysis after 2 days autoclave test....112
3.3.3.4. Coating thickness change due to corrosion....114
3.4. Corrosion mechanism....115
4. Conclusion....117
5. Future work....119
Reference....121

Final word count: 33385 words.

List of figures

Figure 1-1 The nuclear fuel assembly of a typical pressurised water reactor (PWR). 20

Figure 1-2 The schematic of the cross-section of the Zircaloy cladding tub. 20

Figure 1-3 Schematic shows the corrosion mechanism in the water-Zr alloy system.24

Figure 1-4 Measured corrosion rate fitted with power-law of the pre-transition stage of the ZIRLO sheet alloy.....25

Figure 1-5 Oxide growth structure schematic of Zy-4 alloy after PWR simulation [44]25

Figure 1-6 Schematics of typical corrosion transition processes of zirconium alloys..26

Figure 1-7 Periodic oxide layers in AXIOM X1 at 70GWD/MTU [27]. 26

Figure 1-8 Hydrogen pickup of Zy-4 and M5[64].....29

Figure 1-9 Phase diagram of Zr-H system at low hydrogen concentration[65] 29

Figure 1-10 Burnup dependence of oxide thickness for Zircaloy-4 and M5. [27].....31

Figure 1-11 Oxide thickness along the axial direction of zirconium alloy fuel rods[27], [72]. 31

Figure 1-12 Schematic of zirconium cladding temperature during LOCA 32

Figure 1-13 Surface condition of Zy-702 tube after 1hour steam oxidation treatment at 1000°C 34

Figure 1-14 Optical micrographs of the cross-section of Zircaloy BWR cladding specimen oxidised at 1200 for 2h in 1MPa steam[13].....35

Figure 1-15 Unirradiated Zy-2 after 600 seconds steam oxidation test at 1200°C[35]35

Figure 1-16 Schematics of vacancy cluster dynamics[81] 36

Figure 1-17 Schematic of the atomic processes in the oxidation of NiCr alloy in water vapour, illustrating at the atomic level that water vapour enhances vacancy formation and promotes vacancy clustering. [81].....36

Figure 1-18 DFT calculation results of vacancy formation energy and vacancy pairing energy with and without the presence of $Hi^{\bullet}$. (a) shows that vacancy formation energy decreases by 2.83 eV in the presence of $Hi^{\bullet}$. (b) shows that in NiO two separated Ni vacancies repel each other due to the positive energy of 0.36 eV; while the vacancies merge to form clusters with the presence of $Hi^{\bullet}$ due to the pairing energy decrease to -0.34eV. [81] 36

Figure 1-19 Identification of the important attributes of the ATF system design. 40

Figure 1-20 Cross-section micrographs of (a) Zircaloy 2 (b) Fe-25Cr and (c) PM2000 after exposure for 8 h in 1 MPa 1200°C steam [77] 43

Figure 1-21 STEM cross-sectional images of CrAl coatings after 20 hours HTS exposure under 700°C, layers of Cr_2O_3 and Al_2O_3 were observed associated with pores. A layer of intermetallic was formed between CrAl coatings and Zy-2 substrate 46

Figure 1-22 Reflected light optical micrographs of the oxides formed on the Cr-coated Zircaloy-4 in 1200°C steam for 2000 s [114]. 46

Figure 1-23 Cross-sectional TEM image of the oxide double-layer formed on a Ti-Al-N film after 800°C for 5-h [15] 50

Figure 1-24 SEM images of the cross-section tube after SCW test [141] 50

Figure 1-25 (a) Three fundamental steps of the PVD process and (b) schematics of the PVD sputtering process.....53

Figure 1-26 Schematics of a closed-field unbalanced magnetron sputtering deposition and the charged particles movement illustration. 57

Figure 2-1 Experimental arrangement for the steam test, with steam generation system, heating system and steam & gas cooling system 61

Figure 2-2 (a) High temperature and pressure Vessel Model 4651, 250mL with VGR and Thermocouple and (b) with 4923 Heater.....62

Figure 3-1 GIXRD patterns with incidence angle 2°of as-deposited ZrN coating with Zr substrate, TiN and $TiSi_xN$ coatings with Si wafer substrate 66

Figure 3-2 GIXRD patterns of the bare substrate and as-deposited $TiSi_xN$/Ti coatings with Zy-4 substrate 67

Figure 3-3 Cross-section SEM images of the as-deposited (a) ZrN coating on Zr-Nb alloy substrate and (b)TiN coating on a silicon wafer 68

Figure 3-4 SEM images (SE mode) of as-deposited (a) $TiSi_{0.08}N$, (b) $TiSi_{0.13}N$ and (c) $TiSi_{0.19}N$ coatings surface morphology, the white particles are $TiSi_xN$ droplets. 68

Figure 3-5 SEM images (BSE mode) of as-deposited (a) $TiSi_{0.08}N$, (b) $TiSi_{0.13}N$ and $TiSi_{0.19}N$ coatings surface morphology 69

Figure 3-6 AFM height images (left) and 3D topography images (right) of as-deposited (a) $TiSi_{0.08}N$, (b) $TiSi_{0.13}N$ and (c) $TiSi_{0.19}N$ coatings with scan area 10μm by 10μm. ..71

Figure 3-7 SEM images of as-deposited cross-section (a_1)$TiSi_{0.08}N$, (b) $TiSi_{013}N$ and (c) $TiSi_{0.19}N$ coatings with Ti-interlayer on Zy-4 alloy substrate and (a_2)EDS mapping of $TiSi_{0.08}N$. 73

Figure 3-8 Macro-surface morphology of ZrN after 1-hour steam test at 800°C 75

Figure 3-9 4 hours of steam tested surface morphology SEM images of (a) $TiSi_{0.08}N$, (b) $TiSi_{0.13}N$, (c) $TiSi_{0.19}N$ at 600°C, (d) $TiSi_{0.08}N$, (e) $TiSi_{0.13}N$, (f) $TiSi_{0.19}N$ at 800°C and (g) $TiSi_{0.08}N$, (h) $TiSi_{0.13}N$, (i) $TiSi_{0.19}N$ at 1000°C 76

Figure 3-10 GIXRD patterns with X-ray incident angle 2° (a) from 25° to 60° and (b) from 32° to 38° of single-side-polished bare Zy-4 bulk (grey curve) and ZrN coating on zirconium alloy substrate (orange curve) after 1h 600°C steam test, and $TiSi_{0.08}N$ (red curves), $TiSi_{0.13}N$ (blue curves) and $TiSi_{0.19}N$ (green curves) coatings with Zy-4 substrate after 1h, 2h and 4h steam test at 600°C(M-ZrO_2=Monoclinic Zirconium Oxide; A-TiO_2=Anatase;) 77

Figure 3-11 Surface SEM SE images of remain attached ZrN coating after 1 hour 600°C steam test 79

Figure 3-12 Cross-section SEM BSE images of ZrN samples after 1 hour 600°C steam test (a) with ZrN coating attached (b) ZrN coating spalled area 80

Figure 3-13 Cross-section SEM images and EDS elemental mapping of (a) ZrN coating on Zr substrate (b) ZrN coating spalled area after 1-hour steam test at 600°C 80

Figure 3-14 High magnification images (50000x) of $TiSi_{0.08}N$, $TiSi_{0.13}N$ and $TiSi_{0.19}N$ coating surface morphology after 1h, 2h, and 4h steam tests at 600°C 81

Figure 3-15 Cross-section SEM images of polished Zy-4 substrate after 600°C steam test 82

Figure 3-16 Cross-section SEM images in BSE mode of $TiSi_{0.08}N$/Ti after (a)1 hour, (b) 2 hours and (c) 4 hours, $TiSi_{0.13}N$/Ti after (d)1 hour, (e) 2 hours and (f) 4 hours and $TiSi_{0.19}N$/Ti after (g) 1 hour, (h) 2 hours and (i) 4 hours steam test at 600°C 83

Figure 3-17 GIXRD patterns with incident angle 2° of single-side-polished bare Zy-4 bulk and ZrN coating on zirconium alloy substrate after 1h 800°C steam test, and $TiSi_xN$/Ti coatings with Zy-4 substrate after 1h, 2h and 4h 800°C steam test. (M-ZrO_2=Monoclinic Zirconium Oxide; T-ZrO_2=Tetragonal Zirconium Oxide; A-TiO_2=Anatase; R-TiO_2=Rutile) 84

Figure 3-18 High magnification images (50000x) of $TiSi_{0.08}N$, $TiSi_{0.13}N$ and $TiSi_{0.19}N$ surface morphology after 1h, 2h, and 4h steam tests at 800°C 87

Figure 3-19 Macro-observation of $TiSi_{0.08}N$ samples after (a) 1 hour, (b) 2 hours and (c) 4 hours steam test at 800°C 88

Figure 3-20 Lower magnification of cross-section SEM images of (a) $TiSi_{0.08}N$, (b) $TiSi_{0.13}N$ and (c) $TiSi_{0.19}N$ after 1 hour 800°C steam test, with vertical cracks within the coating and lateral cracks within ZrO2 layer along with the oxide and un-corroded Zr interface 89

Figure 3-21 Cross-section SEM images in BSE mode and EDS mappings of $TiSi_{0.08}N$ after (a) 1 hour, (b) 2 hours and (c) 4 hours steam tests at 800°C.....90

Figure 3-22 Cross-section SEM images in BSE mode of $TiSi_{0.08}N$, $TiSi_{0.13}N$ and $TiSi_{0.19}N$ after 1 and 2 hour 800°C steam test and enlarged area EDS mapping.....91

Figure 3-23 GIXRD patterns with incident angle 2° of single-side-polished bare Zy-4 bulk after 1h 1000°C steam test, and TiSiN coatings with Zy-4 substrate after 1h, 2h and 4h 1000°C steam test.....93

Figure 3-24 High magnification images (50000x) of $TiSi_{0.08}N$/Ti, $TiSi_{0.13}N$/Ti and $TiSi_{0.19}N$/Ti coating surface morphology after 1h, 2h, and 4h steam tests at and 1000°C 95

Figure 3-25 Cross-section SEM images in BSE mode of (a) $TiSi_{0.08}N$/Ti, (b) $TiSi_{0.13}N$/Ti and (c) $TiSi_{0.19}N$/Ti after 2 hours 1000°C steam test, the red squares marked as EDS mapping area in Figure 3-26(b), Figure 3-27(b), and Figure 3-28(b) 96

Figure 3-26 Cross-section EDS mappings of $TiSi_{0.08}N$/Ti coatings after (a) 1h and (b) 2h steam test at 1000°C.....97

Figure 3-27 Cross-section EDS mapping of $TiSi_{0.08}N$/Ti coatings after (a) 1 hour and (b) 2 hours steam test at 1000°C.....98

Figure 3-28 Cross-section SEM images in BSE mode and EDS mappings of $TiSi_{0.19}N$ after 1 and 2 hours 1000°C steam test.....99

Figure 3-29 Cross-section BSE images of $TiSi_xN$ coatings after 4 hours steam test at 1000°C 101

Figure 3-30 (a) Low magnification of surface morphology, high magnification of (b) surface shards (c) coating spalled off area of ZrN coating with Zr substrate after the 3-day autoclave test 103

Figure 3-31 SEM image of as-deposit coating cross-section (a) oxidised ZrN coating on Zr alloy substrate, (b) coating spalled substrate cross-section. 103

Figure 3-32 Cross-section EDS mapping image of 3-day autoclave tested ZrN coating on Zr substrate 103

Figure 3-33 (a) Low magnification surface morphology and (b) high magnification morphology of TiN coating with Si substrate after 3-day autoclave test.....105

Figure 3-34 Cross-section EDS mapping images of 3-day autoclave tested TiN coatings on Si substrate 105

Figure 3-35 Cross-section SEM image of 3-day autoclave tested TiSiN coatings on Si substrate.....105

Figure 3-36 Normalised GIXRD patterns of autoclave tested $TiSi_xN$ coating samples for 1 to 7 day, as-deposited and Zr substrate used as reference patterns. 107

Figure 3-37 Surface morphology of (a) $TiSi_{0.08}N$/Ti, (b) $TiSi_{0.13}N$/Ti and (c) $TiSi_{0.19}N$/Ti coatings after 2 days autoclave test conducted by SEM in SE mode 109

Figure 3-38 Cross-section image of (a) $TiSi_{0.08}N$/Ti, (b) $TiSi_{0.13}N$/Ti and (c) $TiSi_{0.19}N$/Ti coatings after 2 days autoclave test 109

Figure 3-39 SEM images of (a) $TiSi_{0.08}N$/Ti, (b) $TiSi_{0.13}N$/Ti and (c) $TiSi_{0.19}N$/Ti coatings fracture surface morphology after 2 days autoclave test.....110

Figure 3-40 Cross-section SEM images and EDS mappings of (a) $TiSi_{0.08}N$/Ti , (b) $TiSi_{0.13}N$/Ti and (c) $TiSi_{0.19}N$/Ti after 2 days autoclave immersion test 111

Figure 3-41 EDS line scan of 2 days autoclaved (a) $TiSi_{0.08}N$/Ti, (b) $TiSi_{0.13}N$/Ti and (c) $TiSi_{0.19}N$/Ti coatings.....112

Figure 3-42 SEM images of (a) $TiSi_{0.08}N$/Ti, (b) $TiSi_{0.13}N$/Ti and (c) $TiSi_{0.19}N$/Ti coating surface morphology after 7 days autoclave test.....112

Figure 3-43 SEM polished cross-section images of (a) $TiSi_{0.08}N$/Ti, (b) $TiSi_{0.13}N$/Ti and (c) $TiSi_{0.19}N$/Ti coating after 7 days autoclave test 113

Figure 3-44 Cross-section SEM images and EDS mappings of (a) $TiSi_{0.08}N$/Ti, (b) $TiSi_{0.13}N$/Ti and (c) $TiSi_{0.19}N$/Ti after 7 days autoclave test.....113

Figure 3-45 Thickness of TiSixN/Ti bilayer after autoclave immersion test.....114

List of tables

Table 1-1 Number of operational reactors by 31, DEC 2016 18

Table 1-2 Typical service conditions for zirconium cladding rods in PWRs [19], [20]. 19

Table 1-3 Chemical composition rage of Zirconium alloys [24]–[27].....21

Table 1-4 List of issues exist in Zr-claddings under designed normal and accident conditions[37], [38] 22

Table 1-5 Thermal expansion coefficient of materials [143].....51

Table 2-1 Chemical composition of Zircaloy-4 by weight percentage 58

Table 2-2 Magnetron sputtering parameters for $TiSi_xN$/Ti coatings 59

Table 3-1 As-deposited $TiSi_xN$/Ti coatings sample ID, chemical elemental composition (at %), thickness (μm) and roughness (nm) scanned by 10x10μm area and area without large droplets.....70

Abstract

A new coating design and material selection of accident tolerant fuel (ATF) claddings have been produced using magnetron sputtering (MS) technique. ZrN single layer and Ti(Si)N single layer coatings were successfully deposited with flat and dense morphology and good adhesion with a polished zirconium alloy plate and Si wafer. $TiSi_xN$/Ti (x=0.08, 0.13, 0.19) double layer structure coatings were deposited as two flat and dense layers bonded together well with a Zy-4 polished plate. To evaluate the corrosion behaviours of these coatings under accident scenarios and operational conditions, a high-temperature steam test (600°C, 800°C and 1000°C with Ar flow 0.4L/min and H_2O 90%) and autoclave immersion test (360°C, 19.7MPa) were conducted. Scanning electron microscopy (SEM) associated with energy-dispersive X-ray spectroscopy (EDS) were used for surface and microstructure analysis. X-ray diffraction (XRD) was conducted to evaluate the phase of coatings before and after corrosion tests.

Single layer ZrN coatings demonstrated significant spallation after steam and autoclave tests due to the large differences in thermal expansion coefficient between the ceramic layer and Zr substrate. The $TiSi_xN$/Ti double layer structure showed better adhesion with the underneath Zy-4 substrate following steam and autoclave tests.

The ZrN layer was fully oxidised after 1-hour 600°C steam test and two-day autoclave immersion. $TiSi_{(0.08,\ 0.13,\ 0.19)}N$/Ti coatings exhibited superior steam resistance up to 4 hours at 1000°C. The corrosion behaviour varied according to the Si content and exposure temperature. However, the corrosion behaviour against pressurised water showed a significant difference compared with water vapour. Only part of $TiSi_{0.08}N$ survived after a seven-day pressurised water immersion test at 360°C, 19.7MPa.

Under high-temperature (1000°C) steam, oxidation of TiSiN and Si-volatilization were the degradation mechanisms for the $TiSi_xN$ layer. However, oxidation of TiSiN and Si-dissolution were the mechanisms of corrosion when under pressurized water.

Declaration

I, Xi YU, solemnly declare: no portion of the work referred to in the thesis has been submitted in support of an application for another degree or qualification of this or any other university or other institute of learning.

Copyright statement

i. The author of this thesis (including any appendices and/or schedules to this thesis) owns certain copyright or related rights in it (the “Copyright”) and s/he has given The University of Manchester certain rights to use such Copyright, including for administrative purposes.

ii. Copies of this thesis, either in full or in extracts and whether in hard or electronic copy, may be made **only** in accordance with the Copyright, Designs and Patents Act 1988 (as amended) and regulations issued under it or, where appropriate, in accordance with licensing agreements which the University has from time to time. This page must form part of any such copies made.

iii. The ownership of certain Copyright, patents, designs, trademarks and other intellectual property (the “Intellectual Property”) and any reproductions of copyright works in the thesis, for example graphs and tables (“Reproductions”), which may be described in this thesis, may not be owned by the author and may be owned by third parties. Such Intellectual Property and Reproductions cannot and must not be made available for use without the prior written permission of the owner(s) of the relevant Intellectual Property and/or Reproductions.

iv. Further information on the conditions under which disclosure, publication and commercialisation of this thesis, the Copyright and any Intellectual Property and/or Reproductions described in it may take place is available in the University IP Policy (see http://documents.manchester.ac.uk/DocuInfo.aspx?DocID=24420), in any relevant Thesis restriction declarations deposited in the University Library, The University Library’s regulations (see http://www.library.manchester.ac.uk/about/regulations/) and in The University’s policy on Presentation of Theses.

Acknowledgement

I would like to express my grateful gratitude to Prof. Ping Xiao, my supervisor and mentor, who guided this work and helped me whenever he was needed. His invaluable support and guidance have helped me to come across the toughness and obstacles during my two years research period and life living in Manchester. His patience, tolerance and trust are my strongest support to accomplish this thesis.

Sincere thanks to the professors and technical staff in Materials Science Centre, Prof. Robert Freer, Dr. David Hall, Mrs. Olwen Richert, Mr. Andy Wallwork, Mr. Kenneth Gyves, Dr. John Warren, Mr. Gary Harrison, who gave technique guidance and administration service for making the study smooth and delightful. I would also like to thank Prof. Peter Kelly, Dr. Justyna Kulczyk-Malecka from Dalton Research Institute, Manchester Metropolitan University, for the supply of magnetron coating technique;

I wish to strongly express my thanks to all present and former colleagues who have helped me with accompany, favor, inspiration, advice, and encouragement, and who shares their knowledge and technical expertise with me so generously. Firstly, I would like to give my thanks to Dr. Zhaohe Gao, who has helped me and inspired me so much into research and also feels like my big brother. He is always there whenever I need his help. Special thanks to Dr. Ying Chen, who is also my best example. I learned so much from him about how to deal with study, work and life with patience, passion and rigorous attitude.

I am grateful to have so many friends who care about me, and I would like to say my thanks to them in person. Very special thanks to my parents Mr. Ying Yu and Ms. Xiaoyang Li for their never-ending love, patience and understanding during a difficult period of our lives; At this moment, I am very delighted and grateful to read through my thesis, because it is full of my great memories.

Introduction

The world's energy structure was changed since the first civilian nuclear power station began operation in the U.S. on December 2nd, 1957 [1]. Great effort was given to improving the fuel cladding resistance to beyond-design-basis accidents (BDBAs) after the Three Mile Island accident happened on March 28th, 1979 [2], [3]. On March 11th 2011, nuclear facilities in Fukushima experienced seismic damage and flooding which surpassed what was expected by the BDBA design requirements [4]. Concerns regarding the irreversible impact on public safety and health caused by the nuclear tragedy have propelled demand for the enhancement of BDBA standards and raised the concept of accident tolerant fuel (ATF) [5].

Although the commercial Zr-based alloys have attained optimised properties and widely used for nuclear power plants [6], it still faces critical limitations. Rapid oxidation and hydrogen generation occur when the Zr claddings react with high-temperature steam once loss-of-coolant accident (LOCA) occurs. A very large explosion may follow due to the exposure of hydrogen in the air under abnormal high temperature [7], [8]. Due to the aforementioned intrinsic properties of the Zr alloy, it is not possible to prevent the Zr claddings from experiencing continuous oxidation during accelerated corrosion and hydrogen generation under LOCA conditions by confined modification of the alloying elements and fabrication process [1].

Since significant efforts endeavoured to improve the microstructure and properties of zirconium alloys for decades but could not satisfy accident tolerant requirements, the new design must be considered for the next generation of fuel claddings, ATF claddings. To protect radioactive fuels from emission to avoid severe accidents, there are three potential approaches to designing a brand new innovative ATF cladding, such as commercial Zr claddings with a protective coating, superior steels, and ceramic claddings [6], [9], [10]. However, considering the existing light water reactor (LWR) system, the revolutionary replacement of traditional Zr-claddings is too difficult and time-consuming. Applying coatings to the outer surface of Zr-claddings to prevent rapid

corrosion under LOCA conditions is expected to be the most efficient and commercially viable way to enhance the cladding's current performance [11]. Serval coating systems, such as SiC composite, FeCrAl ternary alloy, and nitride ceramic coatings have been studied under high-temperature steam conditions. However, no coating has been proven to have the ability to protect Zr claddings under LOCA conditions up to now [12]–[14]. Further study on the degradation mechanisms of the protective coatings for Zr-alloy cladding should be carried out.

Since the 1970s, nitride ceramic coatings have been used for corrosion protection for tools when exposed to high temperature and coolant [15]. However, there is no specific information on what would happen to nitride ceramic coatings if they are exposed in an LWR at 360°C under 19.7MPa. The latest research about nitride coatings on the surface of zirconium claddings mainly focused on the steam resistance under abnormal LOCA condition. Therefore, it is of vital importance that nitride ceramic coatings can withstand variances in working conditions and remain protected against steam.

Aim & Objectives

This thesis mainly focused on the study of high-temperature steam and pressurised water corrosion behaviours of ZrN and $TiSi_xN$/Ti coatings. To understand the corrosion mechanism of coating system on Zr claddings in PWR, the thesis was organised to briefly provide an overview of the state knowhow according to PWR and conventional zirconium claddings, including corrosion mechanisms under typical LWR working environment and potential threats under LOCA scenario. Then, we mainly focused on the pros and cons of recently studied accident tolerant fuel (ATF) cladding and protective coating materials. The following two sections concentrated on experimental details and results presentation, including high-temperature steam corrosion and pressurised water corrosion of ZrN and $TiSi_xN$/Ti coatings, including characterisation of the reaction by-products and microstructure. For the results part, the corrosion

behaviour of the selected coatings presented in detail under both pressurised water and high-temperature steam.

This project aimed to evaluate the corrosion resistance of protective coatings for enhanced accident tolerance propose. Coating materials could endure steam tolerance for a considerably longer core safety margin when a loss-of-coolant accident happens and maintain oxidation resistance under normal PWR working condition. To attain proper properties for PWR operation, we mainly focused on the following objectives:

1. Modification of magnetron sputtering parameters to deposit well-bonded ZrN and TiN coatings on Si-wafer, $TiSi_{0.08}N$, $TiSi_{0.13}N$ and $TiSi_{0.19}N$ coatings on Zy-4 substrate.
2. Study the steam resistance of the coatings under simulated LOCA conditions by high-temperature steam test
3. Study the corrosion resistance of coatings under simulated PWR working condition by autoclave test
4. Understand the protection mechanism and corrosion mechanism of nitride coatings under supersaturated water condition and high-temperature steam

This thesis gives a comprehensive results of potential ATF coatings (nitride ceramic) system under both high-temperature steam and pressurised water conditions which simulated the LOCA condition and normal working conditions. It fills up the incomplete study of ATF materials which mainly focus on high-temperature corrosion.

1. Background and literature review

1.1. Overview of nuclear energy

Nuclear energy is defined as the heat or electricity generated through any exothermal nuclear processes [16]. Nuclear reactors can be categorized as nuclear fission and nuclear fusion reactor based on either split of a target nucleus particle or collision of two or more particles. Since 1971, majority of the commercial power reactors are based on nuclear fission with thermal reactor attributed to the abundant uranium and enrichment methods which reduces the fuel cost. The radioactive fission products are protected and encapsulated by four physical barriers, the fuel matrix, the fuel cladding, the boundary of the coolant system and the containment system [6]. In the aspect of coolant, nuclear reactors can be identified as various types of reactors, as listed in Table 1-1 [17]. Apart from the numbers shown below, there are over 50 nuclear reactors under construction all over the world at present [18]. Considering over half of the nuclear reactors are PWRs, development of the next generation ATF claddings is a worth taking an effort in design and evaluate any potential materials under PWR working environment.

Table 1-1 Number of operational reactors by 31, DEC 2016

Reactor type		Number
PWR	Pressurised Light-Water-Moderated and Cooled Reactor	289
PHWR	Pressurised Heavy-Water-Moderated and Cooled Reactor	49
BWR	Boiling Light-Water-Cooled and Moderated Reactor	78
GCR	Gas-Cooled, Graphite-Moderated Reactor	14
LWGR	Light-Water-Cooled, Graphite-Moderated Reactor	15
FBR	Fast Breeder Reactor	3
Total		448

1.2. Overview of Zirconium fuel claddings

1.2.1. Requirements and developments of fuel cladding materials

Pressurised water reactors (PWRs) uses light water as coolant and moderator, as well as reflector materials. Typical service environment parameters of PWRs list in Table

1-2. The fuel cladding system pf PWRs consists of the uranium dioxide fuel pellets and zirconium alloy cladding tubes (UO_2-Zircaloy).

Table 1-2 Typical service conditions for zirconium cladding rods in PWRs [19], [20].

	Unit	BWR	PWR
Discharge burnup	MWd/kgU	55	60
Exposure time	days	1800	1500
Fast neutron fluence	cm^{-2} , E>1 MeV	1E22	1E22
System pressure	bar	70	158
Cladding hoop stress	N/mm2	-60	-100
Cladding temperature	°C	280-320	290-400
Coolant chemistry	O2 ppb	300	<1
	H2 ppm	0.003	3
	B ppm	-	0-1500wt
	Li ppm	-	0.7-2.2wt

As safety has always been the topmost issue of the nuclear power plants operation, the power plants are designed to bear with the beyond-design-basis accident (BDBA) and reactivity-initiated accident (RIA). The purposes of fuel claddings are to provide mechanical support to fuel pellets in order to avoid fission products from leaking during service time and accident scenario. The tubes also transfer heat generated by fission reaction from inside to the outside coolant. Figure 1-1 depicts a schematic example of the typical PWR fuel claddings, where the fuel cladding rods are bundled together with the top and bottom nozzle, spacing grid and guide thimble tubes forming the nuclear fuel assembly [21]. A standard cladding rod is approximately ~570μm in thickness, 3.7~4.5m in length and 9.5mm in diameter, as shown in Figure 1-2 [21]–[23].

Considering the functions and critical structure of fuel claddings, the requirements for cladding materials are: (i) low thermal neutron absorption cross-section, (ii) superior thermal conductivity, (iii) sufficient mechanical properties (strength and ductility), and (vi) excellent corrosion resistance, under service temperature and potential accident conditions. The compelling low thermal neutron cross-section and dimensional stability under intensive radiation fluxes allow its application for the fuel claddings in the nuclear power generation industry. The superior thermal conductivity of zirconium ensures heat transfer through the cladding shell without creating significant temperature difference at inner and outer surface of the claddings. It could avoid the stress arisen and crack

generation in the fuel claddings during operation [24]. Zirconium alloys, such as M5 and ZIRLO, are extensively applied for the fuel cladding tubes due to its excellent intrinsic properties listed above under harsh environment. Further efforts have devoted to enhancing mechanical and corrosion properties. [6]

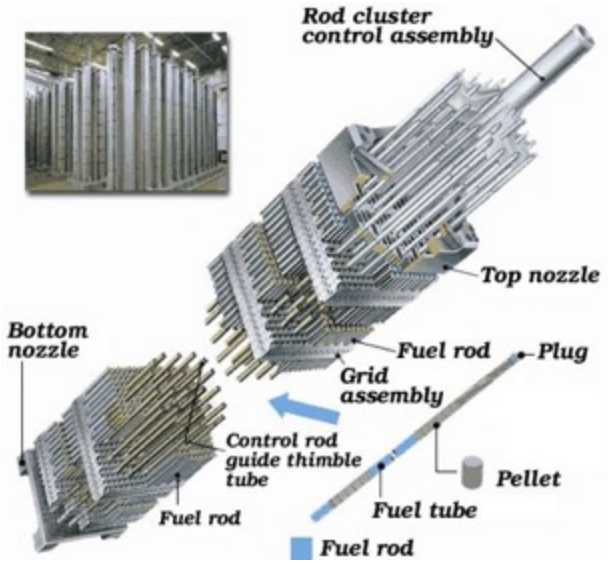

Figure 1-1 The nuclear fuel assembly of a typical pressurised water reactor (PWR).

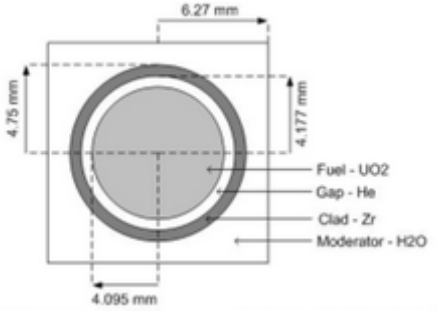

Figure 1-2 The schematic of the cross-section of the Zircaloy cladding tub.

1.2.2. Development of zirconium claddings

Since the first application of unalloyed zirconium in the STR Mark 1 land-based prototype reactor over 60 years ago, the impetus for the modification in zirconium alloy is to enhance the corrosion resistance under irradiation environment and higher fuel duty to achieve higher efficiency. A series of commercially used zirconium alloys lists in Table 1-3. Zircaloy-2 mostly uses for BWR. Zircaloy-4 uses for PWRs with close composition compared with Zircaloy-2. While, ZIRLO and M5 with a longer residence time in plants have applied into higher burnup and higher fuel duty PWRs, where the corrosion resistance of Zr-4 is marginal.

Take the existing zirconium alloys into consideration; two alloy systems have been established, including a Zr-Sn-based system which stands for Zircaloy family and Zr-Nb-based system. Zircaloy with tin as the major alloying element was first introduced to

nuclear reactors in the U.S due to its superior geometry stability under irradiation attack and enhanced tensile strength [28], [29]. By adding niobium, more advanced zirconium alloys with enhanced corrosion resistance have been developed, such as ZIRLO and M5 [30]. Also, by adding limited iron, chromium and nickel, the corrosion resistance in lithium hydroxide solutions can be optimised. Compare ZIRLO and Zircaloy, without Ni, similar oxidation rate but lower hydrogen pickup could obtain to benefit to PWRs. The advantages of ZIRLO are established as less than 40% the corrosion rate, 50% the irradiation growth rate, 80% the creep rate and equivalent hydrogen pickup fraction as Zr-4 [28], [31]. M5 alloys show a significant improvement in 5 times corrosion resistance and much ten times lower hydrogen pickup compared with Zircaloy-4 and stability under higher burnups [30], [32], [33].

Table 1-3 Chemical composition rage of Zirconium alloys [24]–[27]

Elements	Sn	Fe	Cr	Ni	O	Nb	Zr	Application
Zircaloy-1	2.50	-	-	-	-	-		--
Zircaloy-2	1.50	0.12	0.10	0.05	-	-		BWR
Zircaloy-4	1.20-1.70	0.18-0.24	0.07-0.13	≤0.07	-	-		PWR
ZIRLO	1.0	0.10	-	-	-	1.0	Bal.	PWR
Optimized ZIRLO	0.67	0.1	-	-	-	1.0		
M5	-	0.05	0.015	-	0.14	0.80-1.20		PWR

The enhanced corrosion resistance of Zr-Nb series alloy is the result of restrained phase change during corrosion under high temperature (LOCA conditions). The reason for restrained phase change is the stress induced by second-phase precipitates(SPPs) formation resulted from limited niobium solubility within zirconium lattice [34]. However, tin dissolves entirely within zirconium in Zircaloy, which could not provide resistance to the phase change and eventually lead to accelerated corrosion [35]. The fabrication process, including utilised β-treatment, rolling, intermediate annealing, and final annealing, is devoted to controlling the size of SPPs. ZIRLO is in fully recrystallised condition with second phase precipitation such as body centred cubic niobium-rich phase, so-called β-niobium, and hexagonal phase (Zr-Nb-Fe) [29]. M5 is a ternary Zr-

Nb-O alloy with nominally 1% Nb and controlled limitation of Fe and S [30]. The microstructure of the M5 alloy is fully recrystallized with fine grains (3-5 μm in diameters) and uniformly distributed SPPs. The SPPs are mostly Nb-rich β-phase particles with 50nm in diameters and a few larger intermetallic particles $Zr(Nb, Fe, Cr)_2$ with hexagonal crystalline structure [32], [36].

1.2.3. Problems with Zirconium cladding

Table 1-4 List of issues exist in Zr-claddings under designed normal and accident conditions[37], [38]

Performance Conditions		Problems
Normal condition	**Coolant corrosion**	✓ No problem (Oxide thickness less than 100nm)
	Creep	✓ No problem (Hoop strain less than 1%)
	Irradiation growth	✓ No problem (shoulder gap closure)
	Wear resistance	✓ No problem (wear-loss less than 10% in thickness)
	Pellet-Cladding mechanical interaction (PCMI/PCI)	• PCMI failure due to hydrides (hydrogen embrittlement and hydride reorientation)
Design-basis accident (DBA)	**Loss-of-coolant accident (LOCA)**	• Rapid oxidation and H_2 generation • Steam generation • Blooming and burst due to inner cladding stress (fission gas) • Design limitation (max peak temperature 1204°C, max oxide thickness 17%)
	Reactivity-initiated accident (RIA)	• PCMI failure due to hydrides
Beyond design-basis accident (BDBA)		• Severe oxidation and hydrogen generation • Melting

The failure of cladding rods is defined as the loss of hermeticity. In general, the degradation processes which may challenge the integrity of the cladding tube includes overheating, mechanical (grid-to-rod) fretting and fracturing, dimensional change (rod bowing or irradiation growth), fuel rod internal burnable poison gas pressure, crud-induced localized corrosion, waterside corrosion, and hydriding. Table 1-4 summarises the potential failure and degradation issues, considering the performances of zirconium

claddings during operation and accident situations [37], [38]. However, corrosion and oxidation have been the most considerate issues for the research of zirconium claddings. This chapter will discuss the problems with zirconium claddings pertaining to corrosion during regular operation and LOCA.

Intrinsically, the pervasive degradation mechanism of zirconium claddings is microstructure transformation caused by corrosion and oxidation, which leads to oxide formation and hydrogen embrittlement. What's more, the oxide layer formation would significantly impair the ductility of zirconium claddings, which can cause fragmentation during the reflooding phase after LOCA. Thus, it is worth perceiving the fundamental oxidation mechanism of the Zr claddings to establish the design criteria for ATF materials.

1.2.3.1. Corrosion mechanism under PWR

Under the PWR working environment, the Zr claddings are favourable for the waterside corrosion accompanied by hydrogen pickup. The corrosion reaction of Zr in water shows in Equation 1-1. The driving force for the zirconium corrosion is the high Gibbs energy of the ZrO_2 formation reaction, around 965kJ/mole at 360°C [39].

$$\boldsymbol{Zr + 2H_2O \rightarrow ZrO_2 + 2H_2} \qquad \text{Equation 1-1}$$

The corrosion process displays in Figure 1-3. As a result of the zirconium oxidation thermodynamics and the explosive condition, electrochemical potential establishes at the oxide layer interfaces with coolant and metal Zr. It drives the transportation of oxidising mobile species, such as oxygen anions, oxygen vacancies, electrons and hydrogen cations O^{2-}, $V_{\ddot{O}}$, e^- and H^+ within the oxide layer indicated by the thick arrows. Reactions ❶ to ❺ happen in series, while the reaction rate depends on the diffusion of oxidising species [40].

First, oxygen anions are dissociated from water molecules and absorbed at the oxygen vacancy sites onto the oxide surface, marked as ❶ and❷. As a result of the defect density gradient from the oxide-Zr interface into oxide layer and the electrochemical

potential through the oxide layer, the oxygen atoms transport through the bulk of oxide or along the oxide grain boundaries via solid-state diffusion[39], [41], [42], marked as green and blue thick arrows. Once the oxygen anion arrives at the oxide/metal interface, it reacts with Zr-cations and forms new oxides, marked as ❹. Accompanied by oxide formation, electrons are released (reaction ❸) and transport through the oxide layer (thick purple arrow) by a hopping mechanism. Then these elections react with the hydrogen cations formed by water dissociation (reaction ❺) to reduce the electric charge difference. Due to the solubility of hydrogen in the coolant and bulk materials, the sites of cathodic reaction could be at the surface of oxide/coolant, within the growing oxide layer or at the oxide/metal interface[43]. However, instead of combining with electrons, some hydrogen cations dissolve into the oxide layer and transport through the oxide layer to the substrate metal(thick orange arrow), which defined as hydrogen pickup[27].

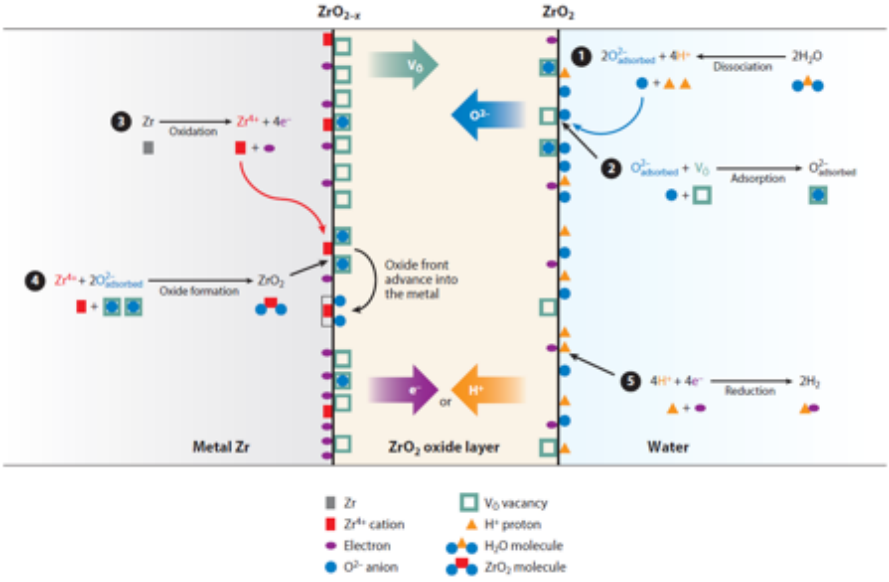

Figure 1-3 Schematic shows the corrosion mechanism in the water-Zr alloy system

The corrosion kinetics of zirconium alloys in an aqueous environment usually indicates an approximate parabolic oxidation rate during the initial pre-transition stage, shown in Figure 1-4. The pre-transition corrosion rate in a given situation shows good reproducibility within the series of zirconium alloys, which follows an empirical law, as

$$w = At^n \qquad \text{Equation 1-2}$$

where w represents the weight gain, t is the exposure time, and A and n are constants which are determined by the nature of the alloy. Normally, in the aspect of zirconium, n is less than 0.5 and the oxidation curves manifest sub-parabolic relations. The value of n for different zirconium alloy can be measured at the very first stage of corrosion by fitting the weight gain data as a function of exposure time to the empirical power law [30]. When the corrosion rate follows a parabolic law, zirconium is usually in the protective corrosion stage where the corrosion rate of Zr-alloy reduces as the thickness/weight of the oxide layer increases.

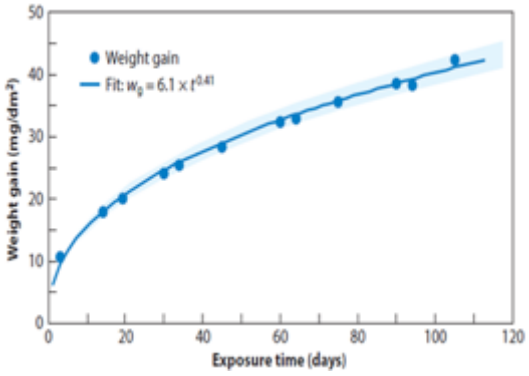

Figure 1-4 Measured corrosion rate fitted with power-law of the pre-transition stage of the ZIRLO sheet alloy

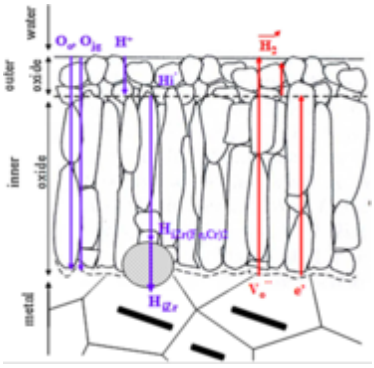

Figure 1-5 Oxide growth structure schematic of Zy-4 alloy after PWR simulation [44]

The initially formed oxide layer at the surface of zirconium alloy exhibits a small, equiaxed grain structure with 30-40nm in diameter. The oxide grains randomly orient and crystalline as a mix of tetragonal and monoclinic ZrO_2 phase. [44] As the oxidation continues, oxide grains with columnar structure begin to grow between the equiaxed grains and metal in a preferred orientation attributed to the texture of the substrate in order to minimise the stress inducement. The columnar grains grow to an approximate length of 200nm and then start to re-nucleate in order to keep an anisotropic direction. At the same time, pores start to form as equiaxed cavities and then grow in the form of small tubs at the columnar oxide grain boundaries [34], [45]. Figure 1-5 shows the schematic of the initially formed oxide structure of Zy alloy in a water environment. The control factor of zirconium alloy initial stage oxidation is generally considered as the diffusion of charged mobile species under a concentration gradient, such as oxygen vacancies and electrons, within the formed oxide layer.

With the increasing service time, the stress accumulation finally exceeds the strain tolerance of the oxide layer. Then, lateral cracks start to form and connect with tubular pores, which may cause loss of protection due to the linkage between the waterside and metal/oxide interface. The corrosion of Zr follows with an oxide transition associated with a dramatic change in corrosion rate, as shown in Figure 1-6[46]. The oxide transition point is defined as critical oxide thickness, usually around 2-3μm, where the corrosion kinetics changes. The following up growth of oxide layer repeats the initial stage, shown in Figure 1-7, and remains protective, which displays with the red curve in Figure 1-5. This protective oxidation behaviour normally happens in Zircaloy-4 and ZIRLO.

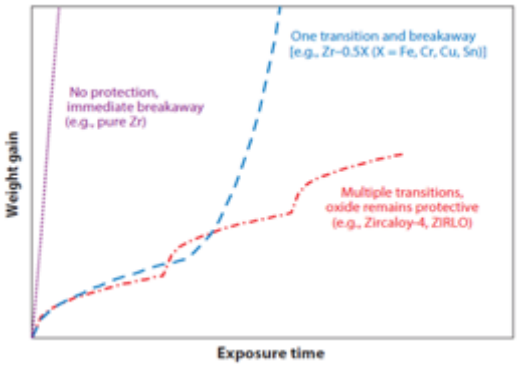

Figure 1-6 Schematics of typical corrosion transition processes of zirconium alloys

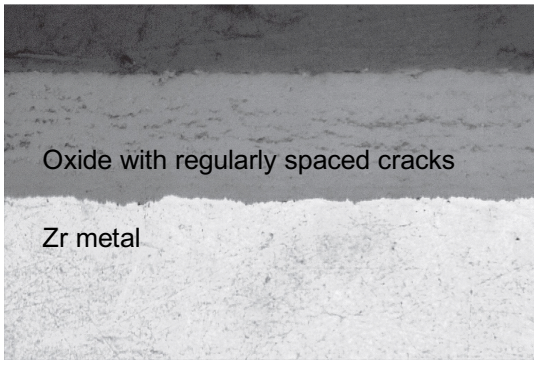

Figure 1-7 Periodic oxide layers in AXIOM X1 at 70GWD/MTU [27].

However, some other alloys present rapid corrosion after the oxide transition at the end of the initial parabolic corrosion stage. This phenomenon is defined as corrosion breakaway, it can happen immediately once corrosion occurs or after the first stage of oxidation, shown as the purple and blue dashed curves in Figure 1-5. The transition from parabolic power law to a nearly linear rate at high temperature could result from the phase transformation from tetragonal to monoclinic zirconia in Zy-4 [47], [48]. Due to the lattice expansion during tetragonal to monoclinic ZrO_2 transformation, cracks are induced to the oxide scale, which leads to the accelerated oxidation by free path for oxygen penetration [49], [50]. Once the operating temperature exceeds 1000°C, oxygen atoms cannot reach the formation of non-stoichiometric zirconia, in this circumstance, porous, non-productive, stoichiometric ZrO_2 forms which may lead to high rate corrosion

and finally cause the oxide spallation [51]. Several investigations have suggested that the transition from non-stoichiometric oxide to stoichiometric oxide decreases the plasticity of the oxide layer, which may lead to crack formation [47]. Breakaway oxidation is widely reported to occur much earlier when the atmosphere contains impurities, such as water vapour or nitrogen, or any interstitial impurities present in the metal and alloys, such as oxygen, carbon, and nitrogen [47].

1.2.3.2. Hydrogen embrittlement

Hydrogen has been considered as an important factor in the corrosion performance of fuel cladding [30], [34] [50], [51]. Hydrogen diffusion into the cladding matrix and formation of brittle phase could cause the degradation of its thermal[44], [52] and mechanical properties[42], [53]. These degradations include: (1) accelerated stress corrosion cracking (SCC)[54], [55]; (2) delayed hydride cracking (DHC); (3) brittle hydride rim formation underneath the oxide scale; and (4) localised hydrogen plasticity and brittle hydrides induced loss of fracture toughness. The source of hydrogen could be the following[24], [56]:

1) Produced by the aqueous corrosion of zirconium fuel cladding at the interface of coolant and cladding

$$\boldsymbol{Zr + 2H_2O \rightarrow ZrO_2 + 4H} \qquad \text{Equation 1-3}$$

2) Decomposed from coolant due to radiation

$$\boldsymbol{H_2O \rightarrow H + OH} \qquad \text{Equation 1-4}$$

3) Moisture presented in the fuel pellets within the claddings
4) Infused hydrogen into the coolant to consume the nascent oxygen produced by radiolytic decomposition

The hydriding mechanism at the initial stage is discussed below. It is unavoidable to neglect the thin oxide layer formed due to large zirconium affinity for oxygen in both oxygen atmosphere and water vapour, even at ambient temperature. The initially formed thin oxide layer is in the form of oxygen solid solution (Zr_2O, ZrO and Zr_2O_3) accompanied by ZrO_2[57]. Normally, the oxide layer will act as a protective barrier to

hydrogen if it is continuous. Which means, hydrogen is not able to penetrate this layer and absorb into Zr lattice. It is because of the formation of O-H bonds which trapped H and prevent H diffusion at room temperature[58], [59]. So, the most accepted mechanism of hydrogen diffusion at ambient temperature is established on the base of microstructure and atomic-scale defect structure within the oxidant layer, such as grain boundaries and dislocation lines [52]. However, at a higher temperature around 300°C, which is the normal reactor operation temperature, this thin oxide layer starts to dissolute gently while hydrogen is parting of from O-H bonds. When the temperature increased over 500°C, aggressive breakage of O-H bonds starts to form H_2O and ZrO_2[60]. Due to the dissolution of the oxide layer, micro-cracks formed within the oxide layer create a shortcut for oxygen and hydrogen diffusion, especially at the grain boundaries of zirconium[29], [61]. This results in rapid weight gain and hydrogen uptake of zirconium claddings. To sum, the initial stage of hydriding is due to the breakaway of the initial oxide layer at a high-temperature water environment.

The hydrogen pickup fraction is defined as the ratio of the hydrogen absorbed by the metal matrix over the total amount generated during the corrosion reaction.

$$f_H = \frac{H_{absorbed}}{H_{generated}} \qquad \text{Equation 1-5}$$

The kinetics of hydrogen pickup is also very difficult to identify, but it functionally depends on oxide thickness and is non-monotonic due to transitional oxidation. That is to say, the fraction of hydrogen pickup also closely depends on the alloying elements, microstructure, corrosive chemistry environments and corrosion time[24], [27], [42], [62]. [63]. At PWR operating temperature, the hydrogen pickup fraction of Zy-4 is around 25%, theoretically, and which is less than a half of that for Zy-2. However, M5 has demonstrated dramatically good hydrogen resistance compared to Zy-4, shown in Figure 1-8.

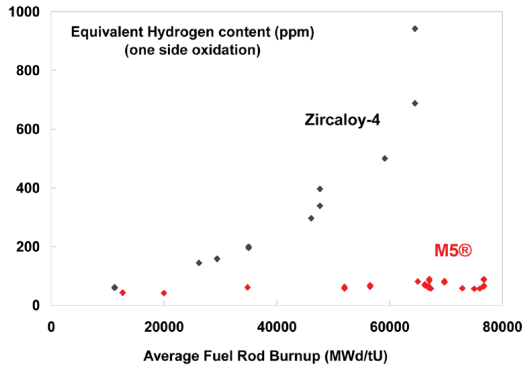

Figure 1-8 Hydrogen pickup of Zy-4 and M5[64]

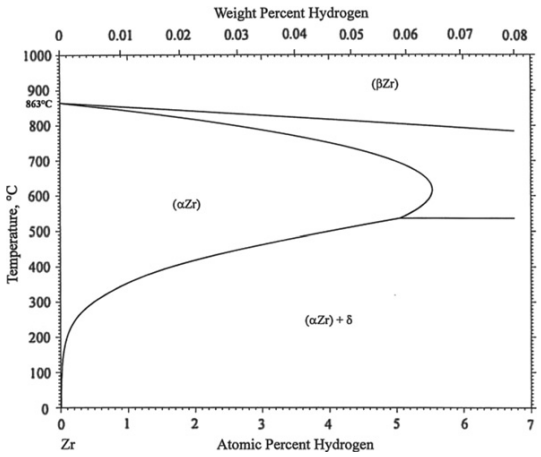

Figure 1-9 Phase diagram of Zr-H system at low hydrogen concentration[65]

Solid evidence manifested that the fraction of hydrogen pickup varies during the oxidation process due to the oxide morphology[66]. And it indicated that the pre-transition oxide with a double sub-layered structure showed a remarkable difference of hydrogen diffusion coefficients[20]. The external oxide layer was extremely hydrogen transparent even at low temperature (<300°C), whereas the inner part of the pre-transition oxide layer acted hydrogen barrier, so does the post-transition oxide. Due to the kinetic transition, microstructure degradation occurs, porous and cracks formed within the scale of the initially formed oxide. Therefore, the overall hydrogen absorbed in the post-transition oxide layer is ten times over pre-transition oxide. However, the inner layer is a protective layer, which is the same as the pre-transition regime, theoretically. Therefore, hydrogen diffusion within the inner oxide layer was considered as the limiting step of hydriding.[20]

Once the solubility of hydrogen in the metal matrix exceed its limitation, zirconium hydrides start to precipitate mostly sited under the metal/oxide interface as a result of the thermal gradient across the cladding during operation under irradiated temperature[20], [52], [67]. For pure Zr, the solubility of hydrogen is about 170ppm at 400°C, and once the concentration of hydrogen exceeds the limitation, zirconium hydrides (δ) start to form, which is shown in Figure 1-9. Many studies on the effect of hydrogen precipitates on the oxidation behaviours of Zr-4 have proved that a higher oxidation rate of the hydride phase compared with the α-Zr matrix accompanied a distinguished oxide microstructure. While Nb causes a reduction effect on the hydrogen

pickup fraction due to the donor effect in the alloy while Cu increases it. Also, as the size of second-phase precipitates $Zr(Fe,Cr)_2$ increases, the hydrogen pickup fraction decreases.

The formation of massive precipitation of hydride in the metallic part near the metal/oxide interface at high burnup is generally agreed as the causes of the accelerated corrosion of Zy-4[30], [34], [44], [68], [69]. Also, there are some studies indicated a decohesion impact of hydride precipitates within the α-Zr crystalline lattice which may enhance the diffusion of oxidising species through the oxide scale to the metal/oxide interface and therefore cause the accelerated corrosion[44], [52]. Also the hydride precipitation in the metal results in less tolerance of the stress due to the oxide growth and formation of more curved metal/oxide interface associated with more interface area, which may trigger the oxide transition at an earlier stage and the accelerated corrosion after oxide transition[42]. What's more, evidence showed that higher hydrogen concentration could lead to changes in oxide structure from long columnar grain to equiaxed grains.

1.2.3.3. The control factors of corrosion

The cladding corrosion parameters are mainly based on relation between operation time and temperature and related to burnup. However, other factors, for example, coolant flow, coolant chemistry, flux speed, and cladding hydrogen levels can further affect the corrosion sensitivity according to temperature changes.[27] The corrosion failure of Zr-claddings is by far much complex, which is combined with various phenomena rather than singular influence factor.

Accelerated corrosion was observed on Zircaloy-4 at over 30 GWD/MTU burnups [27], [44]. However, no significant evidence of accelerated corrosion on M5 was observed, such as oxide structure changes or any other parameters[30], shown in Figure 1-10. Based on the microstructure evolution, the dissolution of second-phase precipitates $Zr(Fe,Cr)_2$ due to the impact of radiation were a prefered hypothesis for the accelerated corrosion kinetics[30] [70] [71].

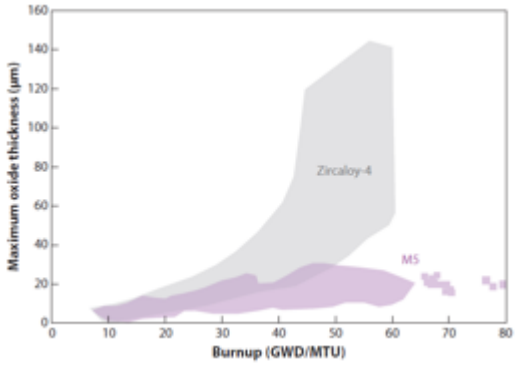

Figure 1-10 Burnup dependence of oxide thickness for Zircaloy-4 and M5. [27]

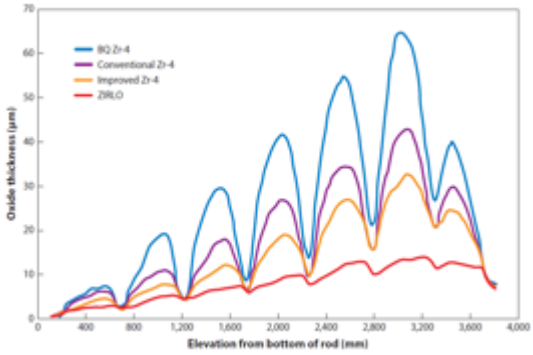

Figure 1-11 Oxide thickness along the axial direction of zirconium alloy fuel rods[27], [72].

Considering the corrosive service environment, hydrogen, iodine and lithium are susceptive for the corrosion of zirconium claddings [53]. Iodine is generated due to fuel fission reaction and represented to be the most toxic corrosive medium which is highly responsible for the stress corrosion cracking (SCC) accompanied with the stress induced by the radiation-growth of zirconium cladding[55], [73]. Autoclave tests revealed the sensitivity of oxidation kinetics of Zr-Nb-based alloy in lithium hydroxide water, and more porous oxide structure was found grown on the Zy-4 cladding surface [31].

The thickness of oxide layer along the axial direction increases from bottom to the top of the cladding rods with eddy current traces, shown in Figure 1-11. The particular eddy current shape of oxide thickness is as a result of the enhanced heat transfer from light water coolant and flux suppression at the grid locations. The figure suggests that Zy-4 alloys are strong flux dependent for the oxide formation. Also, the critical lifespan of the fuel assembly depends on the limiting thickness of oxide layer on the upper spans of fuel claddings due to the highest coolant temperature at the upper spans of the fuel assembly[72].

1.2.3.4. High-temperature corrosion by steam

High-temperature corrosion indicates material degradation under off-normal high temperature and harsh environments, such as steam, radiation and corrosive gas. Under accident conditions, the heat generated by the fission reaction leads to rapid temperature rise and steam generation, which may cause the rapid oxidation of

zirconium. Also if the fracture of PWR occurs associated with the failure of ECCS, steam will be generated due to severe coolant loss and fuel cores will be heated up, resulting in further damage to fuel claddings, which so-called LOCA.

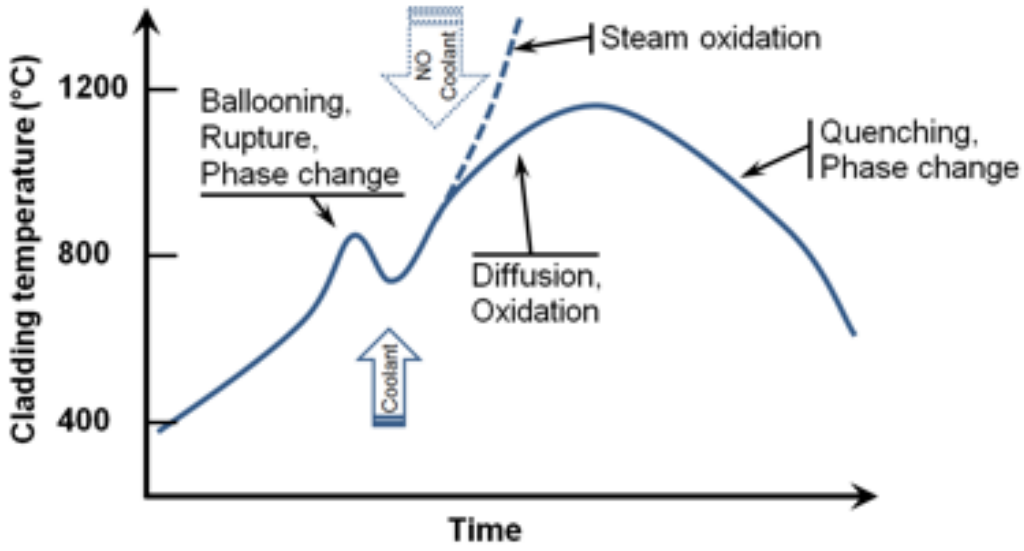

Figure 1-12 Schematic of zirconium cladding temperature during LOCA

The above schematic shows the corrosion behaviour of fuel claddings under steam attack versus time and temperature (Figure 1-12). Once the temperature rises to 700-900°C, the zirconium cladding would exceed its ultimate tensile strength due to the rod internal pressure. Any localised instability would cause severe ballooning strain and rupture would occur if it reach sufficient pressure and temperature [74]. A modest drop of temperature would happen due to the injection of enhanced coolant but continues with temperature rise. At the current pressure and temperature, the contact environment of zirconium claddings is the high-temperature steam. Eventually, when the sufficient coolant system starts to function, the temperature begins to decrease, and rapid cooling or quenching occurs if the temperature drops to 400-800°C. Furthermore, if the emergency cooling system is not responding, when the temperature rises above 1200°C, corrosion of Zr becomes self-catalytic and exothermic due to the Zr alloy reaction with steam. The heat released significantly accelerates temperature rise, which

quickly outperforms than the heat generated by fuel fission and results in massive production of hydrogen as the by-product.

Based on the widely accepted reaction between Zr and water vapour, massive flammable H_2 generated and the chemical heat generated by this reaction (Equation 1-6) ($\Delta H = -586 kJ/mole$)[75], [76] would give rise to pressure and temperature surge.

$$\boldsymbol{Zr + H_2O_{steam} \xrightarrow{HT} ZrO_2 + 2H_2}$$ Equation 1-6

At the temperature range from ambient to 650-800°C, zirconium cladding consists of a hexagonal crystal structure, namely alpha phase (α). As the temperature continues to increase, the α phase begins to enter a mixed-phase regime, part of which transforms to a face-centred cubic geometry or beta phase (β). The phase transformation temperature point varies due to the element concentration. For Zy-4 with an initial O concentration at 0.11w.t.%, the α phase to the mixed phase (α & β) change at the temperature around 810°C, and the complete transition to β phase is at about 980°C. Oxygen has been confirmed to act as an α -stabilizer, once the content of oxygen increase and the phase transformation temperature will rise. On the contrast, the existence of hydrogen and the substitution of Nb for Sn will decrease the value, due to their stabilised effect on β phase.[35]

Corrosion behaviour is controlled by the diffusivity of oxygen within different phases and microstructure. It is associated with alloy-component-induced or oxygen-induced phase transformation. Higher Nb and lower Sn could lead to forming a thinner oxygen-stabilised α-Zr layer, and α-Zr contained prior β-Zr layer[77]. The diffusivity of oxygen in both Zr claddings and outer grown ZrO_2 increases rapidly above 800°C. Therefore, once the temperature over that of α to $\alpha + \beta$ to α phase transformation, it is high enough for oxygen to transport through the oxide layer and diffuse into metal. And it can soon exceed its solubility in the outer layer of the cladding. Instead of forming other precipitations or phase, the outer oxygen-rich layer turns back to α phase, so-called oxygen stabilized alpha phase, $\alpha - Zr(O)$, in which oxygen solubility is higher than in β

phase. Once cooling occurs, the inner β phase also transforms back into α phase, so-called prior-β phase.

Therefore, a remarkable difference of microstructure at room temperature can be distinguished between the inner prior-beta phase and the oxygen stabilised alpha outer layer. The oxide layer surface of steam treated zirconium tubes displays in Figure 1-13. The surface morphology is identified as a mixture of pre-transition oxide (white, flaky, fully converted ZrO_2) and post-transitional oxides (tenacious black)[78]. Figure 1-14 shows an SEM image of the cross-section of the steam treated Zircaloy cladding with a three-layered microstructure. An outer, fully-converted ZrO_2 layer formed at pre-transition associated with various length of axial and transverse cracks due to the tensile stress induced by the volume expansion; a partially converted intermediate zone of oxygen-stabilized $\alpha - Zr(O)$ phase and a minimally oxidized β -Zr phase of the base metal are clearly revealed. Similar oxide morphology has been observed by other studies on the steam oxidation of Zy-2[13], [79] and Zy-4[77], [80], see Figure 1-15. Only the β -Zr phase can maintain the ductility of the zirconium cladding since ZrO_2 and oxygen-stabilized $\alpha - Zr(O)$ phase formed under 1200°C steam attack are brittle phases in the aspect of mechanical properties. Considering the thickness of fuel cladding and harsh working environment, steam corrosion is a key factor which affects the safety and lifetime of the fuel claddings under accident conditions.

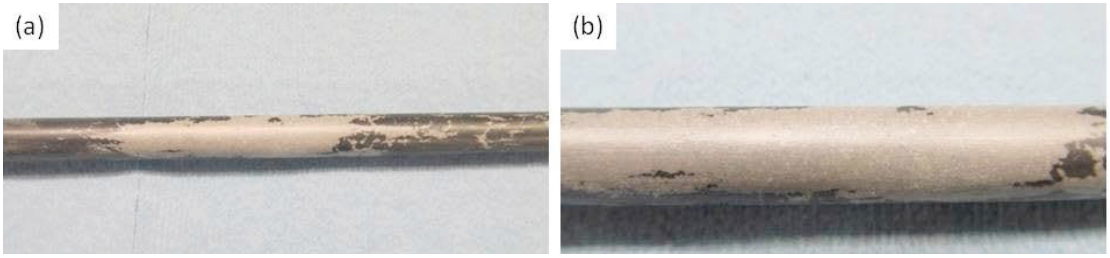

Figure 1-13 Surface condition of Zy-702 tube after 1hour steam oxidation treatment at 1000°C

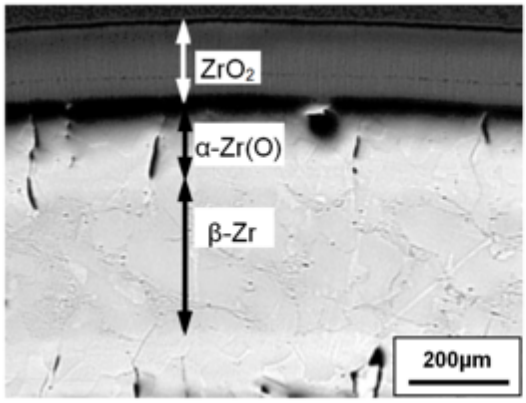

Figure 1-14 Optical micrographs of the cross-section of Zircaloy BWR cladding specimen oxidised at 1200 for 2h in 1MPa steam[13]

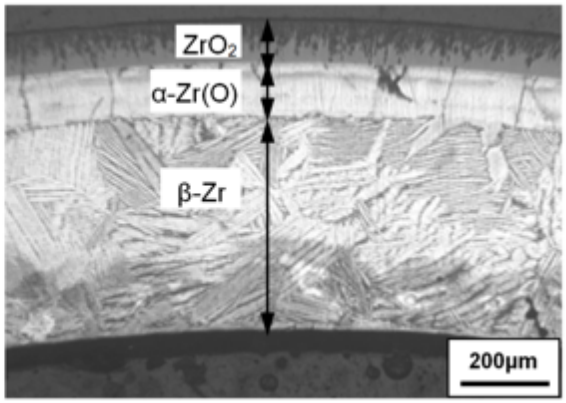

Figure 1-15 Unirradiated Zy-2 after 600 seconds steam oxidation test at 1200°C[35]

1.2.3.5. Steam oxidation mechanism

Based on the new atomic theory of water-vapour oxidation proposed by *Lanli Luo* group, the mechanistic understanding of water vapour corrosion has been distinguished from dry oxidation at the atomic scale[81]. Direct observation of the atomic-scale defect dynamic reaction during the early-stage oxidation at elevated temperature has been demonstrated. Considering the oxidation reaction, oxide develops by a layer-by-layer growth principle via the adatom mechanism which allows diffusion of both metal and oxygen atoms to the oxidation front. However, a significant characteristic of the oxidation in H_2O is different from pure oxygen oxidation behaviour, which involves vacancy cluster formation and migration. The vacancy clusters are incorporated by both metal and oxygen vacancies, which are only in sub-nano scales. Three typical features have been identified for the vacancy clusters dynamic evolution[81], see Figure 1-16:

(1) Migration: the metal and oxygen vacancies diffuse from the m/o interface to o/g interface, at the opposite direction of O atoms.

(2) Condensation: during diffusion, metal and oxygen vacancies gather together and continue diffusion towards the outer surface.

(3) Annihilation: by migrating to the oxide surface, the vacancy cluster forms a pit and subsequently filled up with adatom which results in a new flat oxide surface.

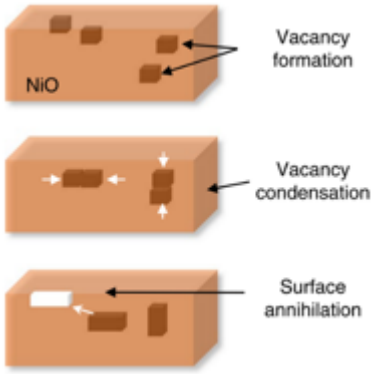

Figure 1-16 Schematics of vacancy cluster dynamics[81]

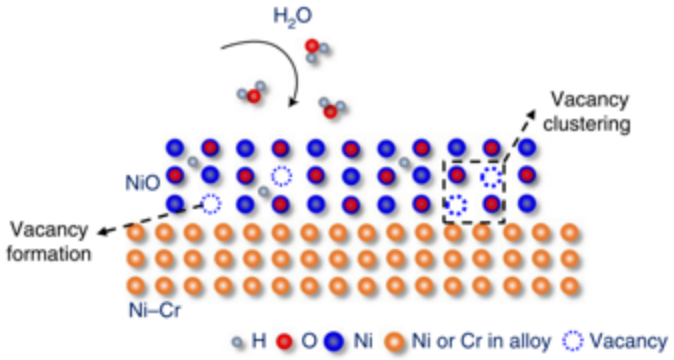

Figure 1-17 Schematic of the atomic processes in the oxidation of NiCr alloy in water vapour, illustrating at the atomic level that water vapour enhances vacancy formation and promotes vacancy clustering. [81]

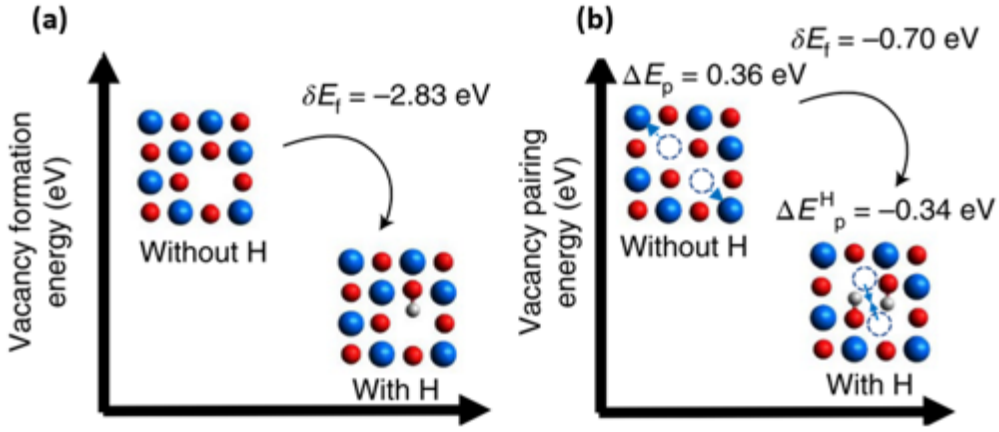

Figure 1-18 DFT calculation results of vacancy formation energy and vacancy pairing energy with and without the presence of $Hi^{\bullet}$. (a) shows that vacancy formation energy decreases by 2.83 eV in the presence of $Hi^{\bullet}$. (b) shows that in NiO two separated Ni vacancies repel each other due to the positive energy of 0.36 eV; while the vacancies merge to form clusters with the presence of $Hi^{\bullet}$ due to the pairing energy decrease to -0.34eV. [81]

When corrosion occurs in a water vapour environment, H_2O molecules can be adsorbed at the oxide surface, then dissociated into OH^- and H^+ and further broken to free oxygen ions and interstitial protons. The interstitial proton $H_i^{\cdot}$defects have been proved to accelerate corrosion by the oxide low diffusion barrier against H^+, which can lead to a decrease in vacancy formation and combination energy, see Figure 1-18. Also, protons can lead to the decrease of a diffusion barrier for both Ni and O within the NiO, thus, facilitate the ion migration.

As the growth of oxide is leading by the through-lattice diffusion of metal ions and O, which is controlled by the diffusion of vacancies. With the presence of $H_i^{\cdot}$, the vacancy

clustering phenomenon cause a highly porous oxide scale at the initial oxidation process, which could affect the continuing formation of the protective oxide layer. Based on their observation, the rate of subsequent oxidation of NiO is much higher in H_2O than in pure O_2. This accelerated water vapour corrosion attributed by vacancy clustering occurred for both Ni-Cr alloy and pure Ni film.

The new atomic steam corrosion mechanism can apply to zirconium under a steam environment at 400-600°C. Several ten percent of hydrogen that migrates into metal is due to recombination and formation of hydrogen ions (protons) by the decomposition of water molecule instead of neutral hydrogen atoms direct dissolved into Zr matrix. The water vapour decomposes, and H^+ generation can be described as the following equations:

$$\boldsymbol{H_2O(g) + V_O^{2+} = 2H^+{}_{ad}(g/ox) + O(ox)} \quad \text{Equation 1-7}$$

$$\boldsymbol{H^+{}_{ad}(g/ox) + e_v^-(ox/g) = H_{ad}(ox)} \quad \text{Equation 1-8}$$

$$\boldsymbol{Zr(m) + 2O(ox) = ZrO_2(ox) + 2V_O^{2+} + 4e_v^-(m/ox)} \quad \text{Equation 1-9}$$

When oxygen atom of the water vapour attaches with oxygen vacancies at the oxide surface, a neutron oxygen atom can be left within the oxide lattice, and the two released protons are adsorbed at the interface of water vapour gas and oxide layer (g/ox) (Equation 1-7). The cathodic reaction by combining with electrons in the oxygen vacancies forms hydrogen atoms within the oxide layer (Equation 1-8). As the anodic reaction at the interface between metal and oxide layer, oxygen vacancies associated with electrons are generated and outward diffusing through the oxide layer (Equation 1-9). What's more, a small amount of the adsorbed H atoms can rather form absorbed hydrogen molecules (Equation 1-10), or release as hydrogen gas form (Equation 1-11).

$$\boldsymbol{H_{ad}(ox) = H_{ab}(ox)} \quad \text{Equation 1-10}$$

$$\boldsymbol{2H_{ad}(ox) = H_2(g)} \quad \text{Equation 1-11}$$

However, some water decomposes as two hydrogen atoms and doubly charged oxygen anion, which dissolve in the oxide layer (Equation 1-12). Then, oxygen anions combine with adsorbed H^+ forming dissolved OH^- within oxides (Equation 1-13).

$$H_2O(g) + V_O^{2+} = 2H_{ad} + O^{2-}{}_{ab} \quad \text{Equation 1-12}$$

$$O^{2-}{}_{ab} + H^{+}{}_{ad} = OH^{-}{}_{ab} \quad \text{Equation 1-13}$$

$$H_2O(g) = H^+ + OH^- \quad \text{Equation 1-14}$$

Also, H_2O can break as a proton and hydroxyl (*Equation* 1-14). Since the diffusivity of OH^- and O^{2-} in the oxide layer is relative high, the majority of H is transferred by the proton which is carried by these negative ions and diffuse together in order to neutralize the oxide layer[24], [82], [83]

To be concluded, some alloys have been proved with accelerated oxidation rate at the initial stage of water oxidation and porous defect structure formation of the continuous oxide. The water-promoted corrosion is initially driven by the interstitial protons, which lowers vacancy formation energy, accelerates vacancy clustering and facilitates metal cation and oxygen anion diffusion, and it results in the formation of the porous structure in the oxide layer.

1.3. Development of ATF

The Fukushima accident has been a strong intention to design the new generation of ATF fuel cladding system to maintain or improve fuel performance during normal operations and operational transients, as well as during design-basis and beyond-design-basis events. The ATF program's mission is to develop a fuel system that improves the safety, competitiveness and economics of the LWR.[34] Generally, the concepts of ATF claddings are to reduce degradation rate and heat generation of traditional Zr claddings corrosion against high-temperature water vapour and to maintain mechanical stability against ballooning and burst of Zr claddings, thereby prolonging safety response time for LOCA.

1.3.1. Requirements for ATF

Considering that the LWR is the most extensively applied worldwide, the design of ATF should mainly focus on the applicability in this particular type of reactor. Truly, current regulations for LWRs are designed in obedience to the safety criteria for accident

situations, even LOCA. LOCA are postulated accidents that caused by the loss of reactor coolant, at a rate beyond the capability of the coolant support system. It would result from the breakage of coolant pressure boundary pipes up to and including a rupture of the equivalent size of the largest pipes in the cooling system.[86] The specified criteria are imposed on the performance of Zircaloy cladding fuel rods. The up-to-date U.S. Nuclear Regulatory Commission (NRC) clarified five calculated requirements for LOCA criteria[86].

(1) Peak cladding temperature shall not exceed 2200°F (1204°C)
(2) Maximum cladding oxidation thickness shall not exceed 17% of the original cladding
(3) Maximum hydrogen generation shall not exceed 0.01 times the hypothetical level generated by the reaction of all metal claddings surrounding the fuel pellets.
(4) Coolable geometry after calculated core geometry changes
(5) Long term cooling shall be maintained after any calculated successful initial operation of the ECCS.

Although the above-listed safety regulations may vary depending on the upgrading of the new fuel materials and reactor operational design, such as high fuel burnup and longer fuel cycle. The fundamental principles of LWR design regarding LOCA situations based upon the current criteria are still imperative to the ATF material design.

It is worth understanding the purpose of the design criteria to find out the limitations that need to breakthrough for the even harsher environment with enhanced accident tolerance. The current sustainable peak temperature (2200°F, 1204°C) and the maximum equivalent cladding oxidation thickness (17%) were selected to attain adequate protection of the cladding against the thermal shock during reflooding after LOCA[35]. The maximum limit of hydrogen generation can also affect the ductility of corroded Zr claddings. The predominant failure mechanism of cladding is because of the degraded ductility caused by oxidation and hydrogen embrittlement.[87], [88] The coolable geometry and long term cooling criteria are also influenced by the cladding

oxidation, since the possible change in coolant channel structure as a result of the potential blockage due to brittle cladding fracture and the degradation in thermal conductivity due to oxide layer formation. To sum up, oxide layer formation and hydrogen generation induced ductility loss are the predominant focus for the regulation design of the next generation ATF claddings.

From the preceding paragraph, the important attributes of enhanced accident tolerance can be identified and defined as 5 categories: reduced hydrogen generation (resulting from cladding oxidation), reduced cladding reaction with high temperature steam, enhanced fuel properties and fission product retention under severe accident conditions, and improved fuel-cladding thermos-mechanical interaction for enhanced performance under extreme conditions, shown in Figure 1-19[34], [35][75].

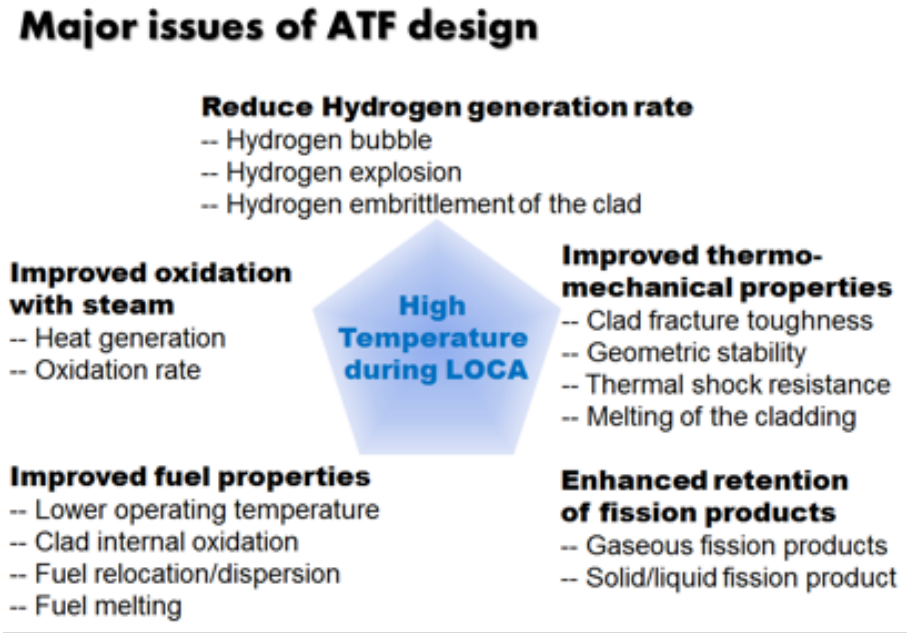

Figure 1-19 Identification of the important attributes of the ATF system design.

The design criteria for the ATF is to maintain its structural integrity under normal working conditions and accidental situations, such as loss-of-coolant accident (LOCA) and reactivity-initiated accident (RIA) to avoid the failure of fuel cladding, the releasement of fission product and further damages. To be more precise, it requires the ATF materials with sufficient mechanical properties and superior chemical stability to serve in the pressured coolant water (290-400°C) and prolong the surviving period under the

extremely high-temperature steam environment (≥1200°C) once LOCA happens[89]. In the aspect of mechanical properties, high-temperature strength, resistance to embrittlement, plastic deformation and burst failure are desirable for ATF under LOCA and RIA[89], [90]. Considering that the flammable hydrogen generation due to Zirconium alloy corrosion may lead to massive explosion under LOCA, chemical stability under normal and emergencies is commanded to reduce the oxidation rate and ensure uniform corrosion to evite a sudden accident and maintain adequate service time.

1.3.2. Potential ATF designs and problems

In an attempt to develop the ATF cladding, a large range of approaches has been explored. Based on the recent researches on ATF claddings, three potential approaches were considered promising, such as new super-alloy to replace zirconium claddings, composites claddings, and protective coating techniques. According to the requirements for ATF claddings, high-temperature steam (HTS) oxidation test was designed to simulated LOCA condition, which is used to determine the oxidation resistance of potential ATF materials. Most of the researches on ATF materials followed the accidental conditions and conducted a steam test to evaluate the potential of the candidate materials.

1.3.2.1. Complete replacement of Zr claddings

According to accumulated understanding of high-temperature performance alloy and development of manufacturing technology, zirconium has achieved excellent performance under corrosion, creep, irradiation growth, and wear. However, embrittlement issues related to hydrogen under accident condition are still unresolved due to Zr inherent limitations, such as high-temperature steam oxidation, loss of ductility, ballooning as well as burst. Full replacement of zirconium claddings by advanced super-alloys and composites claddings have been explored widely.

Silicon carbide fibre-reinforced SiC matrix (SiC/SiC) composites claddings, and ferrite-based superalloy claddings were the well-studied candidates. SiC has been chosen as potential cladding material due to its low neutron absorption compared to Zr, stability under irradiation in terms of swelling and geometric changes, and its retained strength under high temperature. In general, these characters fitted well with the requirements under LWR environments. However, SiC as a ceramic material showed brittle intrinsic property and relative lower thermal conductivity, which made it challenging to fabricate and maintain mechanical properties. Nevertheless, recent reports showed that radiation could undermine the SiC component under LWR environments [91].

Ion-based alloy (FeCrAl) was considered as cladding materials in LWRs, due to its good resistance against oxidation/corrosion and high thermal mechanical strength compared to Zr alloy [13], [92]. Their superior oxidation resistance was because FeCrAl alloys are alumina-forming and chromia-forming alloys. And ferrite steels showed orders of magnitude lower reactivity with superheated steam [75]. PM 2000 (an alumina forming alloy) and Fe-25Cr (a chromia-forming alloy) obtained superior oxidation resistance under 8h 1200°C steam environment while Zy-2 suffered entire oxidation of the cladding materials, shown in Figure 1-20 [93]. A protective α-alumina layer tended to form under PWR condition, while a continuous chromia layer was usually formed first after the high-temperature steam attack [75], [94]. The composition of FeCrAl alloys should be selected for an appropriate combination to achieve proper properties. Cr was limited between 16wt% to 21wt% to provide sufficient corrosion resistance under PWR condition [95]. Al should exceed 5wt% to provide protective α-alumina but avoiding excessive amount causing embrittlement [94], [96]. The optimised design of FeCrAl cladding could minimise the fluctuation of the axial temperature and significantly increase the gap closure time, but it could cause increased the fission gas and fuel temperature [97]. No significant differences occurred in the PWR operation condition and design basis accidents compared between FeCrAl claddings and Zircaloy claddings, while FeCrAl cladding would impede oxidation and hydrogen generation at beyond design basis [98]. However, due to the higher neutron absorption [97], FeCrAl

claddings anticipated thinner in thickness [99], which required higher strength. What's more, its high ductile-brittle transition temperature (DBTT, -4°C) [100] and work hardening effect under irradiation [101] have been concerns of FeCrAl alloys for ATF applications.

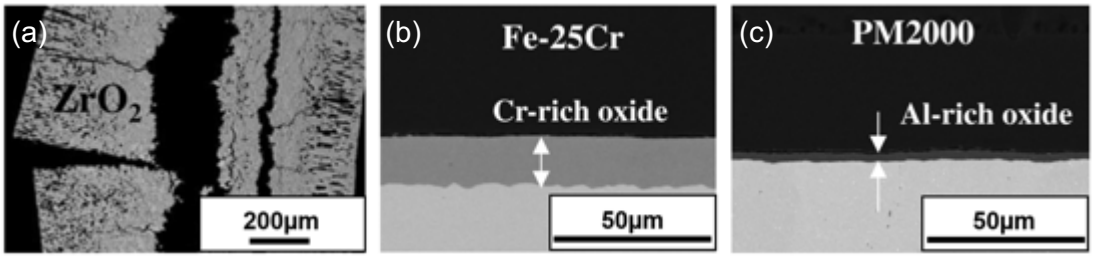

Figure 1-20 Cross-section micrographs of (a) Zircaloy 2 (b) Fe-25Cr and (c) PM2000 after exposure for 8 h in 1 MPa 1200°C steam [77]

1.3.2.2. Protective coating system

Instead of metallurgical alternations on Zr alloys or complete replacement of claddings, protective coating technique has been considered as the most economical and time-saving way to develop ATF claddings. Since the materials that capable for LWR claddings are minimal, a large concentration of alloying elements may undermine the LWR performance of Zr claddings, such as neutronics performance and physical-mechanical properties. Numerical coating materials have been studied in recent years, including ceramic coatings, such as carbide, oxide and nitride; and metallic coatings, such as pure metal, intermetallic and alloy [89], [97], [102], [103]. The coating techniques include thermal spray and sputtering deposition.

1.3.2.2.1. Zr-containing coatings

Metallic and ceramic coatings containing Zr were the priority consideration, according to its intrinsic low thermal neutron capture cross-section and the expected strong bonding with Zr-cladding substrate. $ZrSi_2$ coatings (~3.9μm) deposited by magnetron sputtering on zirconium substrate have been studied. The oxide layer of $ZrSi_2$ consisted of an alternative SiO_2 and ZrO_2 micro- and nano-layer structures, which was formed by the decomposition of spinal Zr-Si-O oxide phase. The intermetallic phase of $ZrSi_2$ coatings exhibited a superior oxidation resistance of almost two times of magnitude

comparing to bare Zy-4 after 20 hours of air oxidation under 700°C. Five hours pre-oxidation test was determined to be the best treatment for the $ZrSi_2$ coatings oxidation resistance performance on the Zy-4 substrate in HTS. After high-temperature oxidation tests, spallation or cracks did not present in the $ZrSi_2$ coating due to the air cooling. [104] Aluminized Zy-4 with a 20μm thick single $ZrAl_3$ phase intermetallic layer using pack cementation diffusion process for 20 hours at 600°C demonstrated an improvement of oxidation resistance and mechanical stability under HTS at 800°C, compared to un-coated Zy-4. However, the aluminised Zr-4 obtained a more substantial weight gain under normal LWR conditions compared to bare Zy-4, which was not desirable for ATF materials [98] . Al-Zr intermetallic coating, formed on Zircaloy claddings surface by magnetron sputtering of Al associated with heat treatment, performed excellent oxidation resistance with 0.7μm thick oxide layer after 800°C 2h oxidation test, while bare Zircaloy formed 8 μm. However, the intermetallic AlZr coating lost protection when oxidation occurred at 1000°C [105].

1.3.2.2.2. Aluminium and chromium coatings

Aluminium and chromium are two superior oxidation resistance metals which forms a dense oxide layer at the surface during oxidation and prevent further oxidation. Alumina served as a protective oxide during HTS exposure. And Cr_2O_3 showed well to waterside corrosion [106]. Ion-based (FeCrAl) alloys as a protective coating for zirconium claddings showed more critical issues during multiple studies. FeCrAl, CrAl, Cr and Al coatings with various composition were examined under steam environment and simulated LWR conditions. FeCrAl coating system with over 18 at% Al created an aluminium-based oxide protecting the underneath alloy at elevated temperature (700°C steam), which demonstrated as parabolic growth [107]. However, sufficient protection for Zy-2 substrate could not be attainable from FeCrAl coatings once the steam temperature reached 1200°C, due to the Fe-Zr eutectic at 950°C which may render the loss of coating by diffusion and melt [94], [108]. FeCrAl coatings failed after the stimulated loss-of-coolant test as a result of the inter-diffusion between the coating and

Zy-4 substrate which caused inadequate protection. As a result of inter-diffusion, intermetallic binary or ternary phases, such as $Zr(CrFe)_2$, $FeZr_2$ and $ZrCr_2$ with oxygen dissolved, was formed between FeCrAl coating and Zy-4 substrate with a layer of Zr-depleted zone. Within the intermetallic region, due to the difference in Gibbs free energy of Fe and Zr, Zr oxidised before Fe due to inward oxygen diffusion and formed ZrO_2 beneath coatings [109]. According to the simulated BWR corrosion test, outward aluminium depletion occurred from the FeCrAl coatings, and it left porosity within the coating due to the counter flow of vacancies [110]. To overcome the eutectic issues and intermetallic phases, CrAl and Cr coatings were applied and proved better steam resistance compared to FeCrAl coatings at 700°C. While at 1200°C, these coatings could only provide 5 minutes delay of the oxidation and continue oxide at speed comparable to uncoated Zircaloy.

Selected concentrations of CrAl coatings were able to impede rapid oxidation of Zr substrate under 700°C steam oxidation; however, no significant protection was observed under 1200°C steam test. Pure cubic γ-Al_2O_3 was formed on CrAl coating with relative high Al content, while a mixture of Cr_2O_3 and Al_2O_3 was confirmed to build with relative low Al content after 700°C 20 hours steam test. Meanwhile, intermetallic phases were detected at the interface of CrAl coatings and Zy-2 substrate after steam exposure [98].

Arc ion plated Cr film could provide enhanced oxidation resistance to Zy-4 claddings, remarkable verities marked in the inner and outer surface of Zy-4 claddings, see Figure 1-22. Cr-coated Zy-4 after 60 days autoclave test gained around 5mg/dm^2, while Zy-4 sheet gained over 25mg/dm^2 [111] Inter-diffusion between Cr-coating and zirconium substrate forming intermetallic layer was still a detrimental issue causing failure [112]. Further surface modification, such as oxide dispersion strengthening (ODS), could obtain better corrosion resistance and improved mechanical properties such as creep, high-temperature deformation and wear resistance [106].

However, under high temperature (1000-1300°C) oxidising environment, Cr_2O_3 could be less HT steam resistance, and continuous oxidisation lead to the formation of volatile CrO_3 and $CrO_2(OH)$. The reaction between Cr_2O_3 and O_2 to form gaseous could damage the protective scales due to the linear steady-state weight loss, which may lead to the reduction in Cr oxide layer thickness [113]. What's more, CrO_3 is toxic, which could also be a severe environmental issue.

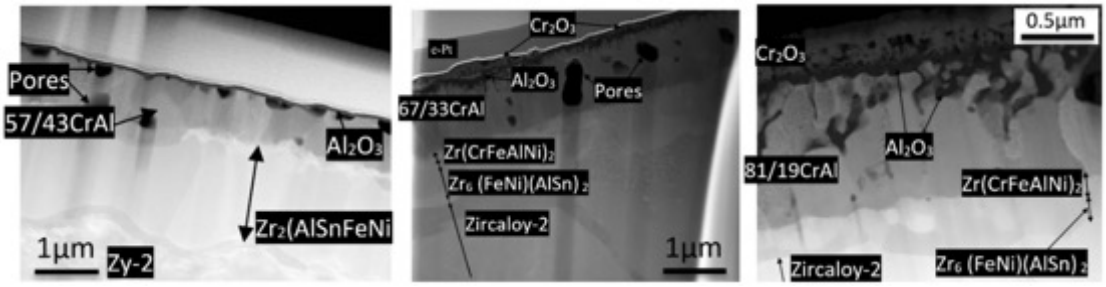

Figure 1-21 STEM cross-sectional images of CrAl coatings after 20 hours HTS exposure under 700°C, layers of Cr_2O_3 and Al_2O_3 were observed associated with pores. A layer of intermetallic was formed between CrAl coatings and Zy-2 substrate

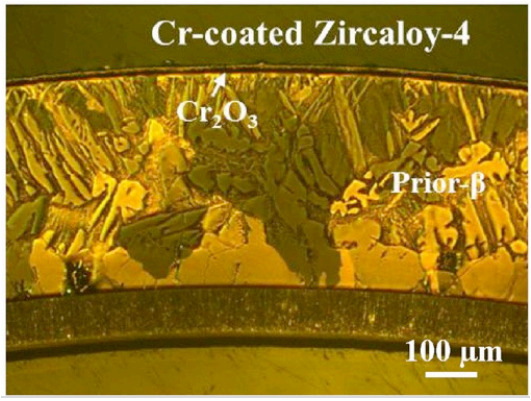

Figure 1-22 Reflected light optical micrographs of the oxides formed on the Cr-coated Zircaloy-4 in 1200°C steam for 2000 s [114].

1.3.2.2.3. Silicon coatings

Si-coated Zy-4 only formed few micro-meters oxide layer after the 2000s 1200°C steam test [115] and performed as a corrosion barrier on the Zr surface; however, plasma sprayed Si coating was not able to provide sufficient adhesion after high-temperature oxidation test due to its intrinsic brittleness. Temperature-activated Zircaloy protection with yttria-stabilised zirconia resulted in a much lower weight gain at long-term 700°C high-temperature steam test; however, Y was detrimental to HTS performance as a result of oxidation [98].

Gaining of safety margins for BDBA conditions requires oxidation resistance to be maintained for a relatively shorter period around hours, compared to tens of thousands of hour's lifetimes for PWR operation. Hence, although the so far studied chromia-, alumina-, and silica-forming materials are not suitable for long-term steam protection, they could provide more extended surviving margins to some extent under LOCA scenarios.

1.4. Coating materials selection for ATF design

1.4.1. Transition metal nitride coatings

Transition metal nitride coatings have been proved to enhance wear, oxidation and corrosion resistance at high-temperature and widely used on cutting and press tools. This type of coating is advantageous in terms of prolonged service lifespan and enhanced performance due to its extremely hard surface and maintained toughness as well as low friction coefficient, excellent adhesion, good electrical and thermal conductivity [116]–[120]. Recent studies on transition metal nitride coatings for steam resistance became popular [121], [122].

Typical morphology of TiN coatings is columnar growth structure associated with defects (pinholes, porous and cracks), which appears to be the weak point for corrosion to penetrate the protective coating [123]. The TiN coatings degradation is due to the growth of titanium oxide TiO_2 associated with pore formation. The oxide formation was as a result of the progressive displacement of N of oxide layer and unaffected layer. The coating surface started to be unstable lower than 500°C oxidation [124].

The corrosion resistance of the TiN coating depends on the number of penetrated defects, such as voids, pinholes, pores and cracks in the TiN layer [118], [120], [125]–[130]. The typical columnar structure with those defects and even delamination could perform as a transport path for the corrosive environment to penetrate the protective coating and interact with the substrate. The microstructure of TiN could be optimised from columnar grains with defects to a denser structure without voids by increasing the bias-voltage during magnetron sputtering [131]. Dense TiN coatings deposited by

filtered cathodic vacuum arc deposition (FVAD) could act as an effective hydrogen barrier compared to columnar grains TiN coatings with voids [132].

1.4.2. Nano-composite TiN based coatings

1.4.2.1. Morphology of TiSiN and TiAlN

Based on the water corrosion mechanism with significant effects of hydrogen and defects, refined microstructure is desired for ATF coatings. By adding C, Si, B, Al, etc., to TiN during deposition process, fine and nano-sized structure could be formed. It was reported that the nano-structure could further enhance the mechanical and thermal properties. The preferential growth orientation of TiN transfer from (111) to (200), which may lead to the grain refinement of the (Ti, Al, Si)N crystallites and reduction of residual stress in the crystal lattice. [133]

TiAlN coatings consist of cubic crystal structure which is obtained by the substitution of Al in the cubic TiN phase. When Al percentage exceeds 50%, hexagonal wurtzite structure AlN gains start to precipitate at the TiN cubic crystalline grain boundaries.[15]

With an increment of Si content, the morphology transforms from pyramid shape (surface morphology of coarse columnar grains) into fine columnar grains and eventually to amorphous structure associated with grain refinement and reduction of surface roughness. By increasing the Si content to some extent, amorphous SiN_x phases are formed around the cubic TiN phase, which limits the grain growth of TiN and therefore results in the grain refinements [123], [134]. The microstructure of the TiSiN was confirmed to compose a nano-crystalline face-centred cubic (B1 NaCl crystal structure) TiN phase and amorphous Si_3N_4 matrix by XRD and XPS [135], [136], [133], [137], [138]. However, continuously increase the Si concentration in TiSiN coatings could form a $TiSi_2$ phase which exhibits less effect on the grain refinement compared to SiN_x. When the Si content exceeds 10mol%, nano-crystalline $TiSi_2$ with the size of 3nm starts to precipitate within the amorphous SiN_x matrix [139].

1.4.2.2. Corrosion resistance of TiSiN and TiAlN

$Ti_{0.70}Si_{0.30}N_{1.10}$ showed 100 times better oxidation resistance compared to TiN at 600°C air oxidation [138]. TiSiN with 11.3wt% Si achieved the best corrosion resistance with 77% protective efficiency [123]. TiSiN coating stayed intact after 1-hour oxidation at 800°C in air. However, the TiAlN coating was impaired completely after 800°C oxidation [124], [140].

$Ti_{1-x}Al_xN$ showed a parabolic oxidation rate constant in air corrosion and formed a passive double layer structure [145,148,149]. The passivity of TiAlN in air was as a result of the formation of protective α-Al2O3 layer [15]. The double layer structure proceeded by outward diffusion of Al to form Al-rich oxide at the topmost surface and inward diffusion of O to form Ti-rich oxide at the interface to TiAlN, shown in Figure 1-23 [15]. However, under supercritical water corrosion test, corrosion resistance performance of TiAlN was not compatible as air oxidation, shown in Figure 1-24 [14], [141]. The degradation of TiAlN in a supercritical water environment was due to the formation of detrimental AlOOH boehmite phase [121], [141]. However, the corrosion resistance of TiAlN could be optimised by multi-layered structure coatings. The mass gain of multi-layered TiAlN/TiN coatings was quite promising, only 1-3mg/dm^2, compared to uncoated ZIRLO substrate, 20mg/dm^2 after 33 days autoclave test [121].

The oxidation resistance of TiSiN was due to the formation of the passive SiO_2 layer and suppress the penetration of oxygen to interact with TiN to further form TiO_2 [137]. The content of amorphous phase Si_3N_4 was the critical component for the oxidation resistance of TiSiN coating. The superior oxidation resistance of TiSiN coating was attributed to the continuous covered monolayer amorphous Si_3N_4 phase on the surface [140].

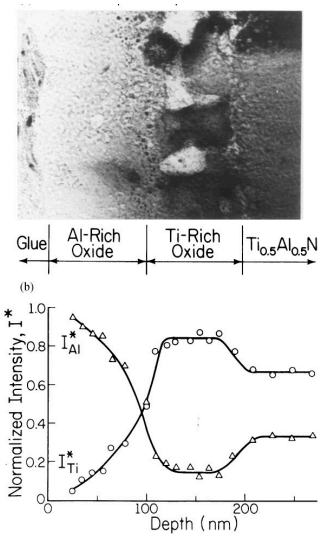

Figure 1-23 Cross-sectional TEM image of the oxide double-layer formed on a Ti-Al-N film after 800°C for 5-h [15]

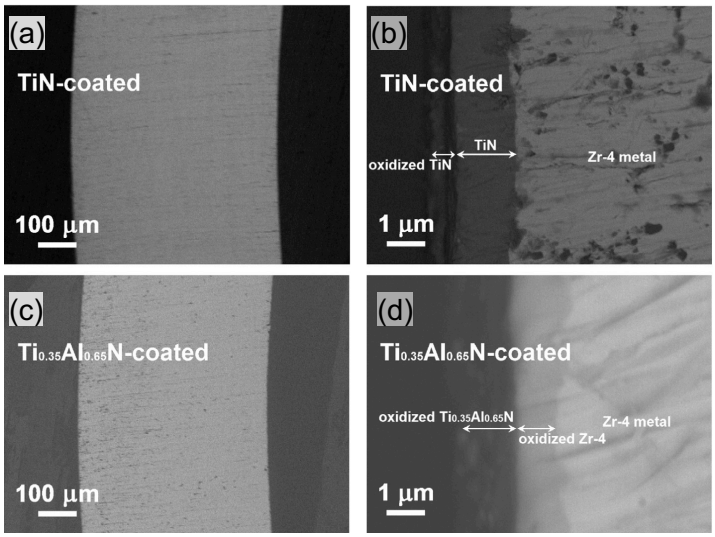

Figure 1-24 SEM images of the cross-section tube after SCW test [141]

1.4.3. Interlayer Double layer structure

The degradation of the corrosion resistance layer could be described as the dissolution of the substrate due to the existence of open defects leading to the formation of a galvanic cell and collapse of thick coatings due to the compressive stress. Therefore, to avoid the interconnection between corrosive environment and substrate, an physical barrier between the protective TiN coating and the substrate was desired to coatings to enhance the corrosion resistance [131]. For this purpose, multi-layered structure and outer layer with strictly controlled defects have been reported by using advanced deposition techniques and parameters.

Consider the influence of thermal mismatch between coatings and substrate, alignment interlayer is required to provide sufficient bonding between coating and substrate and reduce thermal stress during normal operation and accident scenario [142]. Table 1-5 shows the thermal expansion coefficients of the materials involved in this study. Ti interlayer could perform as a bonding layer between TiSiN coating and Zircaloy-4 substrate to reduce the thermal mismatch during heating and cooling.

Ti interlayer could provide a hydrogen barrier in between with the corrosion resistant TiSiN coating and Zr-alloy substrate to suppress hydrogen permeation, substrate phase transformation and maintain mechanical properties of Zr-cladding [142]. The Ti layers

was applied not only to reduce the hydrogen sorption rate but also to trap the penetrated hydrogen [132]. A thicker Ti interlayer was found with a significant improvement of the corrosion resistance. The corrosion resistant mechanism of thicker Ti interlayer was to build a diffusion barrier between the substrate and environment, and reduced diffusion coefficient due to the reduced gradient of the through-thickness defects. [131]

Table 1-5 Thermal expansion coefficient of materials [143]

	Thermal expansion coefficient ($°C^{-1}$, RT)
Zr	5.8×10^{-6}
Zr	6.9×10^{-6} (500°C)
Zircaloy-4	6×10^{-6}
ZrO_2-Monoclinic	7×10^{-6}
ZrO_2-Tetragonal	12×10^{-6}
TiSiN	9.4×10^{-6}
Ti	8.5×10^{-6}
Ti	10.1×10^{-6} (1000°C)
TiO_2-Anatase	10.2×10^{-6}
TiO_2-Rutile	7.14×10^{-6}

Mechanisms for coating corrosion resistance enhancement:

1. **Physical barrier** - by applying non-defect interlayer or by modify deposition parameters to avoid defects, such as pores, cracks;
2. **Anode polarisation** - by adding more positive particles (Si_3N_4) to inhibit localised corrosion and mainly
3. **Grain refinement** – by adding Si to lead homogenous corrosion;
4. **Texture evolution** - by adding Si to change the crystal texture to close-packed plane direction with higher dissolution resistance (higher binding energy).

1.4.4.Coating deposition technique

The protective coatings for ATF are designed to offer a more efficient and better corrosion resistance of zirconium alloy. Various coating techniques have been examined on top of Zr-alloy, such as thermal spray, physical vapour deposition (PVD), and chemical vapour deposition (CVD) to enhance the performance of ATF claddings [6], [104], [144], [145]. TiN has been deposited by arc ion plating technique [129],cathodic arc plasma method [120], plasma enhanced chemical vapour deposition

[117], [136] and DC magnetron sputtering technique [146] and reactive rf magnetron sputtering [125] and plasma activated electron beam physical vapour deposition (EB-PVD) [147].

Thermal spray is a widely used coating technique for relatively thick coatings. The feedstock materials are usually in powder or wire form. The process is based on a spray of melted materials in the form of micrometre-size droplets to the substrate surfaces, which solidifies as a coating. The feedstock materials are melted by electrical or chemical means. It can produce coatings on the large surface area with a high deposition rate compared to other deposition techniques.

CVD involves chemical interaction between mixed source materials and volatile precursors, such as halides or hydrides, under vacuum. Deposition of coatings on the substrate surface occurs associated with volatile by-products removal when forced convection is applied to the deposition chamber. The process is extremely versatile due to the productivity of a wide range of elements and compounds. CVD can produce high purity and high-density thin films to irregular surfaces, such as screw threads and recesses, which is one of the biggest advantages. CVD can also be accelerated by heat, plasma or various methods to do mass production, which is relatively economical process technique. It has been applied to produce monolith SiC inner, intermediate and outer layers for SiC_f/SiC composite ATF tubes[144], [148]–[150].

PVD process includes three steps under the high-vacuum condition. First of all, solid target materials are vaporized by high-power electricity or laser. Then, the gas formed target atoms transport through a reacting chamber by the force of the electric field. At last, the target atoms consolidate directly or react with gas spices at the substrate surface and form coating. The coatings deposited by PVD are usually extremely hard, corrosion–resistant, and high-temperature resistant. Various PVD techniques are used in a wide range of applications, such as fabrication of microelectronic devices, batteries and fuel cell electrodes, diffusion barriers, optical and conductive coatings and surface modifications. PVD is believed as a promising candidate for ATF coatings due to its

required low substrate temperature to maintain the mechanical properties of Zr-alloy during the deposition process.

To acquire a functional oxidation-resistance coating, the following list of criteria is desired[105].

1) Excellent adhesion to the substrate associated with a thermal expansion coefficient similar to that of the Zy-4 substrate to minimise interfacial stresses
2) Smooth surface with low roughness
3) Free from microspores and through-in cracks
4) Manufacturable at low enough temperature to avoid substrate microstructure change
5) Minimal side-effects on neutronics performance

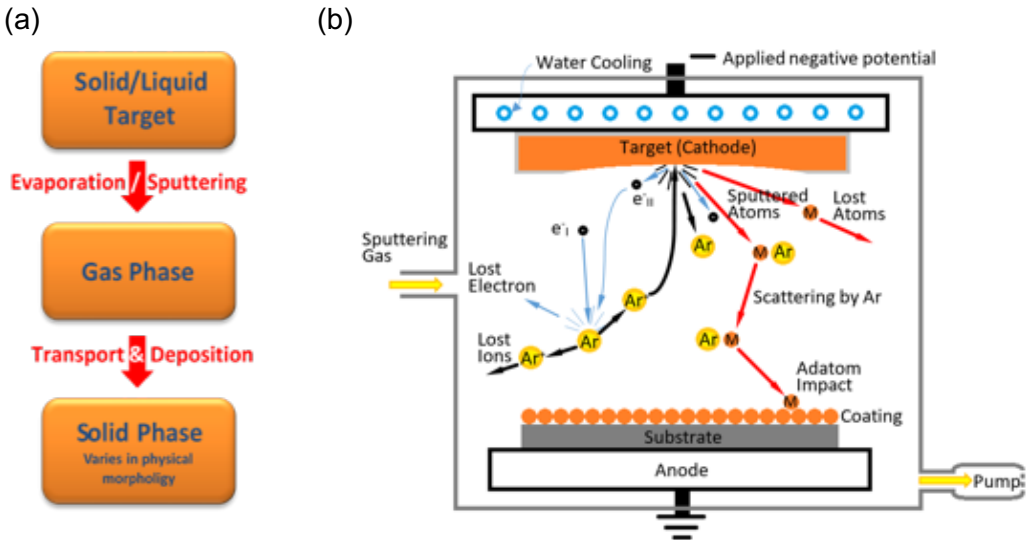

Figure 1-25 (a) Three fundamental steps of the PVD process and (b) schematics of the PVD sputtering process

The basic PVD processes are classified into thermal evaporation and sputtering. The fundamental steps of a PVD process are summarised into three, see Figure 1-25, (1) Vaporization of the target sources from the solid or liquid state by ion bombardment (sputtering) or heating (thermal evaporation); (2) Transportation of the vapour in vacuum or partial vacuum chamber to the substrate surface; (3) Condensation of targeted thin film on top of the substrate surface. The basic sputtering process of PVD is that the energetic ions (Ar+) extracted from an electropositive plasma due to the

applied voltage bombard with the target surface. The ion bombardment collides out target atoms attached to the substrate surface and form a dense, adhered coating.

This paragraph gives a brief description of the fundamentals of the PVD process. The applied negative potential to the target plate (attached with magnetrons) generates a glow discharged plasma between the substrate and the target cathode. The plasma contains energetic ions (Ar^+ and N^+ in this work) and free electrons (e^-), which are also called charge carriers. At the same time, the active ions (Ar^+) can absorb free electrons and release energy in the form of light, which cause the glow of the plasma. A small number of charge carriers, such as primary electrons (e^-_I) and Ar^+, initially exist in the sputtering gas generate a mild current when the voltage starts to apply to the electrodes. As the negative potential increase, it leads to the rise in current density due to the increasing density of charge carriers. A large amount of charge carriers is due to the generation of secondary electrons (e^-_{II}) resulted from the cathode by Ar+ collision with the target surface. The vast free electrons hit the neutron Ar molecules to generate positive ions during their transportation towards the anode.

Meanwhile, the energetic ions flux to the cathode (target). This phenomenon continues until the voltage rise to the breakdown voltage, so-called the *Townsend discharge region*. Once the breakdown happens, the charge-carrier density leads to the increase of current density and decrement of the electrical potential difference concurrently. At this point, the applied electrode voltage is high enough for Ar^+ to collide the target surface and generate secondary electrons continuously. That is to say, the plasma is self-sustaining (*normal discharge region*). In the stable process, the electrons travel from the target plate (cathode) towards the substrate (anode). While, the energetic ions (normally Ar+) accelerated by the electric field physically bombard the target surface and collide target atoms out and towards the substrate, so-called sputtering. The sputtered target atoms react with the energetic nitrogen atoms near the surface of the substrate and collide the substrate to form a condensed and adhered coating.

A basic sputtering system combines a cathode target and an anode substrate facing each other associated with plasma in between, see Figure 1-25 (b). The target works as the source of the coating raw material as well as the source of secondary electrons which sustains the plasma. Due to the energy of ion bombardment, the target usually is water-cooled to avoid melting. Although the density of charge carriers is five orders of magnitude lower than that of feedstock gas, the charged particles play the core roles in sustaining plasma discharge and in the sputtering process. The free electrons play roles of dissociation of the feedstock gas (nitrogen in this work) and ionisation of gas (argon) to create the positive ions that subsequently bombard the target surface. The energetic ion bombardment is used to clear inhibitor films on the target at the beginning of sputtering, physically sputter target atoms towards the substrate and increase the reaction rate.

The deposition rate is a core index of the PVD process, which is ideally desired to be as high as possible to meet the requirements of mass production and achieve a good quality coating without cracking. The deposition rate is determined mainly by the efficiency of ion bombardment and also by the efficiency of atoms attached to the substrate. The efficiency of ion bombardment can also be described as ionisation efficiency. The former determining factor is related to the power density applied to the target, working gas pressure, size of erosion area and source materials intrinsic properties. The high ion current is desired to achieve a reasonable sputtering rate, which can get from higher power density. However, melting or sublimation of target should also take into concern. The energy needed to collide off target atoms and the melting temperature of the target restrict the range of the applied voltage. The latter factor is more associated with the source-substrate distance, and also the feedstock gas pressure. Relatively low pressure is demanded due to the loss of sputtered atom caused by colliding or scattering with the plasma particles. What’s more, some control factors are interrelated, such as gas pressure and power density.

Magnets are commercially applied attached below the target for the sputtering process (Magnetron sputtering deposition) to significantly enhance deposition rate. It is due to the significantly enhanced ionisation efficiency by the applied magnets. During the magnetron sputtering procedure, the magnetic field strength can influence the electrons but not the ions due to its value (few hundreds gauss). It can trap electrons within the vicinity of the cathode and modify the trajectories of electrons to only move perpendicular to the magnetic field lines (Lorenz-force), see Figure 1-26. As a consequence, it increases the chances to collide with gas atoms and decrease the number of loss electrons. Due to the enhanced ionization efficiency, the sputtering process can achieve a higher deposition rate at relatively low pressure with high current density at low voltages.

Magnetron sputtering has been used for the deposition of a various range of coatings for industrial applications, such as hard, wear-resistance, low friction coatings, decorative coatings and electrically conductive coatings. According to the configuration of the magnetic field, balanced and unbalanced magnetrons have distinctive features. Normally, the balanced MS is designed to avoid energetic particles bombardment onto the coating surface, which is widely used for microelectronics. However, such ions bombardment is desired for sputtering hard coatings, which can be achieved by unbalanced magnetrons. It is also possible to alter the magnetic fields to cover both target and substrate with plasma to further enhance the ionisation efficiency, which is called closed field. The advanced closed-field unbalanced magnetron sputtering is a widely applicable technique for the deposition of high-quality, well-adhered films which is qualified for a protective coating for crucial environment use. Also, the advanced magnetron sputtering incorporates multi-source ‘closed-field’ system, which is capable of depositing a broad range of materials with the complex composition at an efficient rate.

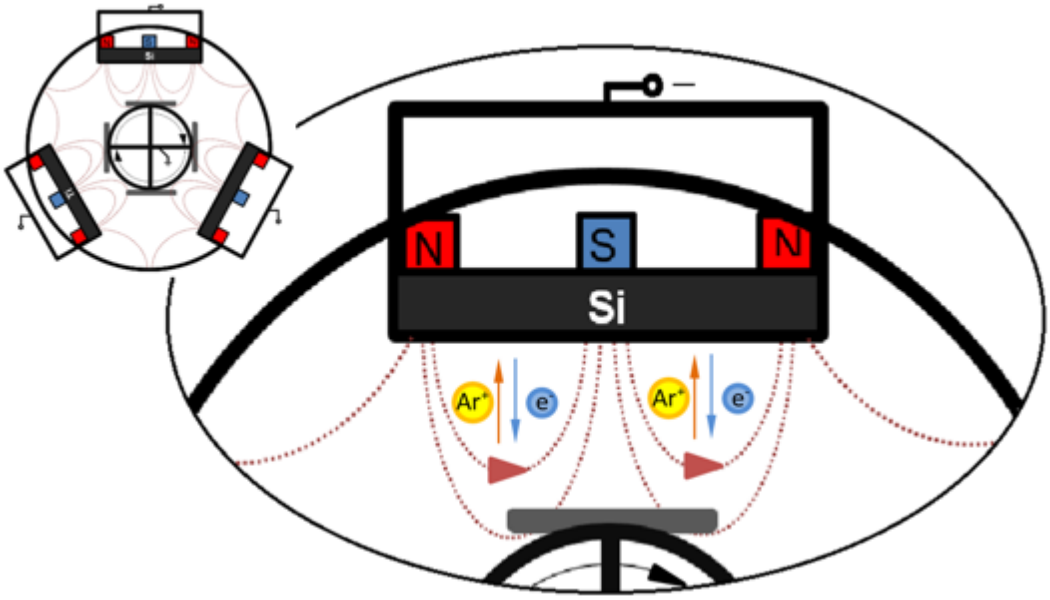

Figure 1-26 Schematics of a closed-field unbalanced magnetron sputtering deposition and the charged particles movement illustration.

2. Experimental procedures

2.1. Substrate preparation

To obtain highly reliable results of corrosion resistance of TiN coatings, the primary commercial alloy Zy-4 was chosen as a substrate. The chemical concentration is listed in Table 1-3. Before the magnetron sputtering process, the Zircaloy-4 alloy plates were cut into 15mmx15mm pieces by EDM (electrical discharge machining) and further deduced to 5mmx5mm by high-speed diamond saw. Each plate was manually ground with round edges to ensure good adherence near the edges and corners. Then, the substrate samples were mounted with TransOptic Powder. The resin formed by this particular powder could be easily removed by heating to 300 °C after grinding and polishing avoiding surface damage or oxidation. The mounted Zircaloy-4 substrate plates were manually ground on silicon carbide paper following a 120, 400, 800, 1200-grit sequence with controlled time (less than 60 seconds) to minimise the material loss. Each step grinding needs to fully remove last step scratches. After the finest grinding, the substrate was coarsely polished by automatic polishing machine 6μm diamond paste and an oil-based lubricant on napless cloth. The coarse polishing required two times 10 minutes automatic polishing with 30N individual force and opposite rotation of the specimen holder and polishing cloth. It was necessary to remove the grinding scratches from 1200-grit silicon carbide paper and polish away the deformation film on the substrate surface (swelling). The fine polishing required OPS polishing for 90 seconds using the mixture of water diluted colloidal silica (0.06μm) and hydrogen peroxide (H_2O_2) at the ratio of 5:1. Between each step of grinding and polishing, the substrate samples were ultrasonically cleaned in distilled water. The flat and shiny surface could be obtained to ensure the good bonding between the coating and substrate during the magnetron sputtering process.

Table 2-1 Chemical composition of Zircaloy-4 by weight percentage

Elements	Sn	Fe	Cr	Zr
Zircaloy-4	1.53	0.26	0.1	Bal.

2.2. Magnetron sputtering process

The ternary $TiSi_xN/Ti$ coatings with various Si content were deposited on Zy-4 mirror-finish substrate by closed field unbalanced pulsed DC magnetron sputtering in a Teer Coating UDP350 rig [151]–[153]. The advantage of the adjustable pulsed DC magnetron sputtering was explained by P.J. Kelly [153] with modification of microstructure and crystallinity and enhancement of hardness, adhesion and wear resistance.

Table 2-2 Magnetron sputtering parameters for $TiSi_xN/Ti$ coatings

Sample ID	$TiSi_{0.08}N/Ti$	$TiSi_{0.13}N/Ti$	$TiSi_{0.19}N/Ti$
Target	Ti (99.99% pure) Si (99.99% pure)		
Base pressure	7.1×10^{-6} mbar		
Gas Used(N_2:Ar)	50:50	60:40	50:50
Sputtering pressure	1.21 mTorr		
Deposition time	1.5 hour		
Sputtering power for Ti	1kW		
Sputtering power for Si	150w	300w	400W
Substrate	Zy-4		
Substrate temperature	Ambient		

The sputtering conditions are summarised in Table 2-2. The illustration shows the overall pulsed DC magnetron sputtering system used in this study, see Figure 1-26. The sputtering process mechanism of DC magnetron sputtering was elaborated in Section 2.4.4. The Zy-4 substrate plates were pre-fixed to a rotating holder at a constant speed of 16rpm to minimise the anisotropic grain growth of the thin film. A high-quality magnetron sputtering coating requires two conditions: inert gas environment and smooth surface. The MS rig was vented to reach vacuum overnight and filled with nitrogen gas before sputtering. Highly smooth and flat substrates were promised by strict grinding and polishing procedures. The $TiSi_xN/Ti$ coatings were deposited by co-sputtering from two cathode targets, 99.5% titanium target and 99.9% silicon target with the size of 300mm × 100mm. The sputtering process was driven using pulsed DC mode (Advanced Energy MDX with SPARC-LE pulse unit) at a frequency of 100 kHz and 4.0 μs off time determined upon experience. Ti+ and Si+ were ejected due to the Ar+ bombardment and sputtered onto the Zy-4 substrate under the force of a second

vertically opposed magnetic field to maximise the ion-to-atom ratio incident at the substrate. The target plates were water cooled. The distance between the target surface and the Zy-4 substrate was 8cm. Before sputtering, the chamber was priory vacuumed to a base pressure around 1x10-3 Pa and then refilled to operating pressure (0.16 Pa) with argon flow. Before the deposition, the targets were sputter cleaned by the applied potential at 1kW under vacuum for 10 mins to remove the possible oxide layer or other contaminants, while the substrate plates were protected from target plasma with a shield. To enhance the adhesion of the $TiSi_xN$/Ti coatings, a thin glue layer of Ti was deposited on the mirror polished Zy-4 substrates by a switch on the rotation of substrate holder and the power of Ti target for 10 mins. Then, 1.5 hours standard deposition was processed by switching on the power of titanium target, Silicon target and turning on the nitrogen supply. The Si composition was controlled by the applied potential of Si target from 150W to 400W while the power of Ti target remained constant 1kW The nitrogen percentage was controlled by the N2 flow rate monitored by Optical Emission monitoring (OEM) system to produce stoichiometric $TiSi_xN$/Ti coatings. A bias of -307V between the substrate and Ti target and a various bias of -240V ~ - 300V between the substrate and Si target was monitored by the control panel.

2.3. Simulated LOCA steam test and PWR Corrosion test

To assist in the determination of the coating system, steam tests from 600-1200°C for 1-4 hours were designed to identify the oxidation resistance against steam to simulate LOCA conditions. The experiment arrangement shown in Figure 2-1 was designed to exam the corrosion behaviour of coated samples by water vapour. The steam generation system consisted of Ar gas feeding and water bath heating, which generates steam at water boiling temperature (100°C, 1 atm). The tube furnace with quartz tube was sealed with the steam generation system and cooling system in an atmosphere of high-temperature gas mixture with steam and Ar. All samples were cut into size 5x5mm, then ultrasonically cleaned, rinsed with ethanol and dried for over 8 hours before the steam test. Samples were placed in a ceramic bowl with coating surface or polished substrate surface facing up, which ensured sufficient steam contact. By calculation, to

achieve 90% of water vapour in the mixture gas, the Ar gas flow rate was 0.4L/min deduced form water consumption. Steam exposures were operated for 1-4 hours at the temperature of 600, 800, 1000°C with constant steam rate. The heating and cooling processes were by push the ceramic bowl into and pull it out of the heating zone of the quartz tubes, which gave sharp heating and cooling speed. In this study, ramping time was neglected due to the fast insertion of samples to the hot steam area to exclude heating period oxidation effect on corrosion kinetics, especially at 1000°C. The quartz tube was protected by argon gas during the heating, steam test, and cooling stages to isolate the corrosion effect of oxygen and focus on the corrosion mechanism of water vapour.

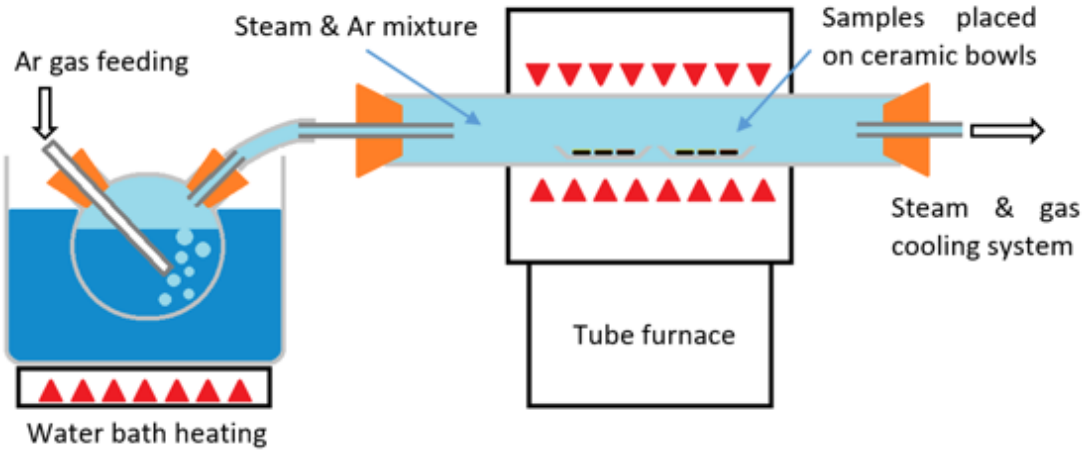

Figure 2-1 Experimental arrangement for the steam test, with steam generation system, heating system and steam & gas cooling system

The corrosion tests were operated in 4650 Series High Pressure and High-Temperature Vessels in the volume of 250ml (model 4651) manufactured by Parr Instrument Company. It could obtain temperature up to 600°C and achieve a maximum pressure of 410 bars. This series vessel came with standardised split ring closure with eight compression bolts and a VGR-T head design that includes a valve, gage, rupture Disc, and thermowell. Due to the volume expansion of water under high temperature and pressure, the maximum water fill of vessel volume is 80ml, 33% of the container volume. Coated samples were cut into size 5x5mm, then ultrasonically cleaned, rinsed with ethanol and dried before the autoclave test. The samples were held in FeCrAl wire weaved loading net to support the sample located at a proper height within the vessel

chamber to ensure the contact with high-pressure water. In order to examine the corrosion resistance capability of each coating, 2 days and 7 days non-interrupted short-term autoclave tests at 360°C and 19.8MPa were conducted.

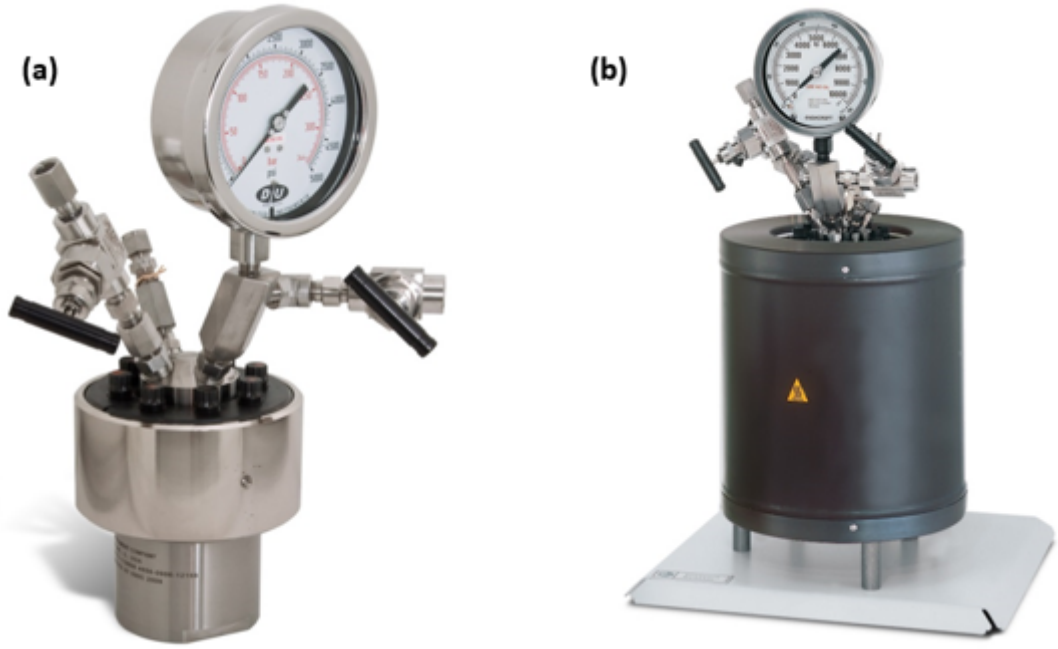

Figure 2-2 (a) High temperature and pressure Vessel Model 4651, 250mL with VGR and Thermocouple and (b) with 4923 Heater

2.4. Characterisation

2.4.1. GIXRD phase characterisation

For the specimen before and after oxidation test in simulated PWR environment, oxide analysis was performed using XRD, AFM, SEM and FIB. First, the phase identification of bulk Zy-4 substrate was performed by Philips X'pert Modular Powder Diffractometer (MPD) XRD with a long fine focus Cu source (λ=1.54Å) for the conventional Bragg Brentano operation (θ/2θ) with 2θ ranged from 20°-110°, step size of 0.02° and at the speed of 4s/step. For the as-deposited $TiSi_xN$/Ti coatings, 2 days and 7days autoclave tested samples, oxidation products were scanned by Philips X'pert MPD XRD using glancing incidence geometry (GI) mode with 2° and 3° to avoid the disturbance of Zr peak and noise and a scan range of 10-90°. The penetration depth of X-ray for ZrN coating was around 1.9μm with 2° incidence angle. The penetration depth of X-ray for $TiSi_xN$/Ti coating and TiO_2 layer were approximately 2.91μm with 3° incidence angle

and 3.37μm with 2° incidence angle, respectively. The penetration values were calculated by Highscore Plus.

2.4.2. Microstructure and element characterisation

The surface morphology of as-deposited $TiSi_xN/Ti$ coatings was analysed using Atomic Force Microscope conducted under taping mode at room temperature, as part of the standard procedure[119]. All the AFM images were collected at a scan rate 1Hz with a resolution of 512 lines per image. The scan area of the coating was 10μm by 10μm. The surface roughness (Ra, average roughness) was calculated based on statistical procedure using NanoScope Analysis 1.9 software. The AFM investigation was used to substantiate the surface roughness and surface particle size, associated with SEM analysis.

To estimate proper magnetron sputtering parameters, the chemical composition of the test trial deposited $TiSi_xN/Ti$ coating was measured by the Zeiss EVO60 tungsten SEM using an accelerating voltage of 20.0keV, the spot size of 300 and a working distance of 8.5mm accompanied with Energy dispersive spectroscopy (EDS) and Oxford instruments Aztec software. The extent of oxidation attack was assessed by the thickness of the oxide layer measured in the sample cross-section by Scanning electron microscopy (SEM). It was difficult to determine the oxidation kinetics by weight change due to the thin MS cracks coatings and precipitations of contaminants of the coating surface. The top surface of the as deposited and autoclave tested samples were then examined by FEI Quanta 650 and TESCAN MIRA3. Cross-section of coated samples was conducted on grand and polished samples by TESCAN MIRA3. Focused Ion Beam SEM (FIB, Helios 660) was used to get a high resolution of the nano-microstructure of the $TiSi_xN/Ti$ coatings.

3. Results and discussion

In this study, the main focus was the different corrosion behaviours of nitride ceramic coatings under high-temperature steam (LOCA condition) and pressurized water (normal operational condition). Steam test aimed to evaluate the corrosion resistance of nitride ceramic coatings under LOCA condition. Autoclave test were designed to simulate the normal PWR condition in order to study the corrosion resistance against water coolant. This chapter includes the results of phase identification and microstructure observation of ZrN, TiN and $TiSi_xN$/Ti coatings in as-deposited state, and after high-temperature steam exposure and high-pressure water corrosion test.

The main results present in the following sequence:

- Comparison between as-deposited ZrN, TiN and $TiSi_xN$/Ti coatings;
- Comparison of as-deposited $TiSi_xN$/Ti series coatings ($TiSi_{0.08}N$, $TiSi_{0.13}N$ and $TiSi_{0.19}N$);
- Steam corrosion behaviours between ZrN and TiN coatings after1h under 600°C and 800°C;
- Steam corrosion of $TiSi_{0.08}N$, $TiSi_{0.13}N$ and $TiSi_{0.19}N$ coatings after 1h, 2h and 4h steam test under 600°C, 800°C and 1000°C;
- Water corrosion of $TiSi_{0.08}N$, $TiSi_{0.13}N$ and $TiSi_{0.19}N$ coatings after 1 to 7 days autoclave tests under 360°C, 194mBar;

Severe corrosion and delamination were found on the surface of ZrN coated samples after 1 hour steam test at 600°C and 800°C, while, $TiSi_xN$/Ti coatings showed excellent steam resistance after 600°C, 800°C and 1000°C steam tests up to 4 hours. $TiSi_{0.13}N$ and $TiSi_{0.19}N$ coatings could survive after 4 hours steam erosion at 1000°C. Further investigation in water corrosion was focused on the $TiSi_xN$/Ti series coatings. Apart from the steam resistance, $TiSi_{0.08}N$/Ti coating showed the best water corrosion resistance after 7 days autoclave test, while $TiSi_{0.13}N$/Ti and $TiSi_{0.19}N$/Ti could not survive for that long period. Details of characterization of nitride coatings before and after steam and autoclave test are given as follow.

3.1. Characterisation of as-deposited nitride coatings

3.1.1. Phase identification

Figure 3-1 illustrated the diffraction patterns of the as-deposited ZrN coating on Zr alloy substrate, TiN and $TiSi_xN$ coatings on Si wafer in GIXRD mode with 2° incident angle. The as-deposited ZrN coating showed ZrN reflections at 33.50°,38.87° (ICDD: 01-080-3718) exclusively with the cubic crystal lattice. Both TiN and $TiSi_xN$ coatings confirmed the existence of cubic TiN crystal structure with main peaks at 36.96°, 42.67° and 61.9° indicating (111), (200) and (220) planes. The X-ray pattern of $TiSi_xN$ coating showed more broadened peaks compare to TiN reference pattern (ICDD: 04-015-2441) which indicated a finer grain in $TiSi_xN$ coatings. TiN with (111) was the preferred phase in as-deposited TiN coating. While, after Si addition, TiN with (200) became the primary phase in as-deposited $TiSi_xN$ coating. $TiSi_xN$ has been proved as a multiphase material with TiN as the predominant phase. Due to the much less of ionic radius of Si^{4+} (0.41 Å) compared to Ti^{3+} (0.75 Å), Si could substitute within TiN lattice at Ti sites forming solid solution[154]. Normally there was a limitation for two ions forming solid solution based on atom size and chemical intrinsic. $TiSi_xN$ with up to 13at% Si content has been proved with TiN crystal structure by XPS analysis[155]. Due to the limitation of X-ray diffraction technique, only crystalline phase satisfy Brag's Law could be identified. So, in this study, possible phases except TiN when Si content over 13at% could not be determined. While the shift of diffraction plane from (111) to (200) indicated the decreased lattice constant of each plane from 2.43 Å to 2.12 Å due to the substitution of Ti by small Si ions[156]. The reduction of crystal lattice spacing in $TiSi_xN$ was due to the structure transformation of TiN caused by the Si implantation in TiN lattice.

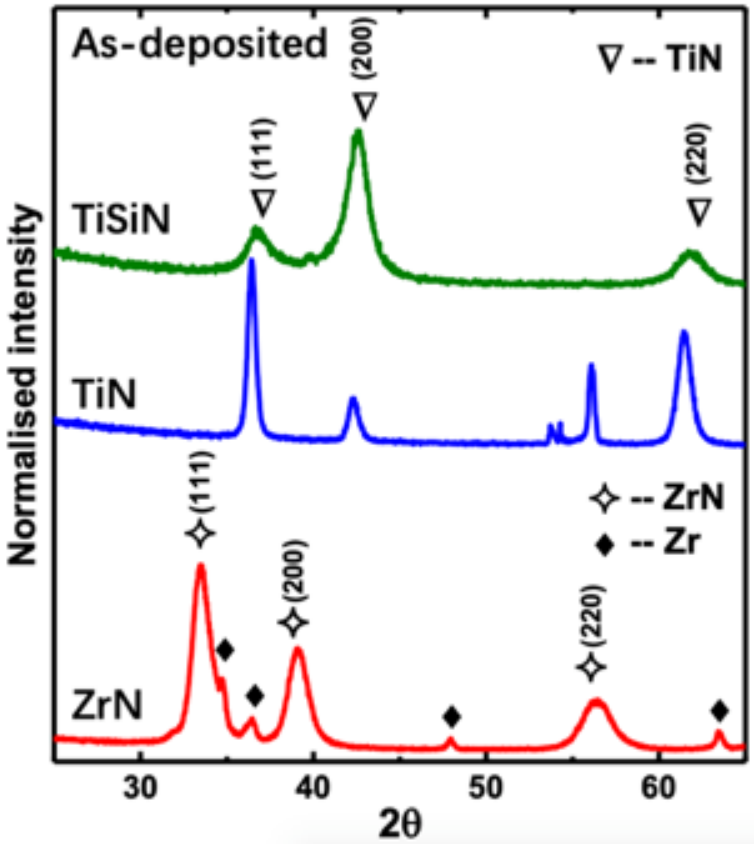

Figure 3-1 GIXRD patterns with incidence angle 2°of as-deposited ZrN coating with Zr substrate, TiN and $TiSi_xN$ coatings with Si wafer substrate

There were some low-intensity peaks of Zr substrate detected from ZrN coated sample due to the penetration of X-ray through coating layer. As X-ray penetration depth of ZrN (1.9μm) was larger than thickness ZrN coating (1.85μm). There was no significant signal from the beneath Si wafer in TiN and $TiSi_xN$ coatings. As the thickness of TiN and $TiSi_xN$ coatings was over 4 μm which was larger than X-ray penetration depth (2.9μm) with 2° incident angle, calculated by Highscore Plus. Also, sample placement needed specified arrangement in order to avoid strong signal from single crystal Si wafer.

Figure 3-2 illustrated the respective diffraction patterns of the bare Zy-4 substrate and all the as-deposited $TiSi_xN$/Ti coatings with various Si content on Zy-4 substrate. As the GIXRD patterns of as-deposited coating samples mainly showed the peaks for zirconium substrate, Zr pattern was used for reference. It was because the X-ray penetration depth was approximately 3μm by calculation while the coatings were all less than 2μm. Zy-4 substrate exhibited a typical hexagonal zirconium diffraction pattern

(ICDD: 04-003-1384). The highest intensity was at about 34.8° diffraction angle, which derived from the Zr (002) diffraction plane.

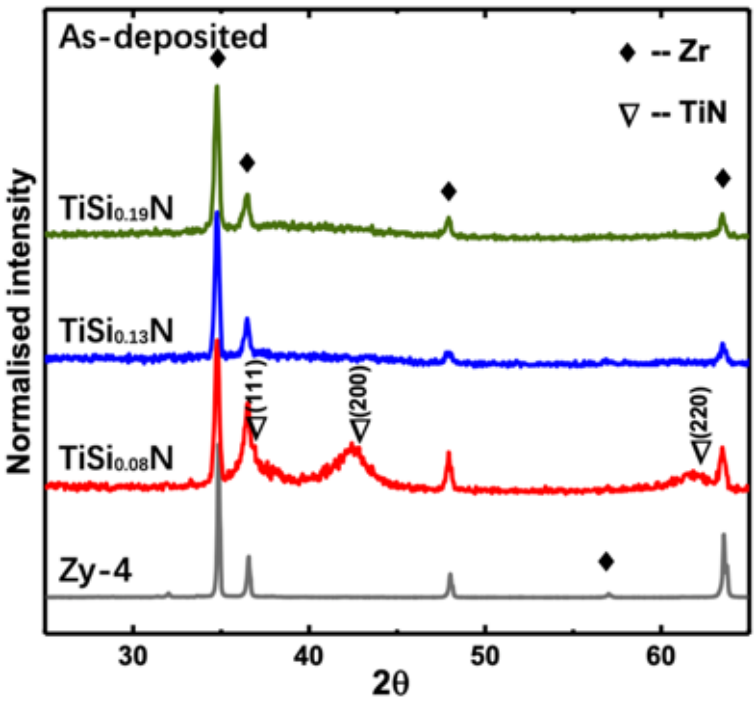

Figure 3-2 GIXRD patterns of the bare substrate and as-deposited $TiSi_xN$/Ti coatings with Zy-4 substrate

No sharp peak was identified as crystalline formed TiN among all three as-deposited $TiSi_xN$/Ti coatings, as evident in Figure 3-2. However, two clear broadened peaks at 2θ angle around 41.3° and 62.2° were identified as cubic TiN crystalline (ICDD: 04-015-2441) in the lowest Si-implanted $TiSi_{0.08}N$/Ti coating. From $TiSi_{0.08}N$ XRD pattern, there was a shoulder-like broadening peak accompanied by Zr peak (36.486°) at the range of 35° to 39°, which could be TiN (111). This various diffraction planes was caused by the Ti substitution by Si ions that might vary the growth orientation of TiN[157], which was consistent with the primary diffraction plane shift in $TiSi_xN$ with Si wafer sample shown above in Figure 3-1. The broadened peaks of TiN shown in $TiSi_{0.08}N$ were as a result of fine crystalline grain size and residual stress caused by the high bias voltage ion bombardment and low-temperature substrate temperature[158]. However, the broadened peaks of TiN crystalline were lost as the Si content increased, which indicated that $TiSi_{0.13}N$ and $TiSi_{0.19}N$ coatings were amorphous.

3.1.2. Composition and microstructure characterisation

According to the visual observation (pictures not shown), well-adhered ZrN and TiSixN coatings were deposited successfully onto the Zy-4 substrate and Si wafer by magnetron sputtering deposition system at ambient temperature. ZrN and TiN both showed goldish and metallic lustre. The as-deposited $TiSi_xN$ surface presented metallic lustre with goldish yellow to dark-greyish colour as the Si implantation increasing. All the coated specimens exhibited a smooth and compact surface. No macroscopic defects, such as cracks and delamination, were visible from the coatings surface and substrate edges. It indicated that magnetron sputtering could produce well-adhered and defect-free nitride coatings directly on polished Zr-surface and Si wafer at low temperature.

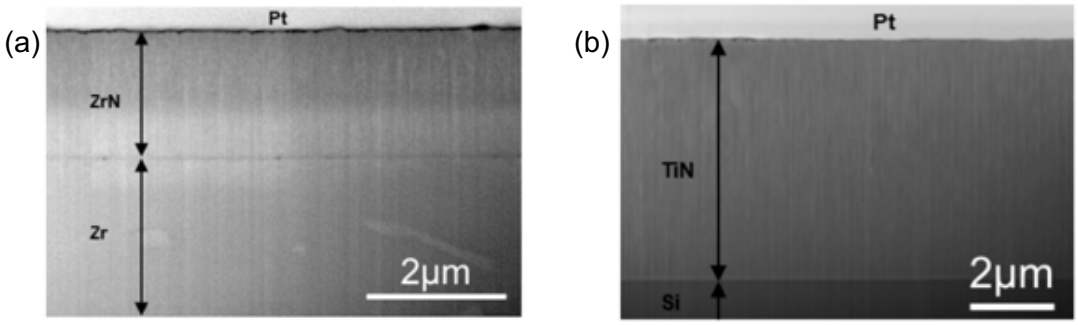

Figure 3-3 Cross-section SEM images of the as-deposited (a) ZrN coating on Zr-Nb alloy substrate and (b)TiN coating on a silicon wafer

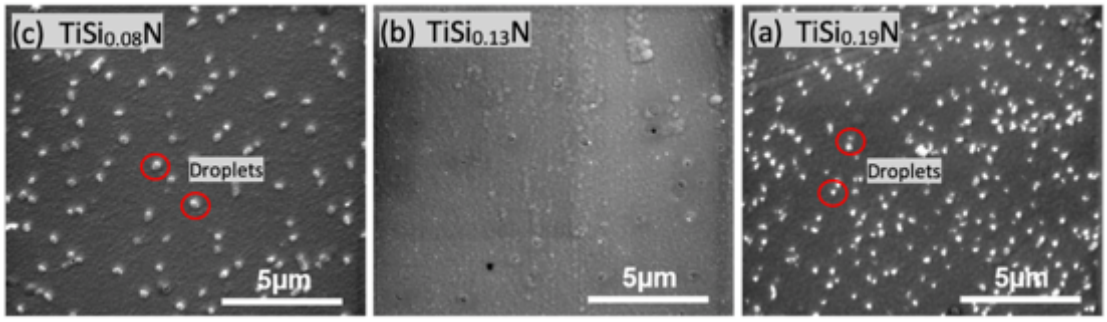

Figure 3-4 SEM images (SE mode) of as-deposited (a) $TiSi_{0.08}N$, (b) $TiSi_{0.13}N$ and (c) $TiSi_{0.19}N$ coatings surface morphology, the white particles are $TiSi_xN$ droplets.

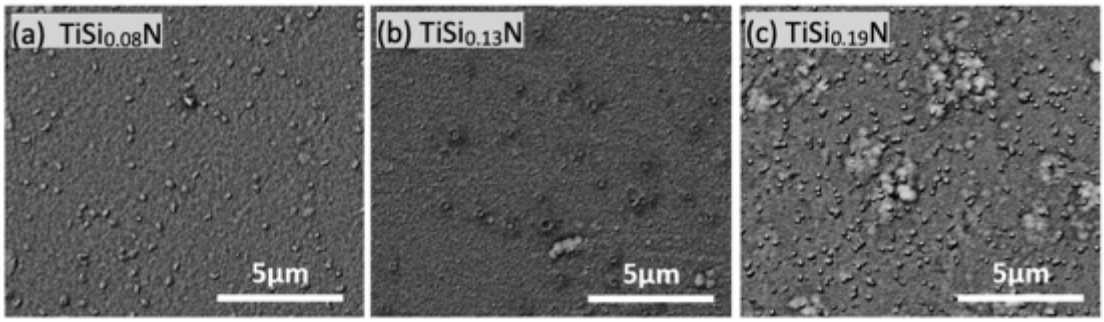

Figure 3-5 SEM images (BSE mode) of as-deposited (a) $TiSi_{0.08}N$, (b) $TiSi_{0.13}N$ and $TiSi_{0.19}N$ coatings surface morphology

Figure 3-3 showed the FIB cross-section of ZrN and TiN layers on zirconium alloy plate and Si wafer. According to the cross-section SEM analysis, dense and uniform ZrN and TiN coatings were deposited by magnetron sputtering. No cracks or voids presented at the interface of as-deposited coatings and substrates or within coating layers. The surface of each coating was relatively smooth, while microstructure did not illustrate clearly from the FIB cross-section images. But TiN cross-section shows relatively clear columnar structure. The thickness of as-deposited ZrN and TiN coatings measured from FIB cross-section SEM images were 1.85 and 5.63 µm, respectively.

Figure 3-4 and Figure 3-5 were high magnification SEM images of each coating surface. All three surfaces show similar nano-grainy structure and only minor variations in grain size. No evident micro-defects such as pinholes, micro-cracks, and unevenness presented under SEM. However, the white particles on $TiSi_{0.08}N$ and $TiSi_{0.19}N$ surface were nano-sized droplets due to sputtering parameters, such as temperature, feedstock gas ratio and power applied. The bright feature of droplets was due to the edge effect of electrons in SEM imaging principles. These surface nano-droplets contain Ti, Si, and N, which was the same as coating material, identified by EDS point analysis. It was also confirmed that these droplets had similar components with the rest surface area, by BSE SEM images (Figure 3-5). $TiSi_{0.19}N$ surface showed the highest droplet density and the smallest droplet size. According to the BSE SEM images of $TiSi_{0.13}N$ surface (Figure 3-5(b)), craters were observed as a distinguish to $TiSi_{0.08}N$ and $TiSi_{0.19}N$-surface droplets. According to the surface morphology and elemental analysis, $TiSi_xN$/Ti

coatings exhibited similar nano-grain structure and uniform elemental distribution through surface area despite morphology difference.

Table 3-1 As-deposited $TiSi_xN$/Ti coatings sample ID, chemical elemental composition (at %), thickness (μm) and roughness (nm) scanned by 10x10μm area and area without large droplets

Element (at %) / Sample ID	Ti	Si	N	Thickness (μm)	Roughness (nm)
$TiSi_{0.08}N$	43.94	7.72	36.72	1.57	6.20/5.38
$TiSi_{0.13}N$	35.72	13.07	40.22	1.78	2.49/2.49
$TiSi_{0.19}N$	37.48	19.16	34.06	1.99	3.94/3.32

Table 3-1 presented the chemical percentage of the as-deposited coatings obtained by EDS surface area scan. The composition of $TiSi_xN$/Ti coatings deposited by magnetron sputtering technique was balanced by the power value applied to each metal target and the target gas ratio. The coated samples numbered by Si element composition which was determined by the power applied to the Si target. The applied voltage on Si targets as well as the nitrogen flow rate were monitored by OEM. These two parameters controlled the balance of $TiSi_xN$ elements. The $TiSi_{0.08}N$ coating showed the highest Ti content, and $TiSi_{0.13}N$ showed the most top N content. The former cause of Ti decreasing was the increased Si power lead to the higher deposition rate of Si, while the power applied on the Ti target remained constant. Also, as the N_2/Ar ratio increased from 50:50 to 60:40, shown in Table 2-2, the N content increased associated with Ti decrease. By adjusting the applied power ratio and gas ratio, the chemical concentration of $TiSi_xN$ could be changed and modified in order to achieve certain element concentration and desired phases.

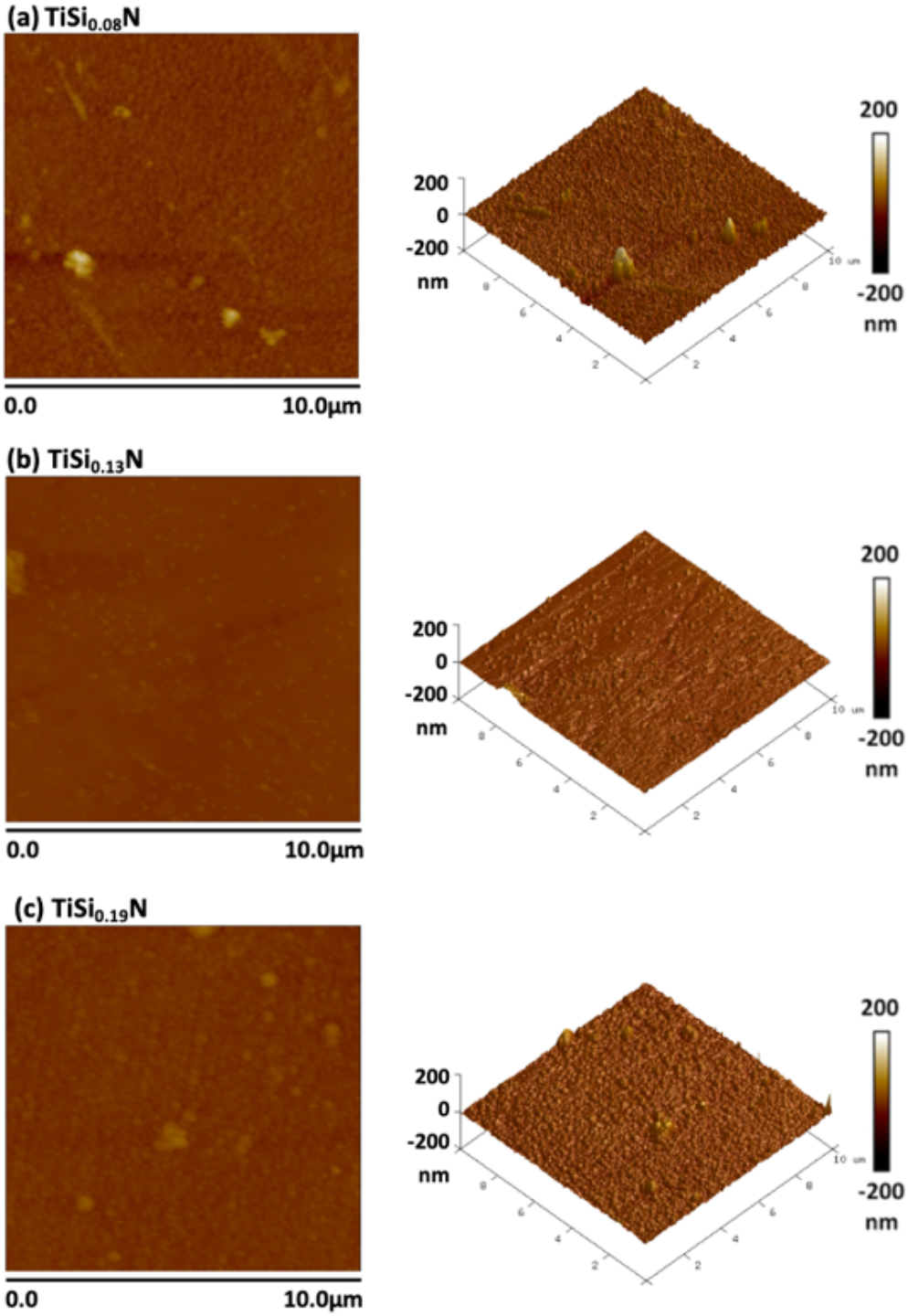

Figure 3-6 AFM height images (left) and 3D topography images (right) of as-deposited (a) $TiSi_{0.08}N$, (b) $TiSi_{0.13}N$ and (c) $TiSi_{0.19}N$ coatings with scan area 10µm by 10µm.

Since both surface roughness and grain size could affect corrosion behaviour of the nitride coatings. And the grain size of all three $TiSi_xN$ are less than 10 nm, which was difficult to determine by SEM and XRD analysis. Therefore, AFM was used not only to measure surface roughness, but also grain size features. The typical AFM photographs and 3D topographies of as-deposited $TiSi_xN$/Ti coating surface were displayed in Figure 3-6, respectively. The AFM height image of $TiSi_{0.13}N$ showed the smoothest morphology

compared to that of the other two surfaces, with the range of -15nm to 45nm. While, the surface height of $TiSi_{0.08}N$ was in the range of -41nm to 132nm, and $TiSi_{0.19}N$ was from -19nm to 104nm, as shown in the computer depth profile Figure 3-6. The surface roughness calculated from AFM analysis was listed in Table 3-1, from 10μm by 10μm scan area and restricted areas (exclude large surface droplet). The surface roughness showed good agreement with the SEM observation. $TiSi_{0.13}N$ coating showed the lowest surface roughness and the negligible difference between large scan area and restricted area due to the absence of surface droplets. $TiSi_{0.08}N$ coating showed the largest surface roughness from both 10μmx10μm scan area and limited scan area and considerable difference in these two results, which were due to a larger surface particle size and a larger size of the surface droplets, respectively. The roughness difference between large scan area and limited area of $TiSi_{0.08}N$ was more extensive than that of $TiSi_{0.19}N$, which indicated the surface nano-particle and droplet size of $TiSi_{0.08}N$ are larger than those of $TiSi_{0.19}N$. That is to say; the surface droplet size was consistent with surface particle size. The AFM helped us have a better understanding of the surface topography by qualitatively morphological analysis beyond SEM analysis.

Based on the contrast of cross-section SEM images shown in Figure 3-7, a double-layered structure coating presented with a thin Ti-interlayer (lighter grey) between the $TiSi_xN$ coating (dark grey) and Zy-4 substrate (white). Further, by using EDS mapping, Figure 3-7 (a_2), Ti-interlayer was confirmed with the thickness around 100nm. The Ti-interlayer was achieved by single target magnetron sputtering in pure Ar atmosphere for 10 minutes before switching on Si target for $TiSi_xN$ deposition. All three coatings showed a dense structure with no cracks and delamination between the substrate and coating layer, which manifested an excellent adhesion due to the Ti interlayer, excellent substrate surface finish and good deposition quality. Cross-section SEM graphs given in Figure 3-7 with scale bars indicated that the coatings were of the order of 1.5μm to 2μm in thickness after 1.5-hour magnetron sputtering deposition.

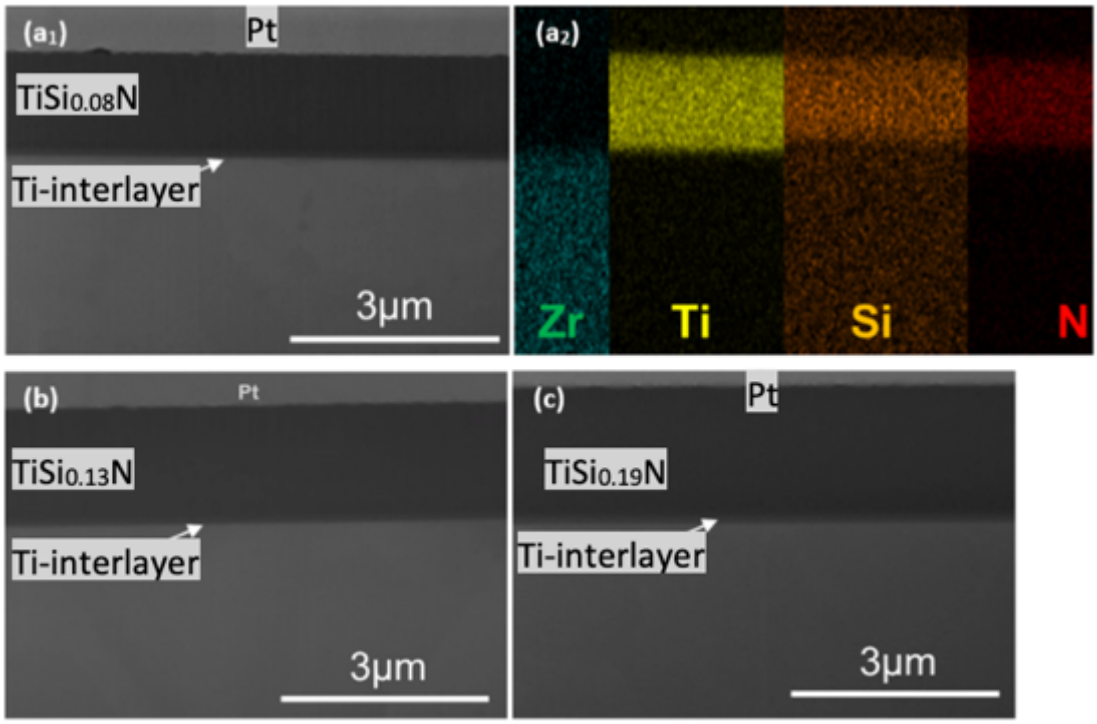

Figure 3-7 SEM images of as-deposited cross-section (a_1)$TiSi_{0.08}N$, (b) $TiSi_{013}N$ and (c) $TiSi_{0.19}N$ coatings with Ti-interlayer on Zy-4 alloy substrate and (a_2)EDS mapping of $TiSi_{0.08}N$.

Table 3-1 listed the thickness of the as-deposited double-layer $TiSi_xN$/Ti coatings measured from multiple cross-section SEM images. After the same deposition time, the thickness difference was due to the increased power on Si target with consistent power on the Ti target. That is, the deposition power governs the deposition rate of each target. The SEM images of $TiSi_xN$/Ti coating cross-sections cut by FIB demonstrate the compact $TiSi_xN$/Ti coatings, while fine columnar structure showed in literature papers did not appear in this magnetron sputtered $TiSi_xN$/Ti coatings. No clear crystal grains or columnar structure were observed in the cross-section SEM images, which may lead to the conjecture that the $TiSi_xN$/Ti coatings were amorphous, agreed with previous XRD results. Fine columnar grain structure converted to amorphous could cause by the Si-implantation or pulsed DC magnetron sputtering[159], [160]. The amorphous coating has been proved to increase hardness[159] and minimise the penetrate corrosion behaviour of columnar TiN structure[153].

According to both the analyses of SEM and XRD, $TiSi_xN$/Ti coatings deposited by magnetron sputtering in this study were nano-crystalline TiN or amorphous with Si component due to the Si-addition and magnetron sputtering.

3.2. High-temperature steam oxidation

Understanding steam oxidation behaviour of nitride coatings is must frontier precede to evaluate the feasibility of nitride ceramics as a protective coating system for the ATF Zy-4 fuel claddings under LOCA condition. To this end, steam tests were designed to investigate the protective potential of ZrN and $TiSi_xN$/Ti coatings and its corrosion behaviour under high-temperature steam environment (600°C, 800°C and 1000°C). A temperature of 600°C was selected to determine if the coating material reacts with low-temperature steam, while higher temperature steam tests (800°C and 1000°C) were conducted to simulate a possible LOCA scenario in LWR.

The oxidation behaviour of nitride coatings on Zy-4 substrate under high-temperature steam was explored by means of GIXRD, SEM and EDS in order to characterise the phase change, surface and cross-sectional morphology, composition variation, respectively. All the analysis was divided into two parts, the comparison between Zr and $TiSi_xN$, and the comparison of Si addition content among three $TiSi_{(0.08,\ 0.13,\ 0.19)}N$/Ti coatings. The GIXRD results of zirconium and its oxides were used to analyse the corrosion extent of Zy-4 substrate in order to evaluate the steam and corrosion resistance of $TiSi_xN$/Ti coating system. The results of titanium oxides were used to discuss the effect of Si addition content on corrosion resistance against high-temperature steam.

According to the results, single layer of ZrN could not survive for 1 hour under 600°C steam test, while $TiSi_xN$/Ti double-layer coating system could withstand steam erosion up to 1000°C for 4 hours. This chapter mainly discussed the details of ZrN and $TiSi_xN$ coatings oxidation behaviour under the steam environment.

3.2.1. Macro-surface analysis and compositional analysis

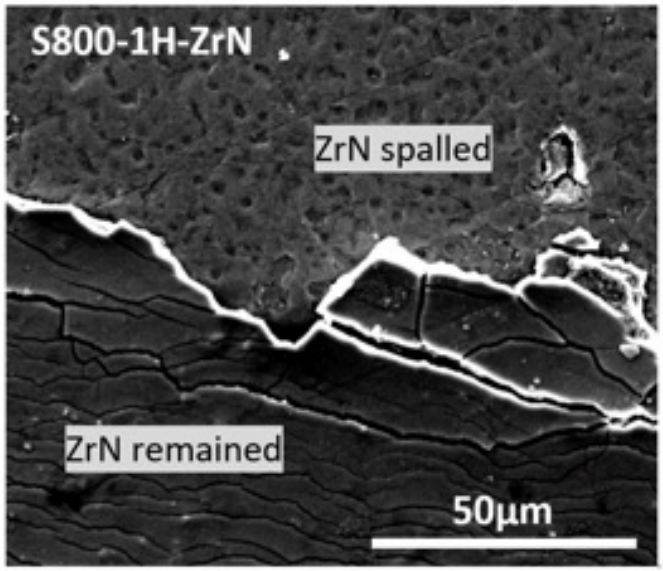

Figure 3-8 Macro-surface morphology of ZrN after 1-hour steam test at 800°C

Figure 3-8 showed the macro observation of the 1 hour 800°C steam eroded ZrN coating surface. Massive crevices generated on all steam tested samples during the steam test and cooling process. And similar morphology also presented at 1 hour 600°C steam treated ZrN sample, which was not shown here. Severe spallation and crimping occurred at the ZrN surface after the 1-hour steam test at 600°C and 800°C which indicated that single layer ZrN coating could not withstand the thermal mismatch during heating and cooling process.

Figure 3-9(a)-(j) showed the surface morphology of $TiSi_{(0.08,\ 0.13,\ 0.19)}N$/Ti double-layer coated samples after 4 hours steam tests at the temperature of 600°C, 800°C and 1000°C. After 4 hours steam test, all coatings were still attached onto the Zy-4 surface with no large area spallation, but cracks existed after stem test. Cracks formed on $TiSi_{0.08}N$ coatings after all 600°C, 800°C and 1000°C steam tests. While cracks only formed on $TiSi_{0.13}N$ and $TiSi_{0.19}N$ coatings after 800°C and 1000°C tests. The formation of massive cracks on all three coatings attributed to the thermal mismatch between themselves and substrate due to the rapid cooling process. Crack morphology on each coating were different, $TiSi_{0.08}N$ showed a consistent straight and paralleled feature for all temperature range, while $TiSi_{0.13}N$ and $TiSi_{0.19}N$ showed more curly cracks and buckling at the edges when the steam temperature reached over 800°C. The cracks

observed from the coatings may cause the loss of protection of the underneath Zy-4 substrate, but the adhesion of double-layer structure has improved dramatically compared to ZrN single layer structure. Further investigation on corrosion resistance of $TiSi_xN$/Ti double layered coatings were illustrated in the following sections.

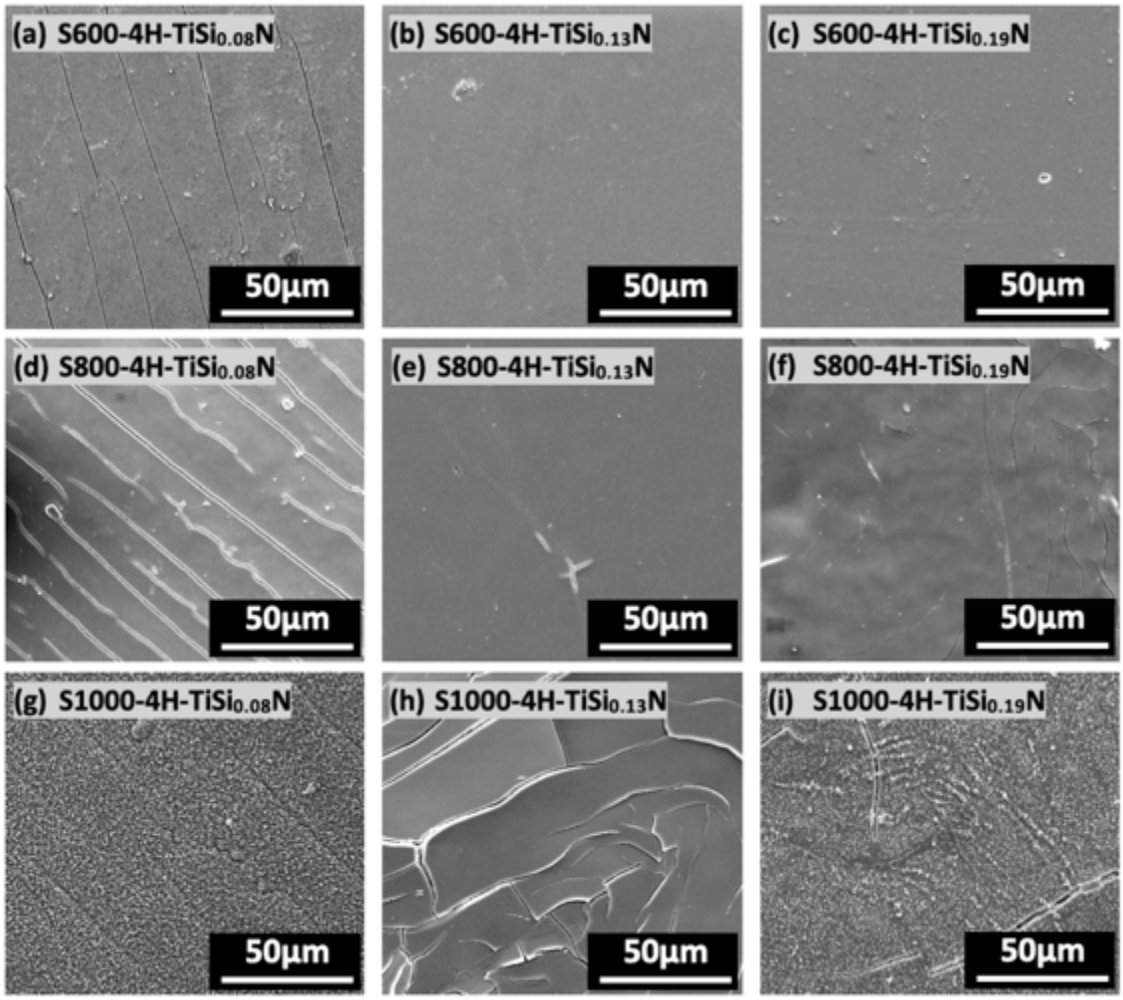

Figure 3-9 4 hours of steam tested surface morphology SEM images of (a) $TiSi_{0.08}N$, (b) $TiSi_{0.13}N$, (c) $TiSi_{0.19}N$ at 600°C, (d) $TiSi_{0.08}N$, (e) $TiSi_{0.13}N$, (f) $TiSi_{0.19}N$ at 800°C and (g) $TiSi_{0.08}N$, (h) $TiSi_{0.13}N$, (i) $TiSi_{0.19}N$ at 1000°C

3.2.2. 600°C steam oxidation characterisation

3.2.2.1. Phase identification

Figure 3-10 showed the GIXRD results with incident angle 2° of phase formation of ZrN, $TiSi_{(0.08,\ 0.13,\ 0.19)}N$/Ti double-layer coated Zy-4 samples and bare Zy-4 substrate after 600°C steam tests as time increases. XRD pattern curve of single-side-polished Zy-4 plate after 1h 600°C steam test was used as a reference to distinguish the overlap of coating phases (TiN, TiO_2, ZrO_2) with Zr peaks. After 1 hour 600°C steam test, the main

phase detected from the bare Zy-4 was zirconium. The highest two peaks at 34.8° and 36.5° match with Zr (002) and (101), which was consistent with the as-received samples. Serval low-intensity peaks of monoclinic ZrO_2 (M-ZrO_2, ICDD: 04-004-4339) at 28.2° and 34.1° presented in GIXRD pattern of Zy-4 substrate after 1 hour 600°C steam test. According to the X-ray penetration depth and the ratio between Zr and ZrO_2 peaks, ZrO_2 layer formed at 600°C was relatively thin.

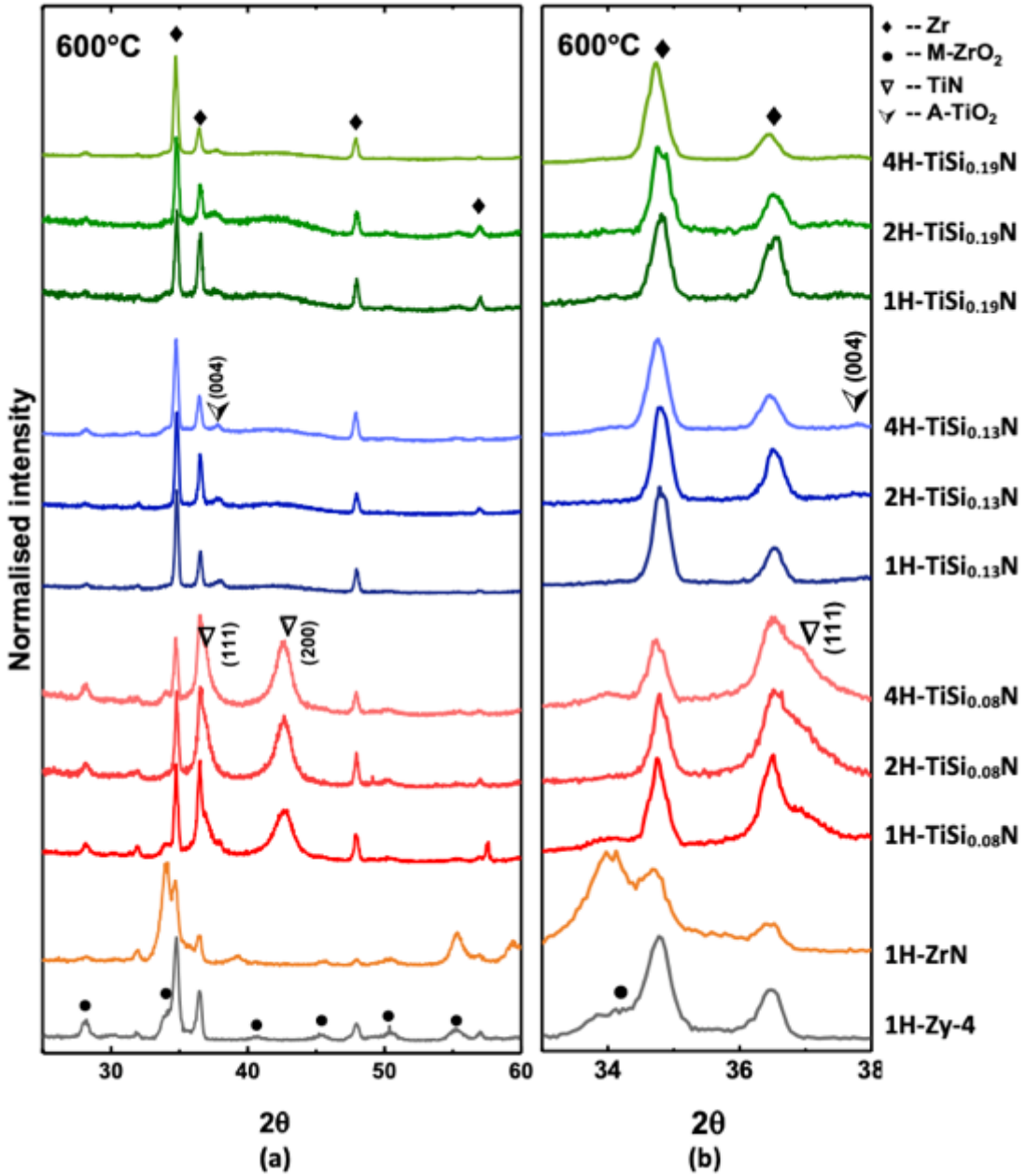

Figure 3-10 GIXRD patterns with X-ray incident angle 2° (a) from 25° to 60° and (b) from 32° to 38° of single-side-polished bare Zy-4 bulk (grey curve) and ZrN coating on zirconium alloy substrate (orange curve) after 1h 600°C steam test, and $TiSi_{0.08}N$ (red curves), $TiSi_{0.13}N$ (blue curves) and $TiSi_{0.19}N$ (green curves) coatings with Zy-4 substrate after 1h, 2h and 4h steam test at 600°C(M-ZrO_2=Monoclinic Zirconium Oxide; A-TiO_2=Anatase;)

For ZrN coating, after 1-hour steam test at 600°C, the main phase was M-ZrO_2 with the highest intensity at 34.1° associated with diffraction plane (002). While, the secondary phase was Zr identified by peaks at 34.8° and 36.5°. No ZrN pattern presented in the steam tested ZrN sample compared with as-deposited one. It could speculate that ZrN coating fully oxidised or completely lost due to spallation after 1-hour steam test at 600°C. Details of coating oxidation needed to be verified by SEM analysis.

For all three $TiSi_xN$/Ti coatings after steam oxidation at 600°C, the broadened peak of TiN with diffraction plane (200) at the range from 40° to 44° was comparably visible as compared to the as-deposited GIXRD results, given in Figure 3-2. The intensity of TiN (200) peaks from $TiSi_{0.08}N$ after 1 and 2 hours steam tests at 600°C were much stronger, and the width of that became narrower compared to as-deposited $TiSi_{0.08}N$/Ti coated sample. From the Fig.3-10(b) magnified XRD pattern, a clear shoulder of the peak at 36.9° determined as TiN (111) from $TiSi_{0.08}N$ after all 600°C steam tests fitted the as-deposited state. A much clear bump at TiN (200) presented in $TiSi_{0.13}N$ and $TiSi_{0.19}N$ after 600°C steam tests. It was explained as the high temperature steam treatment could anneal out the interstitial atoms at 600°C[158]. No clear sign of TiN (111) peaks detected from $TiSi_{0.13}N$ and $TiSi_{0.19}N$ after 600°C steam tests since the Zr peak at 36.5° was sharp and narrow. It suggested that recrystallisation of amorphous TiN phases occured in $TiSi_{0.08}N$ with lowest Si addition under the high-temperature steam environment.

The main oxidation product of $TiSi_{0.13}N$ and $TiSi_{0.19}N$ coatings after 1 and 2 hours 600°C steam tests was identified as tetragonal anatase, titanium dioxide (A-TiO_2, ICDD: 04-014-8515). The TiO_2 peak at 37.8° with diffraction plane (004) showed very low intensity in $TiSi_{0.13}N$, and $TiSi_{0.19}N$ samples after 600°C steam test, but no signal of that could be identified in $TiSi_{0.08}N$. From the magnified curves given in Figure 3-10(b), the peaks of TiO_2 (004) became broader as the Si content increases, from $TiSi_{0.13}N$ to $TiSi_{0.19}N$, which indicated that the TiO_2 particles of formed on $TiSi_{0.13}N$ were finer than that of $TiSi_{0.19}N$. According to the reference, A-TiO_2 supposed to have a diffraction plane

(200) at 48.014°. However, it was hard to distinguish that from Zr (102) peak at 47.94°. To the end, from the GIXRD results, it could tell that only $TiSi_{0.08}N$ slightly oxidised while marginal oxidation occurred in $TiSi_{0.13}N$ and $TiSi_{0.19}N$ after 4 hours steam test at 600°C.

3.2.2.2. Surface and cross-section analysis of ZrN

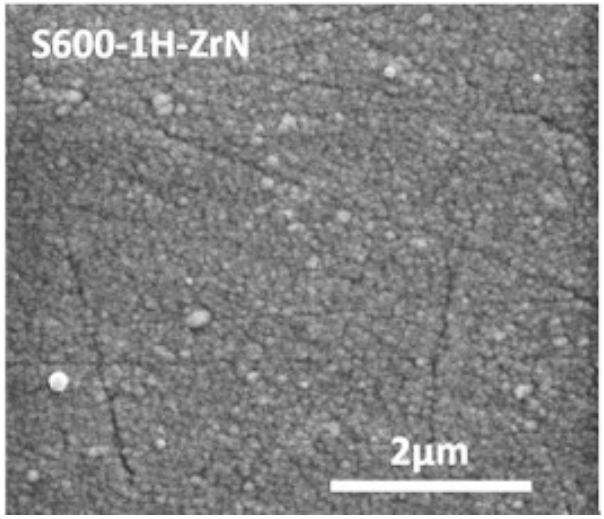

Figure 3-11 Surface SEM SE images of remain attached ZrN coating after 1 hour 600°C steam test

According to the macro-surface investigation, picture not shown, severe spallation happened to the ZrN coated samples after 1 hour 600°C steam test, only a few areas near the edges still attached with ZrN shads. It was supposed to be the thermal mismatch between ZrN and Zr-Nb substrate during heating and cooling. Majority of the substrate surface exposed to the steam environment, which led to severe oxidation. Figure 3-11 presented the surface morphology of the remained coating shards. Nano-sized round particles were the oxidation product from ZrN and fully covered the coating surface after 1 hour 600°C steam test.

Figure 3-12 and Figure 3-13 showed further observation from cross-section BSE images and detailed EDS mappings. According to the strong signal of oxygen in EDS mapping, severe oxidation occurred at the ZrN coating and the substrate surface where both ZrN coating spalled off and attached. The relatively thicker oxide layer formed at the area where ZrN coating spalled compared to ZrN attached surface. A thick layer of oxide with lateral micro-cracks inside displayed on the surface of the Zr substrate, and

a grey layer between the upper oxide layer and un-corroded Zr substrate which could be identified as the oxygen-stabilised α phase[161].

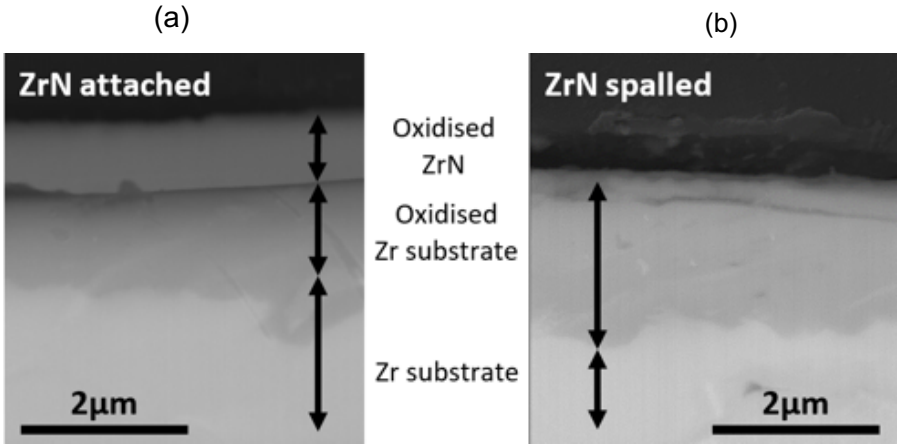

Figure 3-12 Cross-section SEM BSE images of ZrN samples after 1 hour 600°C steam test (a) with ZrN coating attached (b) ZrN coating spalled area

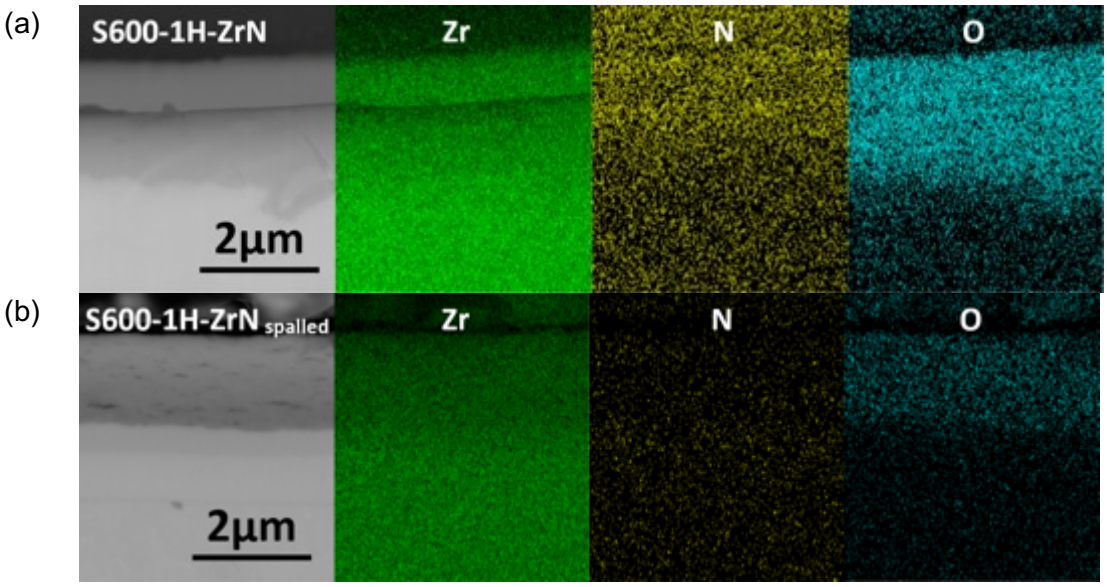

Figure 3-13 Cross-section SEM images and EDS elemental mapping of (a) ZrN coating on Zr substrate (b) ZrN coating spalled area after 1-hour steam test at 600°C

3.2.2.3. Surface and cross-section analysis of $TiSi_xN/Ti$

Cross-section investigation conducted on all steam tested samples at 600°C, including single-side polished Zy-4 substrate, and $TiSi_xN/Ti$ coated Zy-4. Comparison between Si content and oxidation time were presented in this chapter.

Figure 3-14(a)~(i) gave higher magnification SEM images of $TiSi_xN/Ti$ coatings after 1h, 2h and 4h steam tests at 600°C. The surface of $TiSi_xN$ coatings after various steam oxidation periods showed barely difference in morphology. Compared to the as-

deposited coating surface, the particle boundary seemed sharper and more evident after steam treatment. Coatings after 600°C steam tests showed a slight difference in surface particle size different according to Si content, which was similar to those of as-deposited surface particles. As the steam test period increases at 600°C, the surface particle remained constant without significant grain growth for all three coatings with different Si content. It indicated that steam test under 600°C could not cause severe degradation or corrosion to $TiSi_xN$/Ti coating.

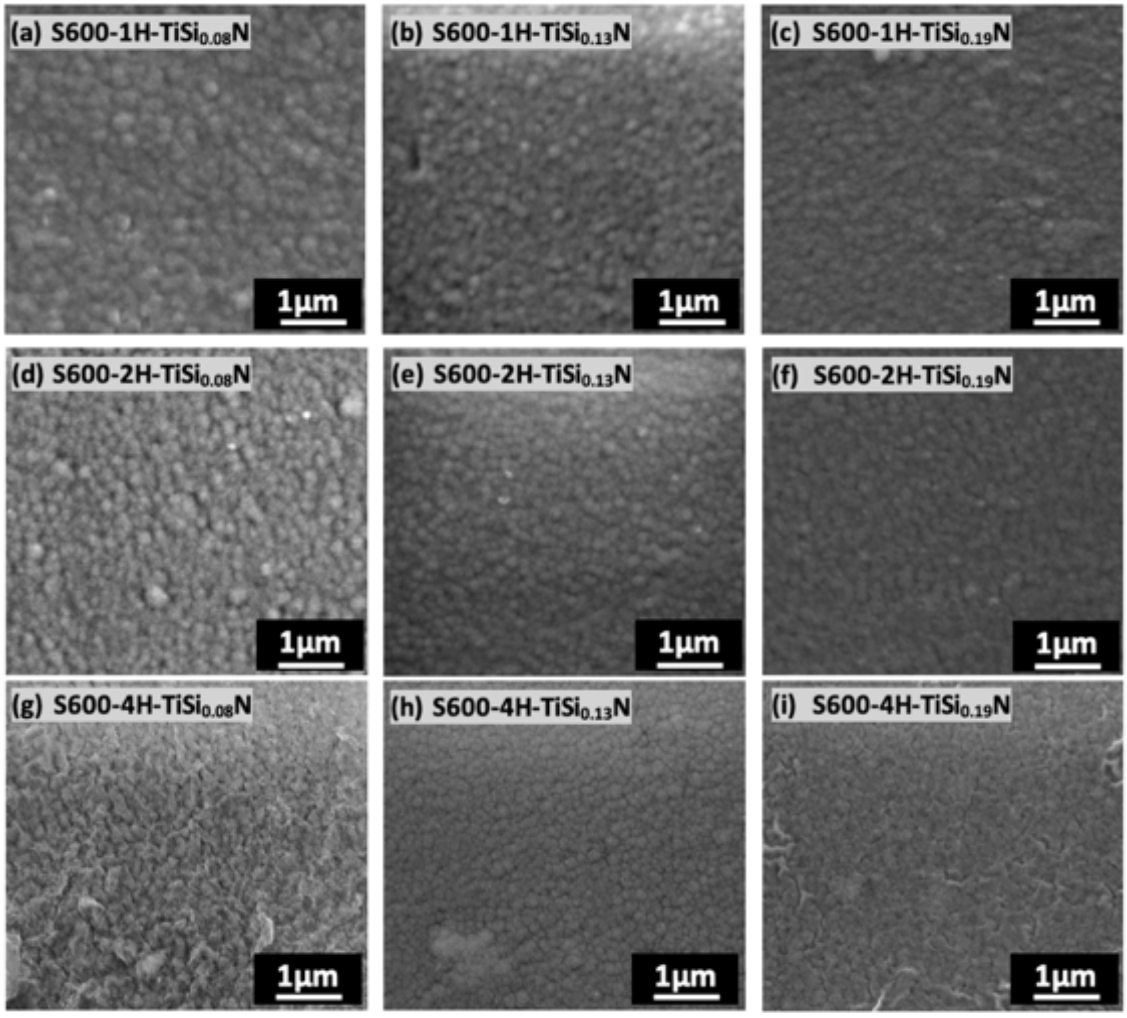

Figure 3-14 High magnification images (50000x) of $TiSi_{0.08}N$, $TiSi_{0.13}N$ and $TiSi_{0.19}N$ coating surface morphology after 1h, 2h, and 4h steam tests at 600°C

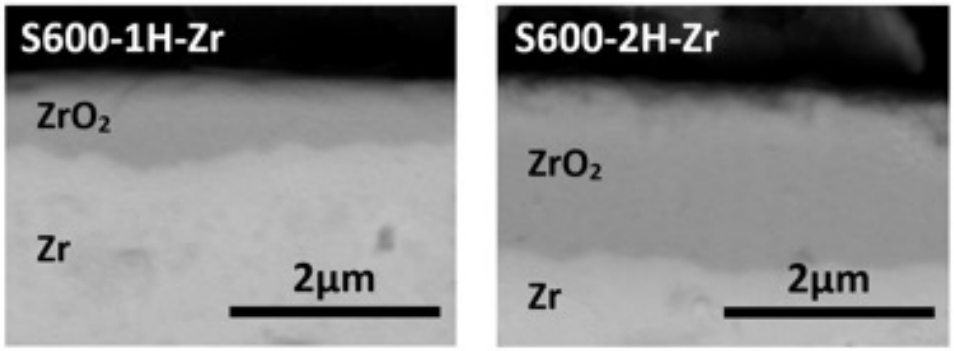

Figure 3-15 Cross-section SEM images of polished Zy-4 substrate after 600°C steam test

In order to proof the steam resistance of coating systems, the bare substrate was steam tested at 600°C for 1h and 2h. The cross-section of corroded substrate was shown in cross-section images (Figure 3-15). Clear oxide layer formed on the surface of Zy-4 substrate. The thickness of the oxide layer was around 0.75 and 2μm for 1 hour and 2-hour tests, respectively, which agreed with the low-intensity peaks of ZrO_2.

Figure 3-16(a)-(i) presented $TiSi_xN$/Ti coatings and substrate steam oxidation condition in backscattering electron (BSE) mode with different contrast. No sign of oxidation occurred to the substrate of $TiSi_xN$/Ti coated samples under 600°C steam up to 4 hours. It was also consistent with the X-ray diffraction results that no strong peaks of ZrO_2 were detected. It indicated that 600°C steam could not penetrate and degradant $TiSi_xN$/Ti coating system, and $TiSi_xN$/Ti coating system could protect Zy-4 substrate for at least 4 hours from 600°C steam. However, even with several cracks observed from the surface of $TiSi_xN$/Ti coatings shown in section 3.2.1 (Page 75). It could speculate that cracking occurred during cooling.

According to the cross-section microstructure analysis, $TiSi_xN$/Ti coatings after 600°C steam test showed barely any changes after sequence time steam corrosion. The coatings all remained flat, uniform and well-attached to the substrate. The Ti-interlayer remained clear for all samples from the BSE SEM images. No evidence of corrosion and oxidation occurred at the surface of the coating as well as the underneath Zy-4 substrate. This result was consistent with the surface elemental analysis, which remained a similar percentage of each element with as-deposited $TiSi_xN$/Ti coatings.

The oxygen detected from the surface could be absorbed into the coating surface but not forming oxides.

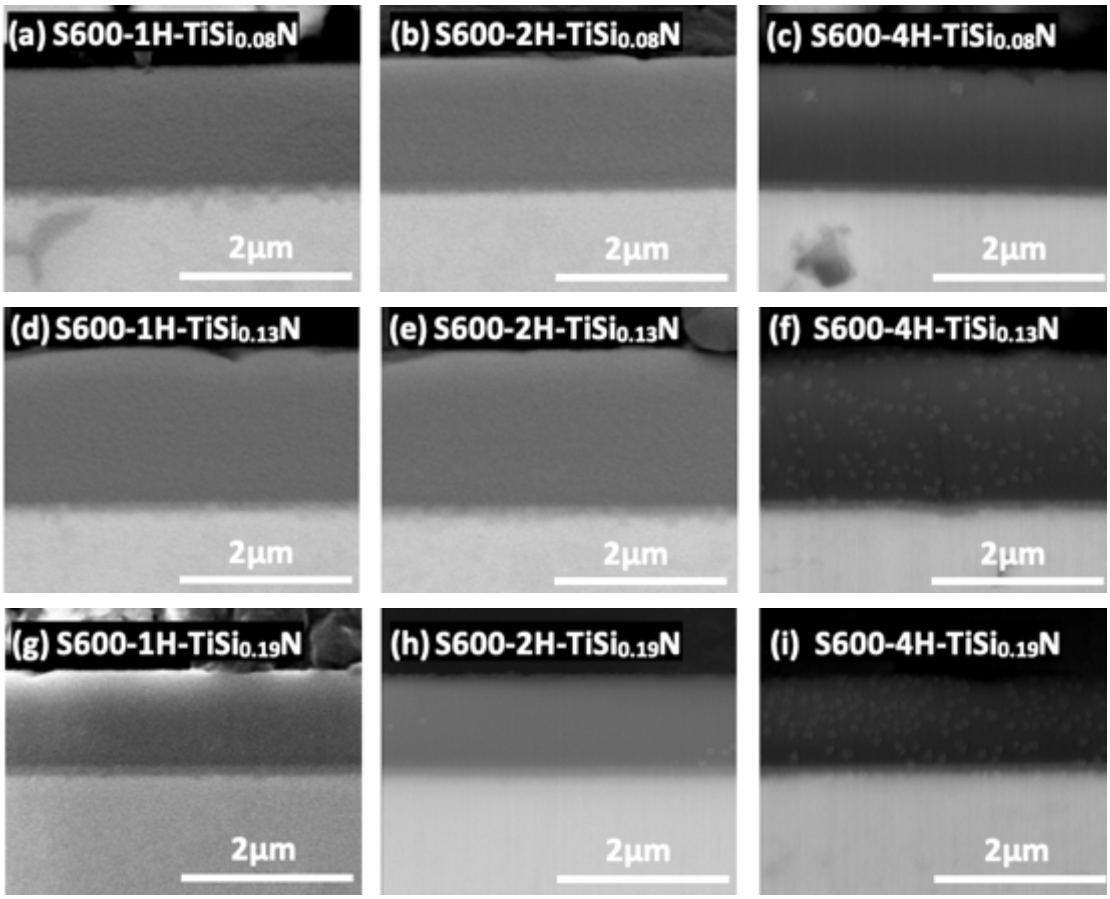

Figure 3-16 Cross-section SEM images in BSE mode of $TiSi_{0.08}N$/Ti after (a)1 hour, (b) 2 hours and (c) 4 hours, $TiSi_{0.13}N$/Ti after (d)1 hour, (e) 2 hours and (f) 4 hours and $TiSi_{0.19}N$/Ti after (g) 1 hour, (h) 2 hours and (i) 4 hours steam test at 600°C

3.2.3. 800°C steam oxidation characterisation

3.2.3.1. Phase identification

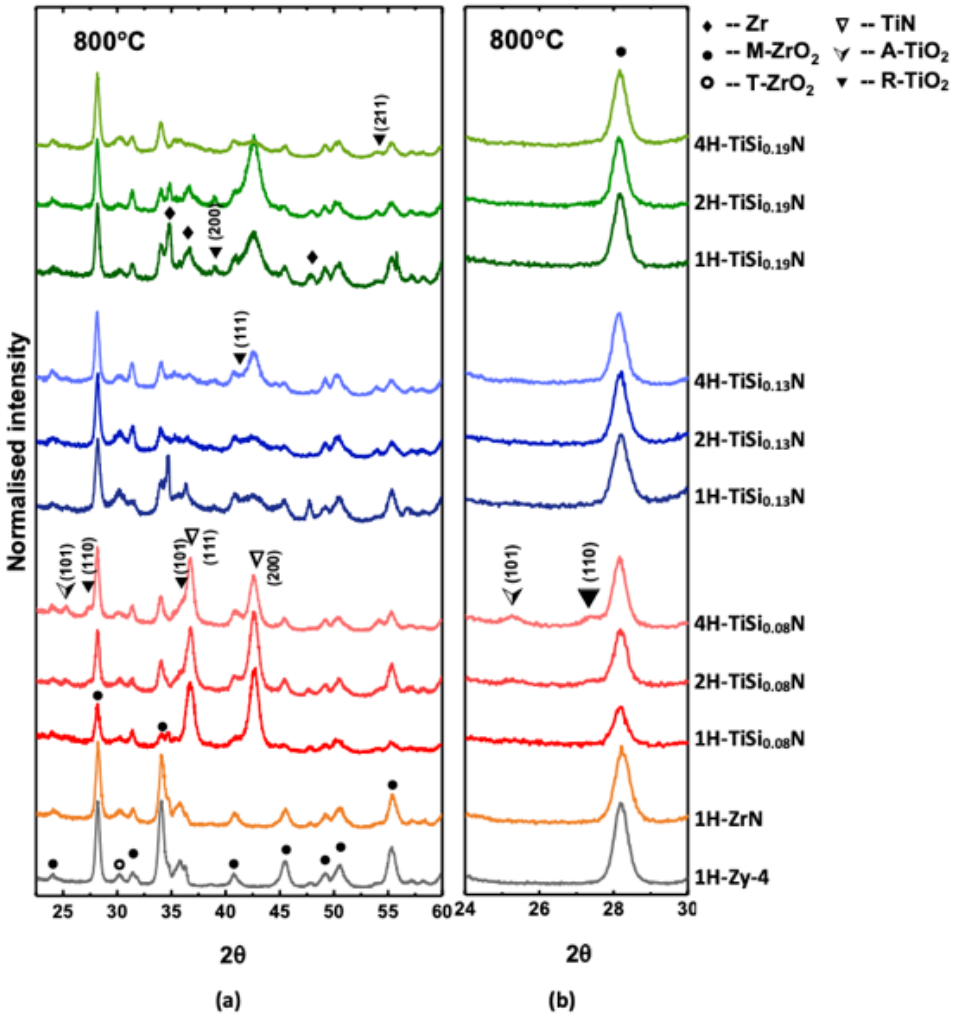

Figure 3-17 GIXRD patterns with incident angle 2° of single-side-polished bare Zy-4 bulk and ZrN coating on zirconium alloy substrate after 1h 800°C steam test, and $TiSi_xN$/Ti coatings with Zy-4 substrate after 1h, 2h and 4h 800°C steam test. (M-ZrO_2=Monoclinic Zirconium Oxide; T-ZrO_2=Tetragonal Zirconium Oxide; A-TiO_2=Anatase; R-TiO_2=Rutile)

Figure 3-17 illustrated GIXRD (incident angle 2°) results of the steam tested $TiSi_{(0.08, 0.13, 0.19)}N$ samples and Zy-4 bare substrate after 1, 2 and 4 hours at 800°C. The dominant peaks of Zy-4 substrate presented after 1 hour 800°C steam test is monoclinic ZrO_2 (M-ZrO_2). The diffraction planes of M-ZrO_2 are (-111) and (002) matched with the two highest intensity peaks at 28.2° and 34.1°. Another zirconia phase that recognised at 30.2° in 800°C steam tested samples is tetragonal ZrO_2 (T-ZrO_2, ICDD: 04-005-4504), which was new compared to Zy-4 sample after 1 hour 600°C steam test. The detection of two oxide phases indicated that severe oxidation occurred at Zy-4 surface due to the 1-hour steam attack at 800°C. As the XRD results collected at room temperature,

tetragonal phase, a high-temperature phase, was kept due to the T-M transformation induced compression stress and fast cooling[162]. The main phase of the bare Zy-4 surface after 1 hour 800°C steam test was monoclinic zirconia while that at 600°C was zirconium. Low intensity peaks of Zr detected in 800°C steam test suggested that the oxide layer was relatively thin compared to the X-ray penetration depth but thicker compared with those tested at 600°C, which needed to verify with SEM cross-section observation. This indicated that the high-temperature steam starts to oxidise Zy-4 alloy when steam temperature exceeds 600°C. Zy-4 could loss the steam resistance at the temperature between 600°C and 800°C, while, the precise temperature where loss the steam resistant needs further investigation.

The GIXRD result of ZrN coating after 1 hour steam test at 800°C (Figure 3-17) showed a dramatic difference compared with that at 600°C(Figure 3-11) due to the remarkable ZrO_2 peak at 28.2°. The XRD pattern of ZrN coated sample after 1 hour 800°C steam test (orange line) was highly consistent to that of bare Zy-4 substrate after 1 hour 800°C steam test (grey line). It suggested that significant oxidation occurred to ZrN coating itself and protection of ZrN coating lost at 800°C, which was also consistent with the spallation observed from the macro-surface investigation.

GIXRD detected two relative sharp peaks of TiN (111) and (200) at 36.8° and 42.9° from $TiSi_{0.08}N$ after 800°C steam oxidation similar to that in the as-deposited states and after steam tested at 600°C. $TiSi_{0.13}N$ samples after 1and 2 hours 800°C steam oxidation showed a swell at the TiN (200) position after 1h and 2h, while it detected a clear peak after the 4h steam test. $TiSi_{0.19}N$ coatings after 1- and 2-hours steam tests at 800°C contained a clear broadened peak of TiN (200) at 42.9°, which was distinctively apart from the bump shape of TiN peaks in that of as-deposited state and steam tested at 600°C. And this peak disappeared in $TiSi_{0.19}N$ after 4h test at 800°C. It suggested that as the steam temperature rises to 800°C, the formation of TiN crystal apart from amorphous particles occurred or nano-sized grain started to grow. The TiN

crystallisation and nano-sized grain growth need further investigation to identify the influence of Si and temperature, which is not the focus of this thesis.

In order to demonstrate if oxidation occurred after 800°C steam test, titanium oxide was the main focus of this GIXRD results. By comparing with the GIXRD results of Zy-4 substrate after 1-hour steam oxidation at 800°C, $TiSi_{0.13}N$ and $TiSi_{0.19}N$ after 800°C steam treatment only detected few low-intensity peaks as TiO_2. It meant that there was no significant titanium oxide crystal formation on $TiSi_{0.13}N$ and $TiSi_{0.19}N$ during the 800°C steam test no matter the test period. However, several low-intensity peaks marked as TiO_2 in $TiSi_{0.08}N$ steam treated at 800°C. According to the 800°C steam tested $TiSi_{0.08}N$ XRD patterns, titanium oxide showed two different crystal structure, A-TiO_2 (anatase, ICDD: 04-014-8515) and R-TiO_2 (rutile, ICDD: 01-078-4188). The peak could confirm A-TiO_2 at 25.3° with a diffraction plane (101). From the magnified graph Figure 3-17(b), the clear shoulder peak attached to the left of M-ZrO_2 peak at 27.4° could identify as R-TiO_2 (110) in 4 hours steam tested $TiSi_{0.08}N$ at 800°C. Based on the investigation of XRD, no significant crystalline oxide formation of $TiSi_xN$/Ti coatings happened, but $TiSi_{0.08}N$ showed more TiO_2 to some extent. Zy-4 substrate covered by $TiSi_xN$/Ti coatings all showed oxidation to a certain degree. The oxidation degree of coatings and substrate need to be identified by SEM and elemental analysis, given in the following section.

3.2.3.2. Surface morphology and elemental analysis

From the high magnification images of TiSixN/Ti surfaces after 800°C steam treatment, the surface particles were relatively uniform with the size of a few dozens of nanometres. Coatings after the steam test at 800°C showed a slight variation in surface particle size different according to Si content, which was similar to those tested at 600°C. For 800°C steam tested samples, the boundary of nanoparticles was more distinct according to the sharper contrast of SEM images compared to 600°C steam tested and as-deposited TiSixN/Ti coatings. Accompanied with the XRD results, the TiSixN/Ti coatings remained

nanoparticles and transition from amorphous to nano-crystal phase occurred after 800°C steam test, but no significant crystalline oxide formed.

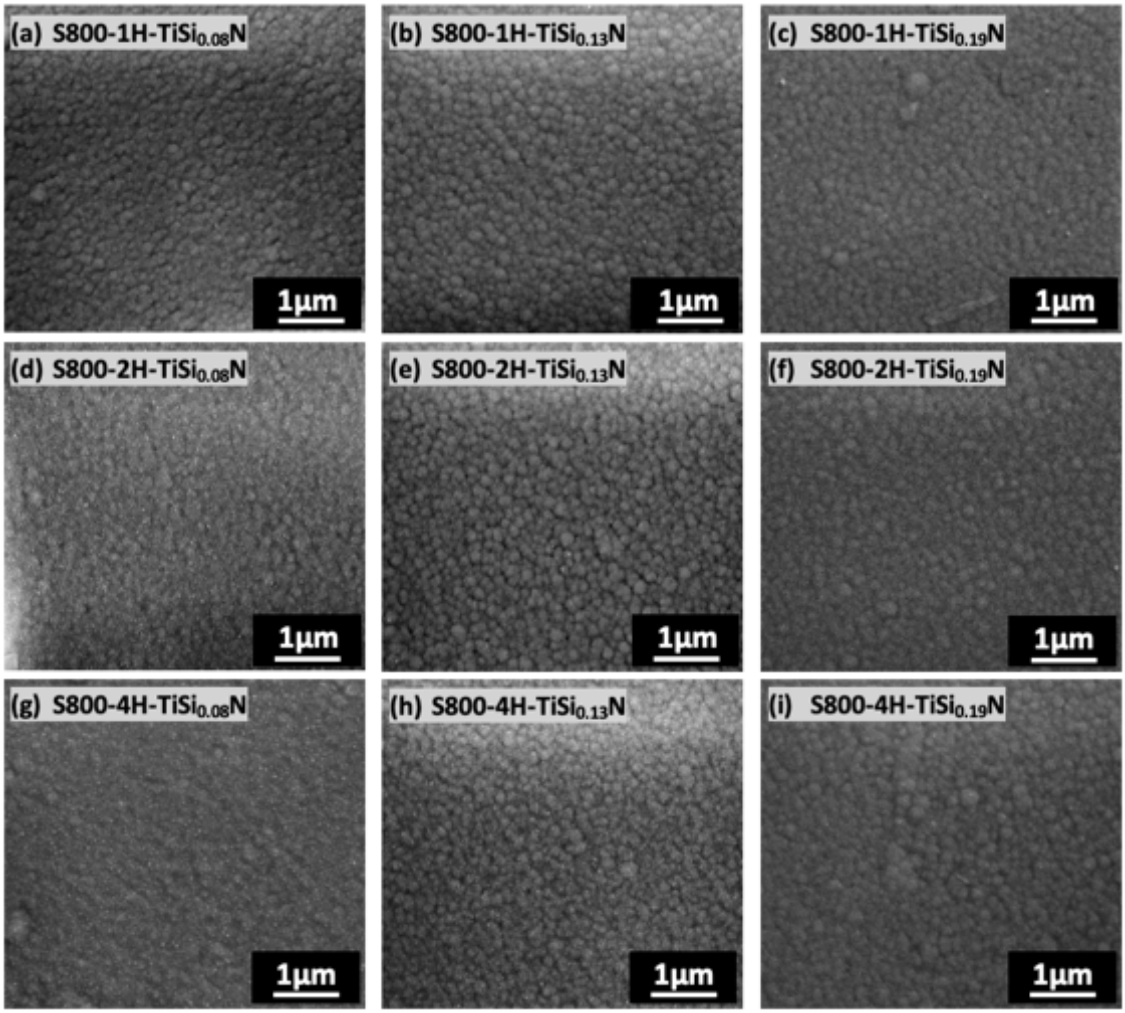

Figure 3-18 High magnification images (50000x) of $TiSi_{0.08}N$, $TiSi_{0.13}N$ and $TiSi_{0.19}N$ surface morphology after 1h, 2h, and 4h steam tests at 800°C

3.2.3.3. Cross-section and Oxidation kinetics

Based on the low magnification images of cross-section (Figure 3-19), ZrO_2 layer formed between $TiSi_{0.08}N$/Ti coating and Zy-4 substrate throughout the whole area. The thickness of ZrO_2 layers of each $TiSi_{0.08}N$ samples did not experience a dramatic increase after 1h, 2h and 4h steam tests at 800°C. As the test period increase, more quantity of the vertical cracks was found in the $TiSi_{0.08}N$ layer, and the interval between fractured $TiSi_{0.08}N$ pieces became wider, and the extent of $TiSi_{0.08}N$ coating curvature became more apparent. This phenomenon could be explained by the more porosity and cracks presented in the ZrO_2 layer. The broadening of gaps between fractured shards was due to volume expansion of porous oxide and cracks formation. Similar

phenomenon presented in $TiSi_{0.13}N$/Ti and $TiSi_{0.19}N$/Ti based on SEM observation (not shown). The curvature structure of ZrO_2 growth front was due to the oxygen-free path through the vertical cracks within $TiSi_xN$/Ti coating[77]. According to the thermal expansion, CTE of TiN is higher than Zr substrate, which leads to compression stress to $TiSi_xN$/Ti coatings during heating. Cracks were not supposed to form during the ramping and isothermal steam process. However, with rapid cooling, tensile stress was generated to $TiSi_xN$/Ti, which could cause a fracture of $TiSi_xN$/Ti coatings. The oxide layer formed in this study (4 -10μm) was much thinner compared to that on bare Zy-4 (10 -100μm), according to the comprehensive results from S. Leistikow and G. Schanz[163]. $TiSi_xN$/Ti coatings showed a significant corrosion resistance under 800°C and protected the Zy-4 substrate to some extent.

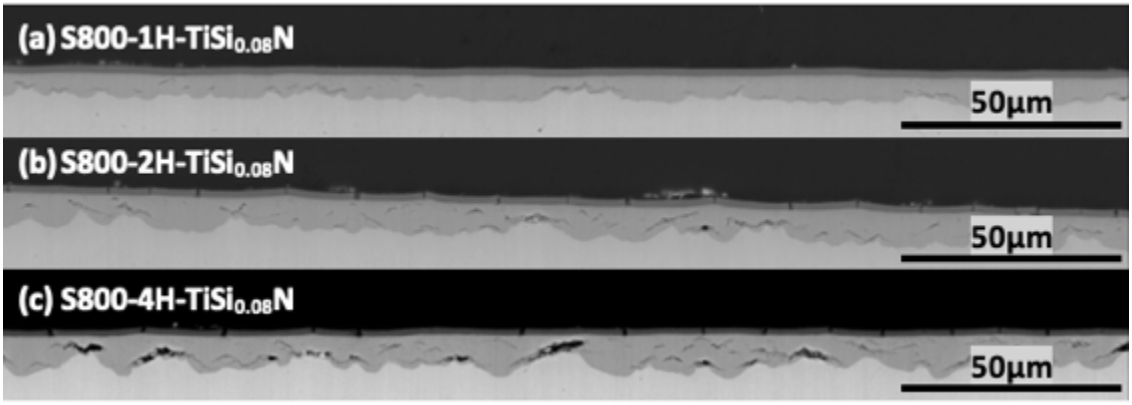

Figure 3-19 Macro-observation of $TiSi_{0.08}N$ samples after (a) 1 hour, (b) 2 hours and (c) 4 hours steam test at 800°C

According to Figure 3-20, curvature and cracks of the $TiSi_xN$/Ti coatings were observed from all samples after 1 hour 800°C steam tests, while most of the coatings remained attached to Zy-4 substrate and even oxidised area. Non-affected Zy-4 substrate remained below $TiSi_xN$ coatings after 1-hour test as shown in Figure 3-20(b)(c). A similar phenomenon was observed from all samples after 2 hours and 4 hours steam test at 800°C, with only slightly increased ZrO_2 layer thickness. Explicit evident showed $TiSi_{0.13}N$/Ti and $TiSi_{0.19}N$/Ti could provide sufficient protection against 800°C for 4 hours steam erosion. Compression stress were generated in TiSiN coatings due to the thermal expansion difference of substrate and ceramic coatings, see Table 1-5. In this case, cracks were not supposed to generate. But in fact, due to the hydro-effect,

corrosion occurred more robust. Hydrogen associated with vacancies accelerated the penetration of oxidation species. When the beneath Zr substrate started to oxidise, volume expansion could induce more complicated stress to coated system which led to the formation of vertical crack. Vertical cracks only presented within $TiSi_xN$/Ti coatings, and it propagated through the coatings and invaded into Zy-4 substrate, which created a pathway for water vapour to attack the beneath Zy-4 substrate. Lateral cracks followed the vertical cracks and propagated within the ZrO_2 layer along with the interface between the ZrO_2 layer and $TiSi_xN$/Ti coatings. The crack propagation led to deformation of $TiSi_xN$/Ti coatings but not spallation. The water vapour contacted the substrate at the front of vertical cracks. Apparent oxidation occurred firstly at the cracking region and then expanded to the nearby area. The oxidise species diffuse inwards used the contact points as a centre and were blocked by voids and porous, which led to non-uniform ZrO_2 layer.

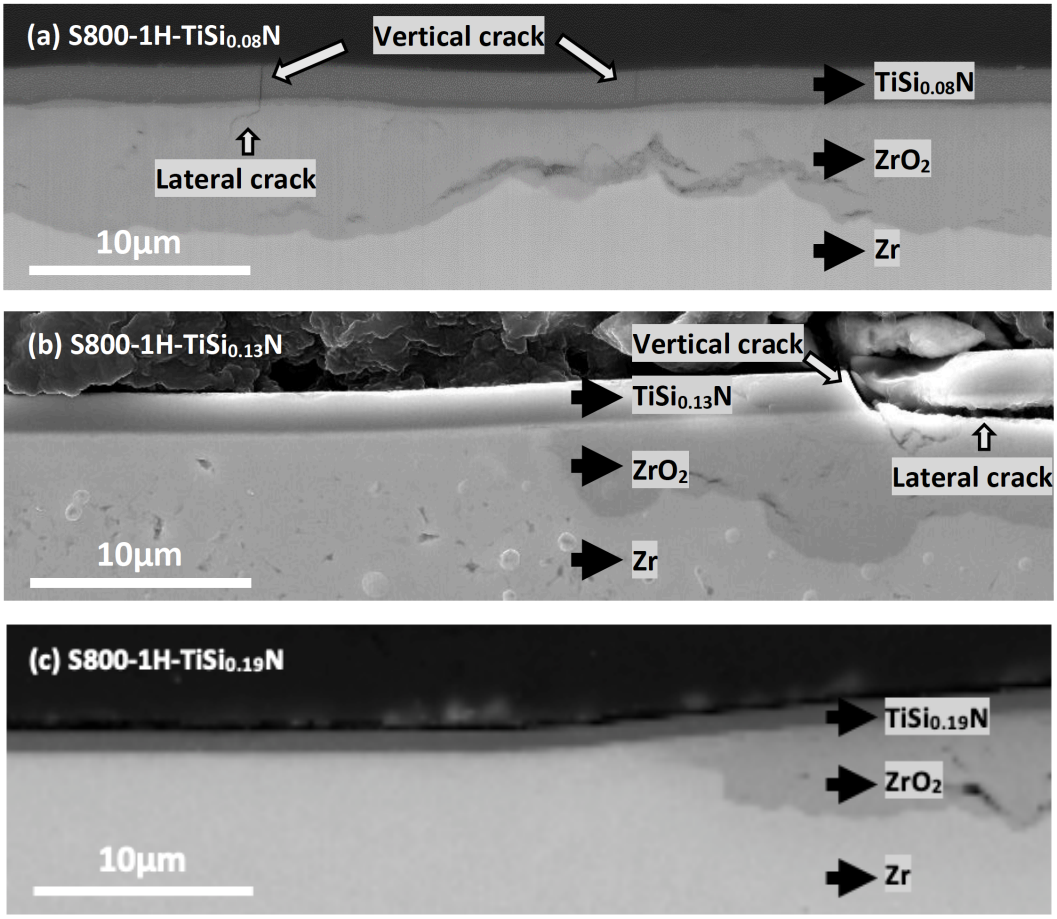

Figure 3-20 Lower magnification of cross-section SEM images of (a) $TiSi_{0.08}N$, (b) $TiSi_{0.13}N$ and (c) $TiSi_{0.19}N$ after 1 hour 800°C steam test, with vertical cracks within the coating and lateral cracks within ZrO2 layer along with the oxide and un-corroded Zr interface

(a) S800-1H-$TiSi_{0.08}N$

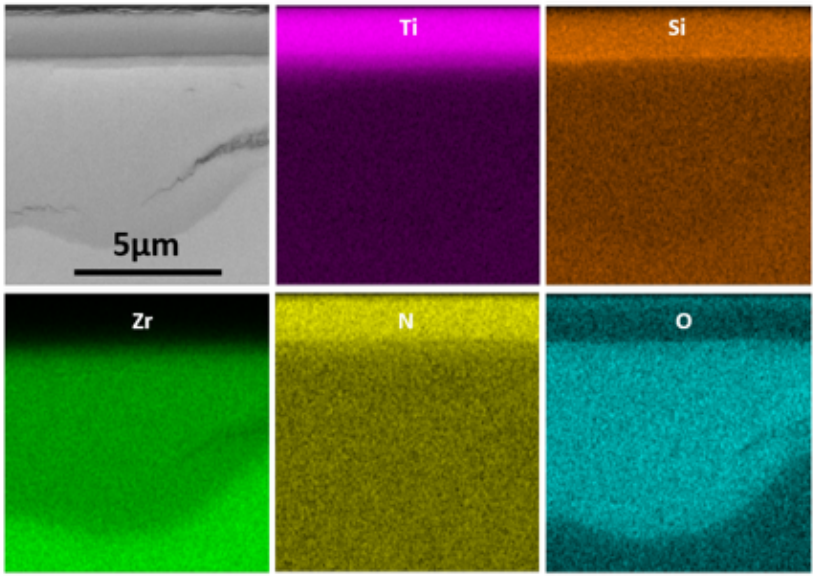

(b) S800-2H-$TiSi_{0.08}N$

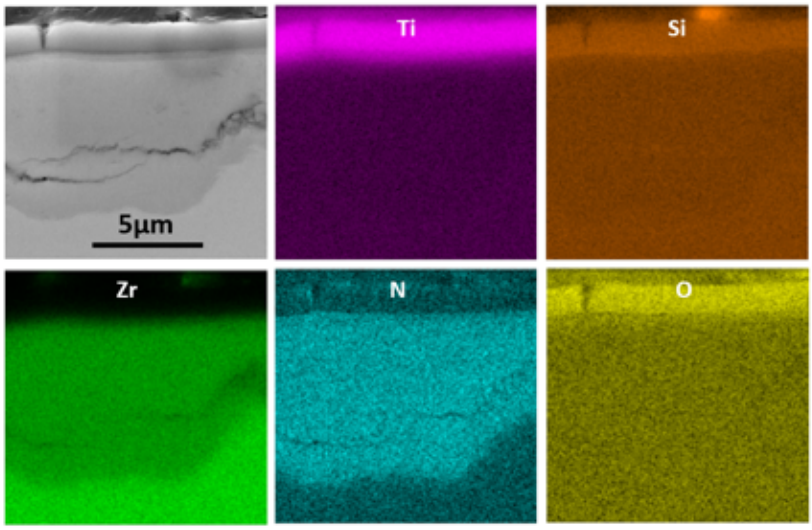

(c) S800-4H-$TiSi_{0.08}N$

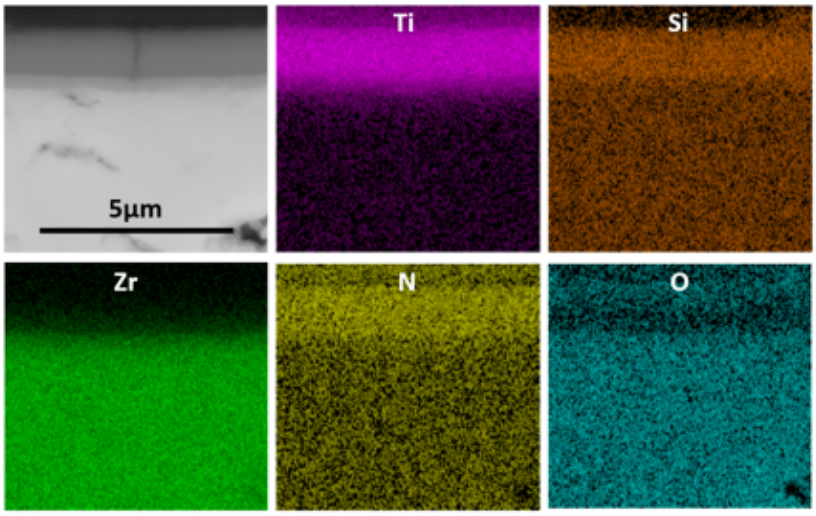

Figure 3-21 Cross-section SEM images in BSE mode and EDS mappings of $TiSi_{0.08}N$ after (a) 1 hour, (b) 2 hours and (c) 4 hours steam tests at 800°C

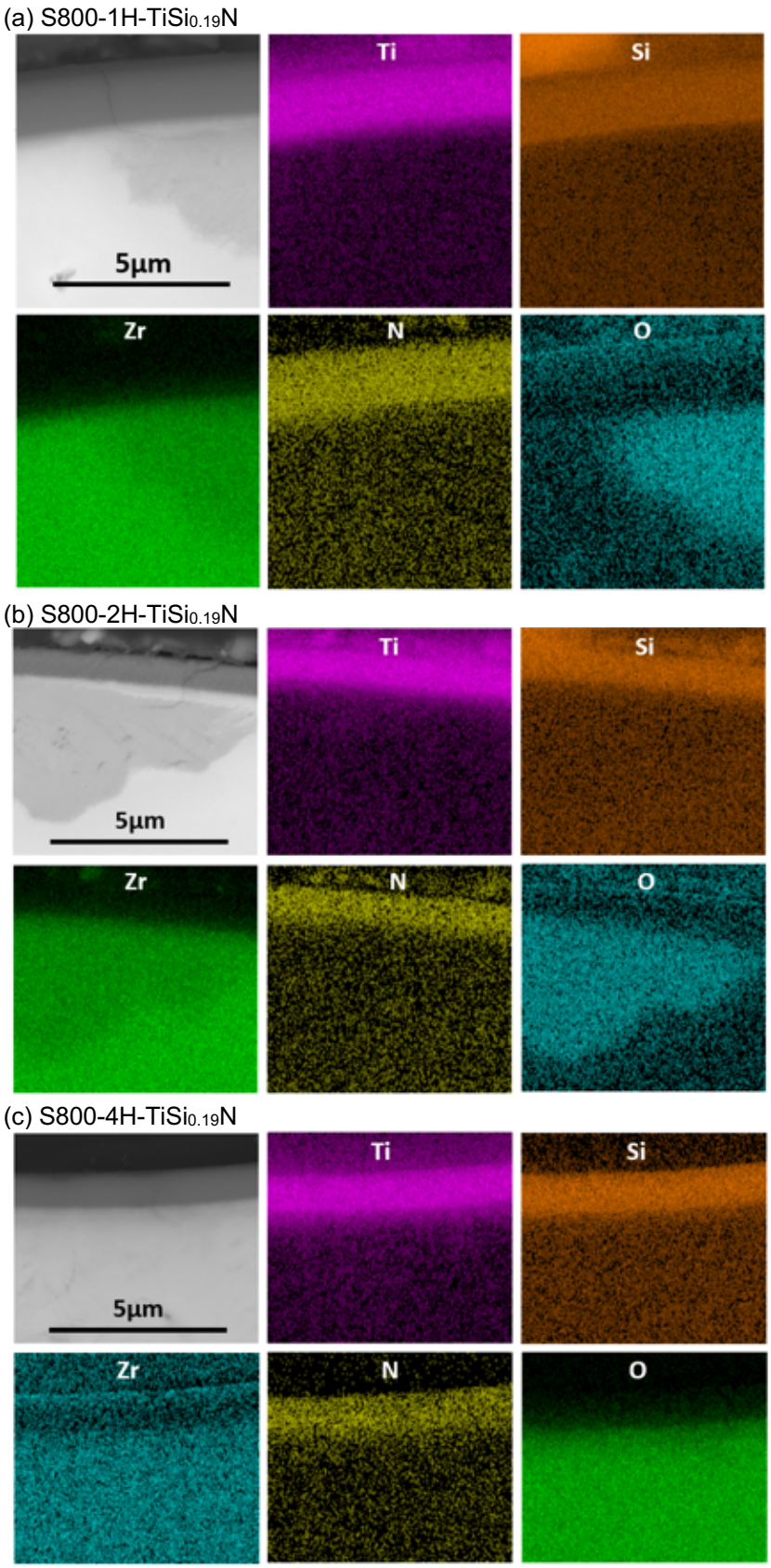

Figure 3-22 Cross-section SEM images in BSE mode of $TiSi_{0.08}N$, $TiSi_{0.13}N$ and $TiSi_{0.19}N$ after 1 and 2 hour 800°C steam test and enlarged area EDS mapping.

Figure 3-21 showed the BSE SEM images and EDS mapping images of $TiSi_{0.08}N$ steam treated at 800°C. Titanium, silicon and nitrogen remained stable within $TiSi_{0.08}N$ region. The very low intensity of oxygen presented within all $TiSi_xN$/Ti layer. Clear Zr and O

signal detected from Zr substrate beneath the $TiSi_xN$/Ti coating. A layer containing O, Ti Si and Zr formed at the Ti-interlayer region between $TiSi_{0.08}N$ coating and Zr. Oxygen distributed uniformly within this layer while Ti and Zr showed diffusion gradient towards substrate and coating, respectively. Ti signal decreased from $TiSi_xN$/Ti coating to substrate, while Zr signal increased. Si showed depletion at this layer, especially in $TiSi_{0.08}N$ after 1-hour test. It indicated that diffusion occurred between $TiSi_xN$/Ti bilayer and Zr substrate and oxidation occurred at the diffusion layer. To summary, interdiffusion occurred at 800°C, however, Zr was still protected with presence of the $TiSi_xN$/Ti coatings provided that there was no crack or damage in the coatings.

3.2.4. 1000°C steam oxidation characterisation

3.2.4.1. Phase identification

Figure 3-23 presented GIXRD results of $TiSi_xN$/Ti coatings and bare Zy-4 substrate after 1, 2 and 4 hours steam oxidation at 1000°C, which showed significant changes in phases in comparison with that at 600°C and 800°C. Figure 3-23 illustrated multiple phases with sharp peaks. The primary phase of bare Zy-4 substrate after 1 hour 1000°C steam test detected with strong intensity peaks at 28.2°and 34.1° was M-ZrO_2. While the T-ZrO_2 phase was also confirmed in Zy-4 treated by 1 hour steam at 1000°C by a low-intensity peak at 30.2°, which was similar to 800°C tested series. Analogous results of ZrO_2 phases presented in all the coated samples after 1000°C steam tests. Especially, M-ZrO_2 was the dominant phase in $TiSi_{0.13}N$/Ti and $TiSi_{0.19}N$/Ti after 1 to 4 hours 1000°C steam test, while it became subordinate in $TiSi_{0.08}N$/Ti. Signal of Zr was not apparent after 1000°C steam tests compared to 600°C and 800°C treatments for both substrates and coated samples. We believe that the substrate beneath $TiSi_xN$/Ti coatings was oxidised and a significant amount of zirconium oxide was formed under 1000°C. The oxidation condition needed to be verified by cross-section SEM analysis and elemental analysis.

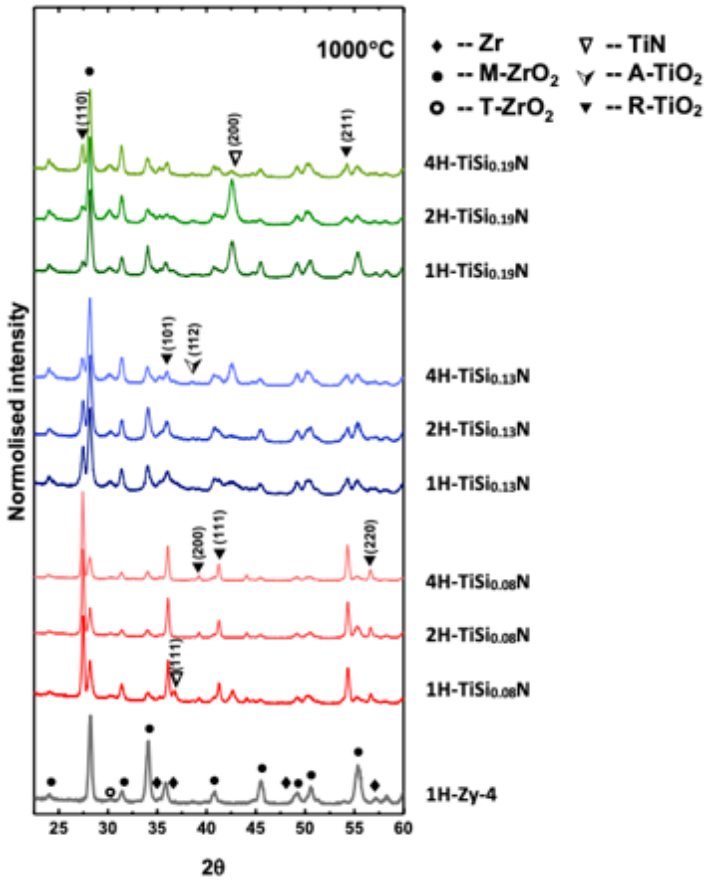

Figure 3-23 GIXRD patterns with incident angle 2° of single-side-polished bare Zy-4 bulk after 1h 1000°C steam test, and TiSiN coatings with Zy-4 substrate after 1h, 2h and 4h 1000°C steam test.

According to the XRD results, it suggested that various crystal oxide phases formed after 1000°C steam tests. Rutile (R-TiO_2, ICDD: 01-078-4188) was the predominant phase in $TiSi_{0.08}N$/Ti coating tested in 1000°C steam. The R-TiO_2 formed in $TiSi_{0.08}N$/Ti showed an intense peak at 27.4° with diffraction plane (110). $TiSi_{0.08}N$/Ti coating remained the TiN (111) and TiN (200) peaks after 1 hour 1000°C steam test, while TiN signal disappeared after 2 and 4 hours tests. Apart from ZrO_2, TiN (200) phase was still a compatible phase in $TiSi_{0.13}N$/Ti and $TiSi_{0.19}N$/Ti according to a sharp peak discovers at 42.9° after 1000°C steam test. The TiN peaks presented in $TiSi_{0.13}N$/Ti and $TiSi_{0.19}N$/Ti treated at 1000°C were similar to those after 800°C. What's more, as the temperature increased to 1000°C, anatase (A-TiO_2) begin to form with a weak peak at 38.6° in all three $TiSi_xN$ coatings. Two types of TiO_2 formed on all $TiSi_xN$ coatings after the steam tests at 1000°C, which made a difference from those after 600°C and 800°C tests. It suggested that as the steam temperature rises, the formation of TiN crystal apart from amorphous particles occurred, or nano-sized grain started to grow.

3.2.4.2. Surface morphology and elemental analysis

High magnification SEM images shown in Figure 3-24 illustrated a significant difference in surface morphology of $TiSi_xN$ coatings treated at 1000°C from the former two temperature ranges 600°C and 800°C. First, all surfaces showed crystalline particles after all periods of the 1000°C steam tests. However, $TiSi_xN$ coatings with different Si contents showed a comparable difference in crystal size. $TiSi_{0.08}N$/Ti showed the largest grain in hundred nanoscales, while $TiSi_{0.13}N$/Ti showed the finest grain in few nanoscale after 1000°C steam tests. The grain size of oxidation products at 1000°C showed none linear relation with the original Si content. What's more, as the steam period increased (from 1h to 2h and 4h), all coatings treated by 1000°C steam showed a noticeable grain growth regardless of Si percentage. One more significant point was that the grain size of $TiSi_{0.08}N$/Ti was the largest among all samples after 1000°C steam treatments, which showed the largest difference in grain size compare to as-deposited state. While samples treated at 600°C and 800°C did not experience significant grain growth compared to the as-deposited coatings.

As data shown in Table 3-1, when the steam test conducted at 1000°C, the ratio of Ti and O reached 1:2, which indicated the formation of stoichiometric TiO_2. It was also consistent with the TiO_2 crystalline peaks from GIXRD. At the same time, N faced a total depletion from $TiSi_xN$ coatings, and the concentration of Si dropped dramatically.

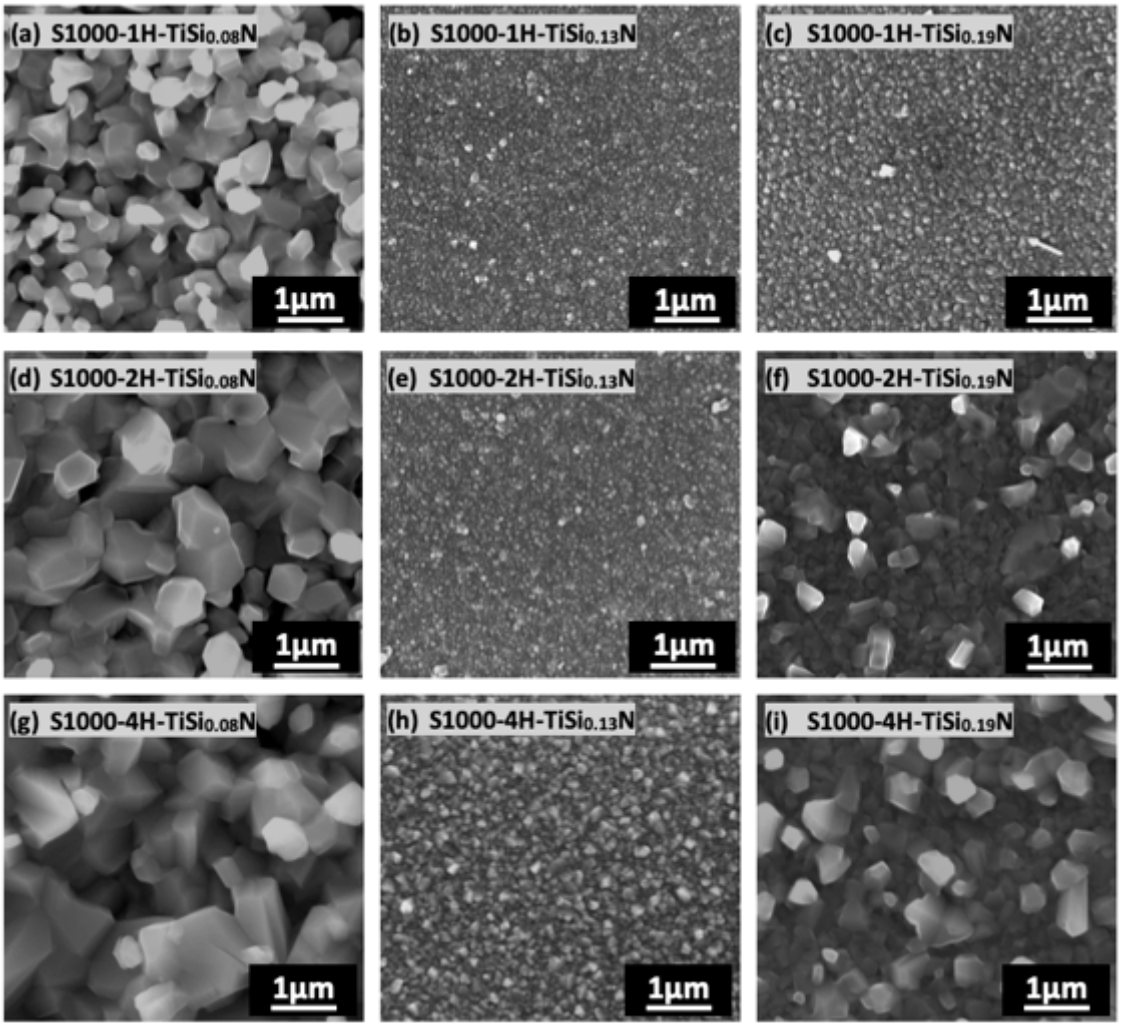

Figure 3-24 High magnification images (50000x) of $TiSi_{0.08}N$/Ti, $TiSi_{0.13}N$/Ti and $TiSi_{0.19}N$/Ti coating surface morphology after 1h, 2h, and 4h steam tests at and 1000°C

3.2.4.3. Oxidation kinetics

Evidence of steam protection was found in cross-section image of $TiSi_{0.19}N$/Ti after 1 hour and 2 hours steam tests at 1000°C, Figure 3-25(c). The beneath Zy-4 substrate remained un-attacked with $TiSi_{0.19}N$ coating attached after 1000°C steam test and rapid cooling. It demonstrated that $TiSi_{0.19}N$/Ti coating could protect Zy-4 from steam attack for 2 hours under 1000°C.

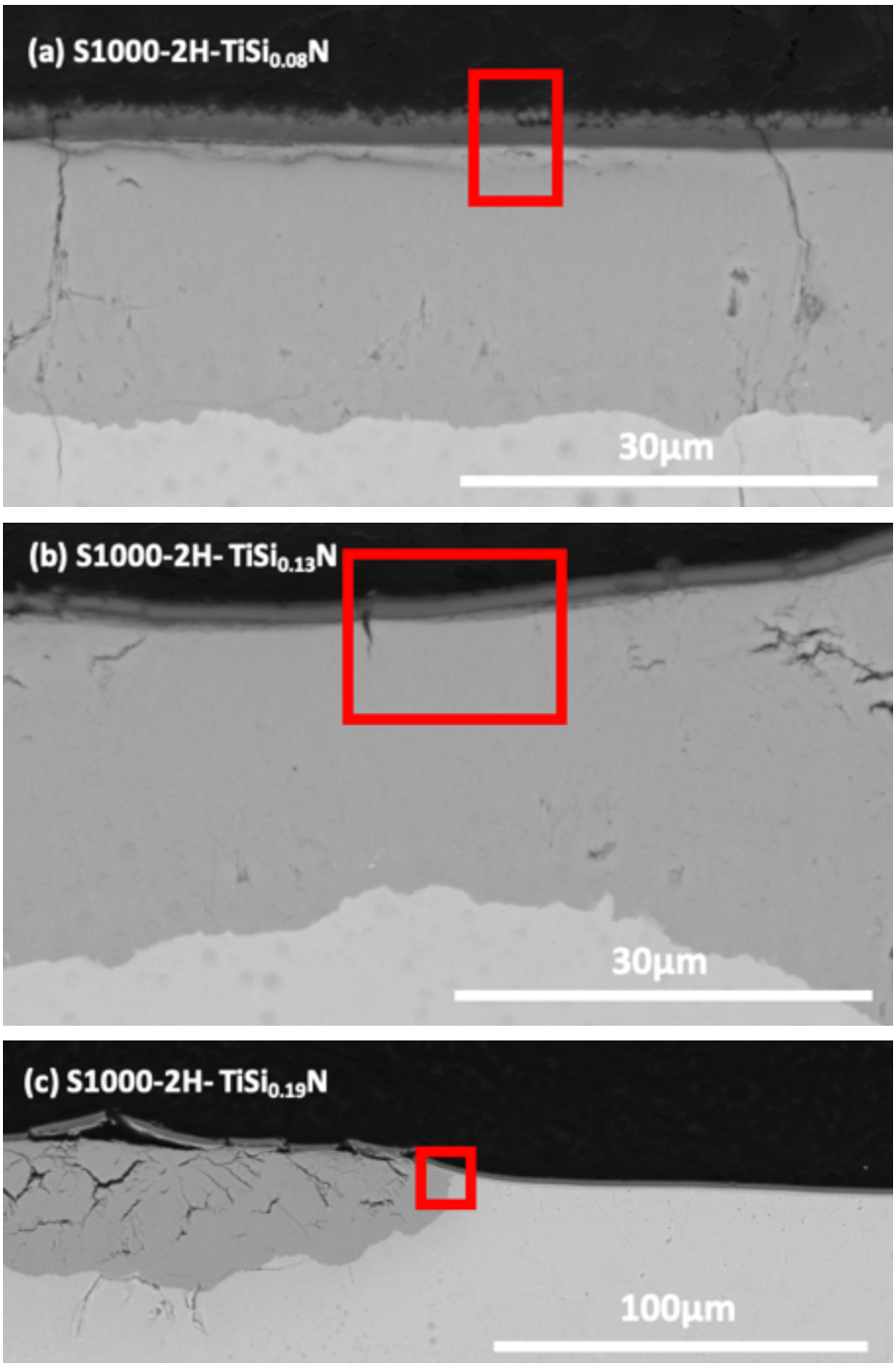

Figure 3-25 Cross-section SEM images in BSE mode of (a) $TiSi_{0.08}N$/Ti, (b) $TiSi_{0.13}N$/Ti and (c) $TiSi_{0.19}N$/Ti after 2 hours 1000°C steam test, the red squares marked as EDS mapping area in Figure 3-26(b), Figure 3-27(b), and Figure 3-28(b)

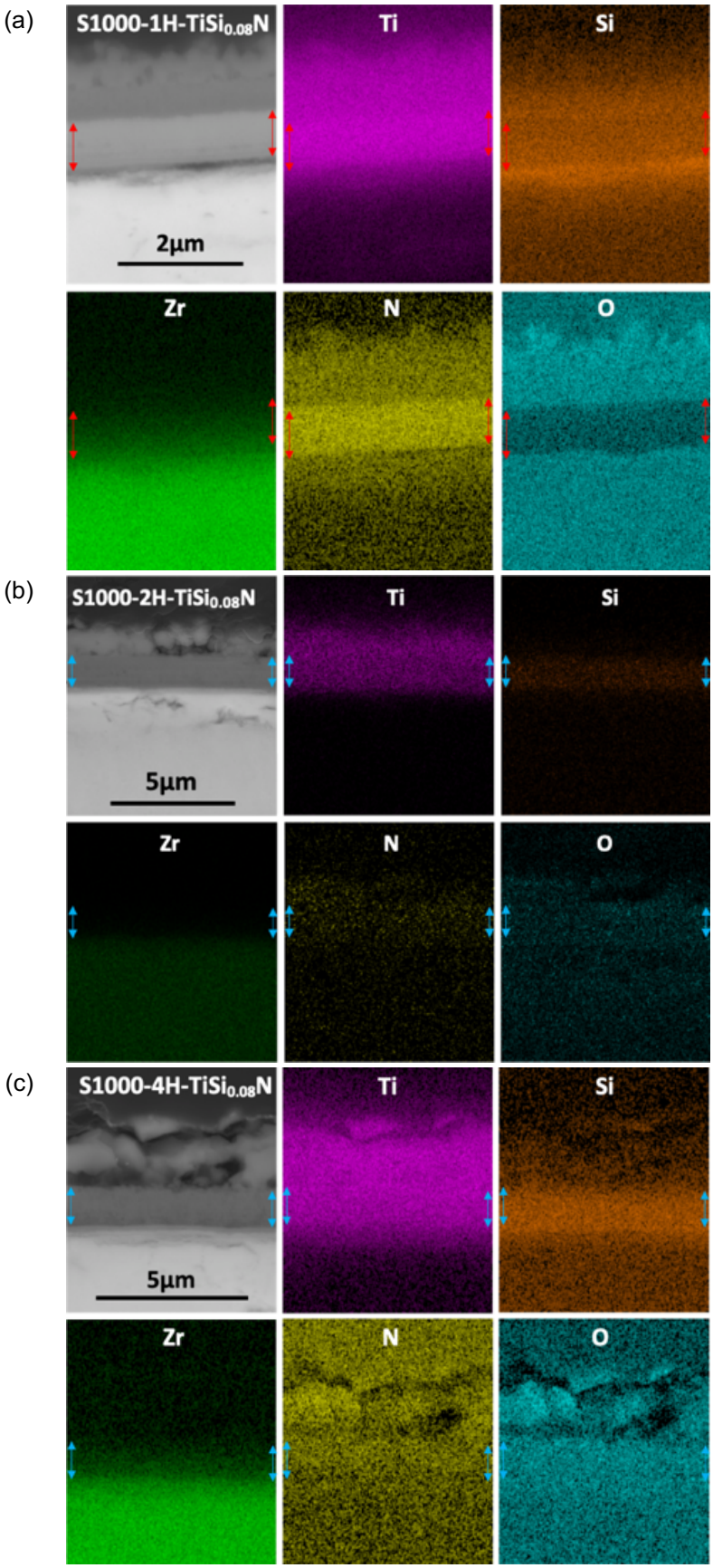

Figure 3-26 Cross-section EDS mappings of $TiSi_{0.08}N$/Ti coatings after (a) 1h and (b) 2h steam test at 1000°C

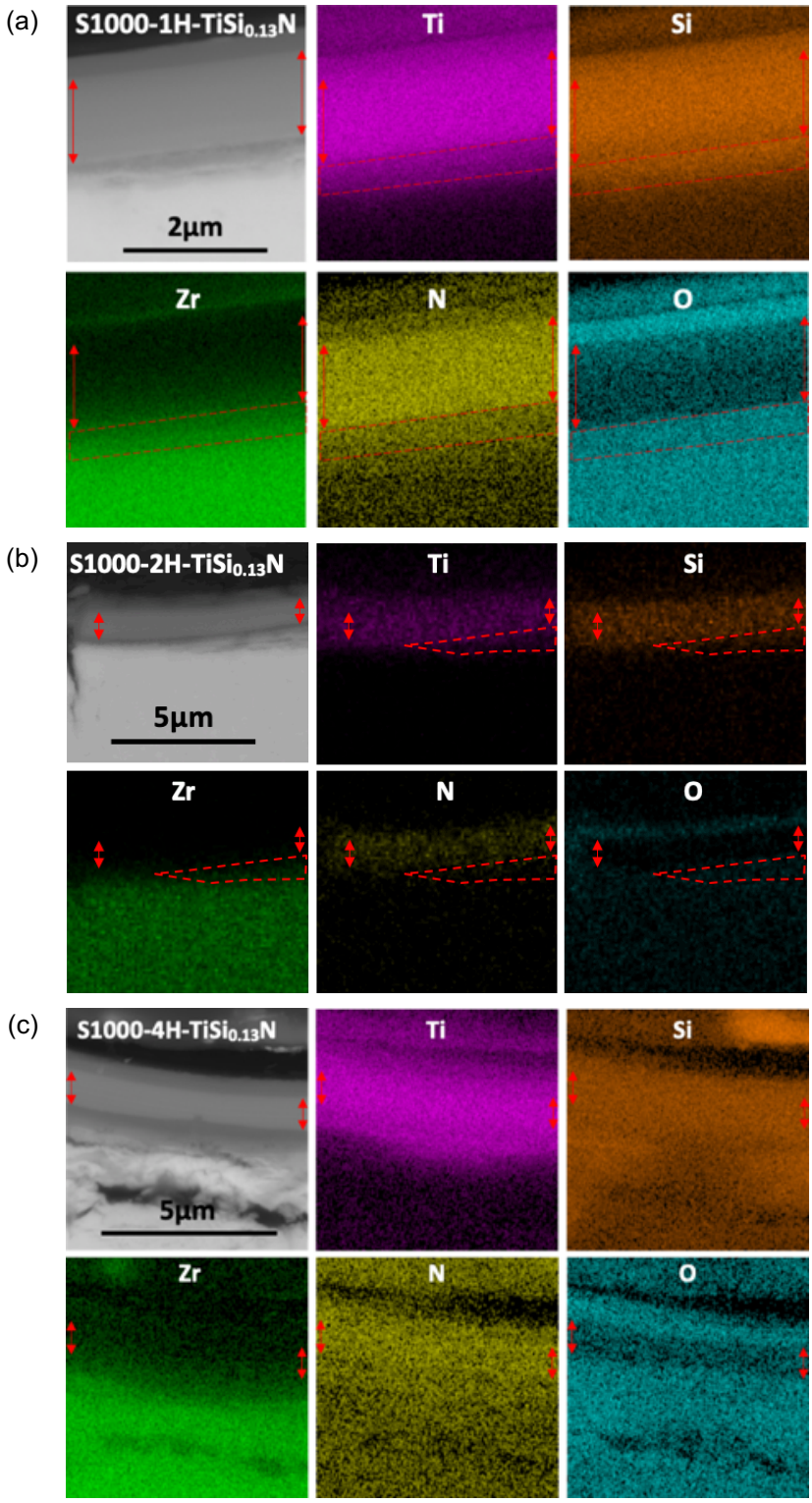

Figure 3-27 Cross-section EDS mapping of $TiSi_{0.08}N$/Ti coatings after (a) 1 hour and (b) 2 hours steam test at 1000°C

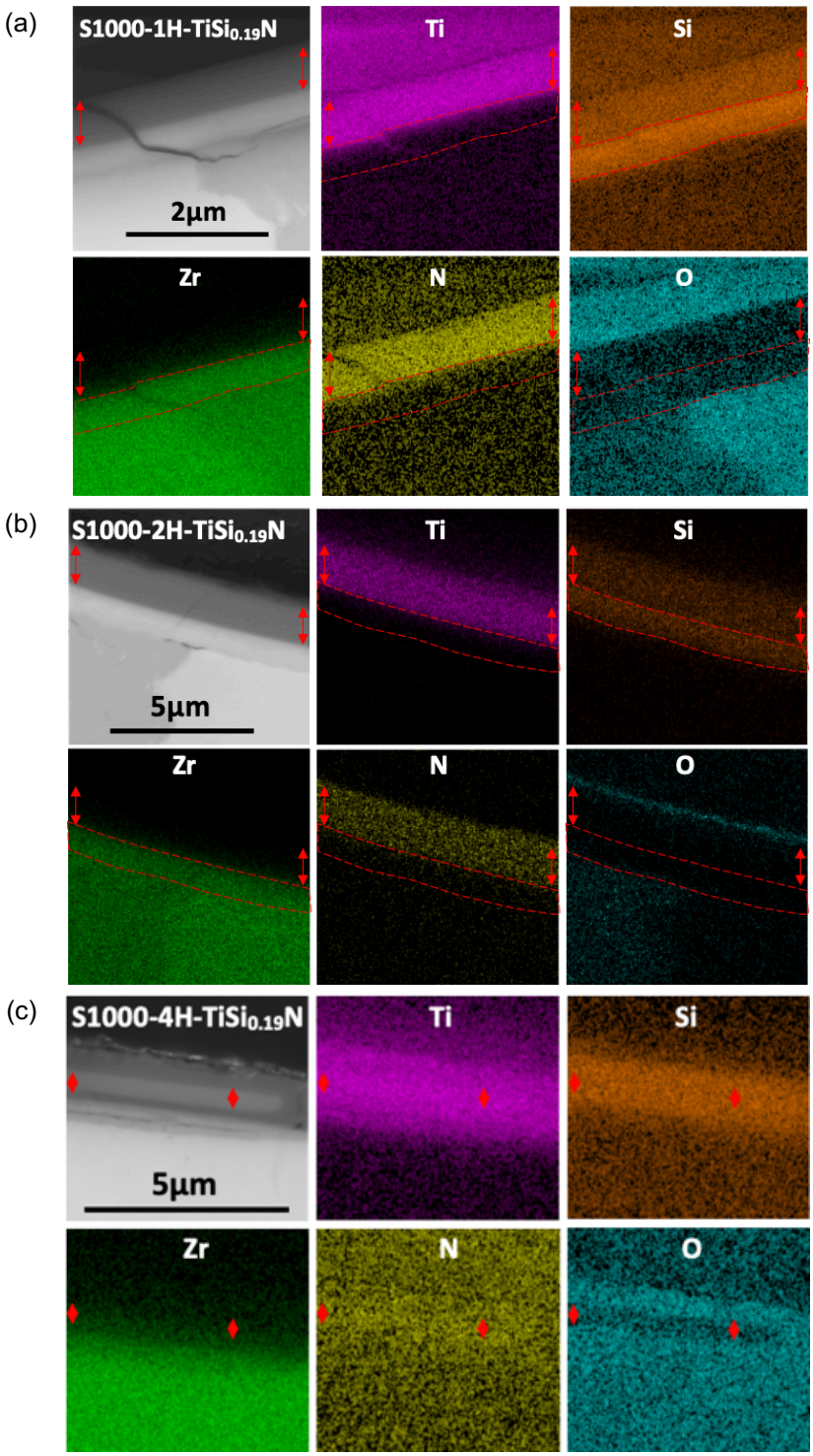

Figure 3-28 Cross-section SEM images in BSE mode and EDS mappings of $TiSi_{0.19}N$ after 1 and 2 hours 1000°C steam test

Figure 3-26 showed the BSE images and EDS mappings of $TiSi_{0.08}N$/Ti cross-section after 1h, 2h and 4h 1000°C steam test. It showed an oxygen concentrated layer with a porous structure at the top surface. The porous morphology from cross-section was consistent with the observation of the large crystalline oxide particles from the surface. Apart from oxygen, this layer also consisted of Ti, Si and N.

The grey layer in $TiSi_{0.08}N$/Ti after 1 hour 1000°C test marked by the red arrows showed a significant amount of Ti, N, moderate of Si and weak signal of O, which was the un-corroded $TiSi_{0.08}N$/Ti coating part. The thickness of remained $TiSi_{0.08}N$/Ti coating was around 0.78μm. However, from $TiSi_{0.08}N$/Ti after 2 hours test, we found clear oxidation evidence that the relatively dense layer (1.34μm) marked by blue arrow showed a significant amount of oxygen as well as Ti, Si and N. According to the EDS results, a full range of oxidation occurred in $TiSi_{0.08}N$/Ti due to the uniform distribution of oxygen in the $TiSi_{0.08}N$ coating area. It was also consistent with the disappearance of TiN peaks shown in section 3.1.1. Apart from the porous oxide layer in 1 hour tested $TiSi_{0.08}N$/Ti, a unique two-layered oxide structure formed after 2 hours steam test under 1000°C. The upper oxide layer showed a more porous structure and a sign of Si loss, while the underneath oxide layer was relatively dense with comparable Si content. As the steam treatment increase to 4 hours at 1000°C, the upper porous oxide layer of $TiSi_{0.08}N$/Ti coating became thicker and the underneath oxide layer became porous compared to 2 hours tested coating. The change in the upper oxide layer from fine and porous structure to gradually increased grain size and porosity as the steam treatment time increase was consistent with the surface morphology, as shown in Figure 3-24.

Figure 3-27 and Figure 3-28 illustrated EDS mappings of $TiSi_{0.13}N$/Ti and $TiSi_{0.19}N$/Ti samples after 1h, 2h and 4h steam test at 1000°C. Despite the underneath corroded Zr, only a very thin layer of oxygen was detected from both $TiSi_{0.13}N$/Ti and $TiSi_{0.19}N$/Ti.

After 1 hour 1000°C steam test, a layer with 1.1μm in thickness remained unattack by steam, and the oxide layer formed on the surface was relatively dense and flat. It agreed with the surface morphology that $TiSi_{0.13}N$/Ti showed the finest oxide particles. The oxide layer formed on $TiSi_{0.13}N$/Ti was thinner compared with $TiSi_{0.08}N$/Ti. After 4 hours test, $TiSi_{0.13}N$/Ti remained an un-corroded layer, and the oxide layer formed remained dense.

In the cross-section BSE image (Figure 3-27) of 2 hours 1000°C tested $TiSi_{0.19}N$/Ti, a clear interlayer was formed between $TiSi_{0.19}N$/Ti coating and Zy-4 substrate, with a

significant amount of Si and Zr, marked with the red dashed line. Severe diffusion of Si from $TiSi_{0.19}N$/Ti coatings path through Ti-interlayer to Zy-4 substrate occurred after 2 hours steam test at 1000°C. However, $TiSi_{0.19}N$/Ti still showed the best corrosion resistance among these three $TiSi_xN$ coatings.

Compare SEM surface and cross-section images of three $TiSi_xN$/Ti coatings, $TiSi_{0.08}N$/Ti coatings showed the largest surface oxide crystal and the thickest porous surface oxide layer. $TiSi_{0.13}N$/Ti showed the smallest oxide size and the smoothest surface oxide layer.

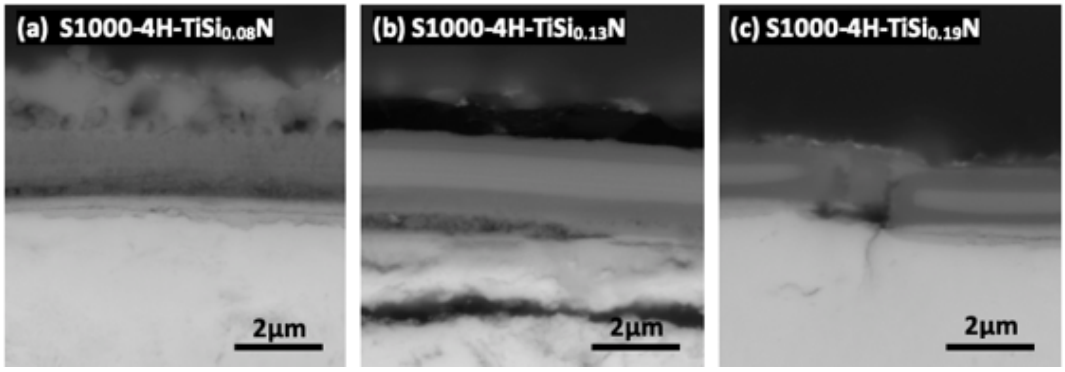

Figure 3-29 Cross-section BSE images of $TiSi_xN$ coatings after 4 hours steam test at 1000°C

3.2.5. Summary

Based on the XRD patterns and EDS analysis shown above, the corrosion behaviour in surface morphology and cross-section elemental distribution under steam environment showed significant difference under 600°C, 800°C and 1000°C. Nano-sized round particles of oxides uniformly distributed through the whole surface of all three TiSiN coatings after various period steam tests at 600°C and 800°C, while the oxidation was not severe, so the amount of oxides was below the detection limit of XRD. Oxides formed on TiSiN after 600°C and 800°C steam treatments were non-stoichiometric TiO_x. However, after 1000°C steam test, significant amount of crystalline TiO_2 was formed. Without formation of crack in the coatings, the underline Zr alloy was still protected. On the other hand, where crack was formed in the coating, ZrO_2 formed beneath the cracked coating area. To conclude, TiSiN series coatings could provide steam resistance at 600°C for at least 4 hours, $TiSi_{0.13}N$/Ti and $TiSi_{0.19}N$/Ti could stand 1000°C steam attack for 4 hours.

3.3. Corrosion behaviour in autoclave

Apart from accident scenarios, the regular working operation was the primary criterion for the design of ATF claddings. Since over 18-month immersion in the coolant water at high-temperature and high-pressure associated with irradiation could cause significant impact on cladding properties. The autoclave test was used to simulate the PWR primary coolant environment at 360°C, 18.7MPa. In this section, we focused on further corrosion behaviour study of the nitride ceramic coating system under PWR working condition. First part of this section mainly described pressurised water corrosion behaviour of single layer ZrN coating, similar delamination occurred under water compared to the former introduced steam environment. Through thickness oxidation happened to ZrN coating after 3 days autoclave test, with porous oxide layer structure. The second part gave a comparison of TiN and TiSiN single layer coating on Si wafer. TiN showed 4 times corrosion resistance better than TiSiN under water, which showed contradictory to steam resistance behaviour. Last section, we focused on the study of Si addition effect on $TiSi_xN$ waterside corrosion behaviour.

3.3.1. Corrosion behaviour of ZrN

Figure 3-30 presented different surface morphology of ZrN after 3-day in an autoclave at different location. From the low magnification SEM image of the ZrN coating surface after 3 days autoclave test, Figure 3-30(a), only pieces of coating remained on the surface. It indicated that the bonding between ZrN coating and Zr alloy substrate was not sufficient to withstand the thermal mismatch during autoclave tests. With high magnification SEM image shown in Figure 3-30(b) and (c), both the attached ZrO_2 shards and the exposed Zr substrate surface presented nano-sized spherical oxide particles. Both the attached shards and the exposed Zr substrate surface were identified as ZrO_2 by EDS point analysis. However, the two surfaces showed a significant difference in oxide microstructure. The oxidised ZrN coating surface appeared to be more dense and smooth structure while the oxides formed on the exposed Zr substrate

were relatively loose and uneven, according to the FIB cross-section image of the attached shards area, Figure 3-31(a).

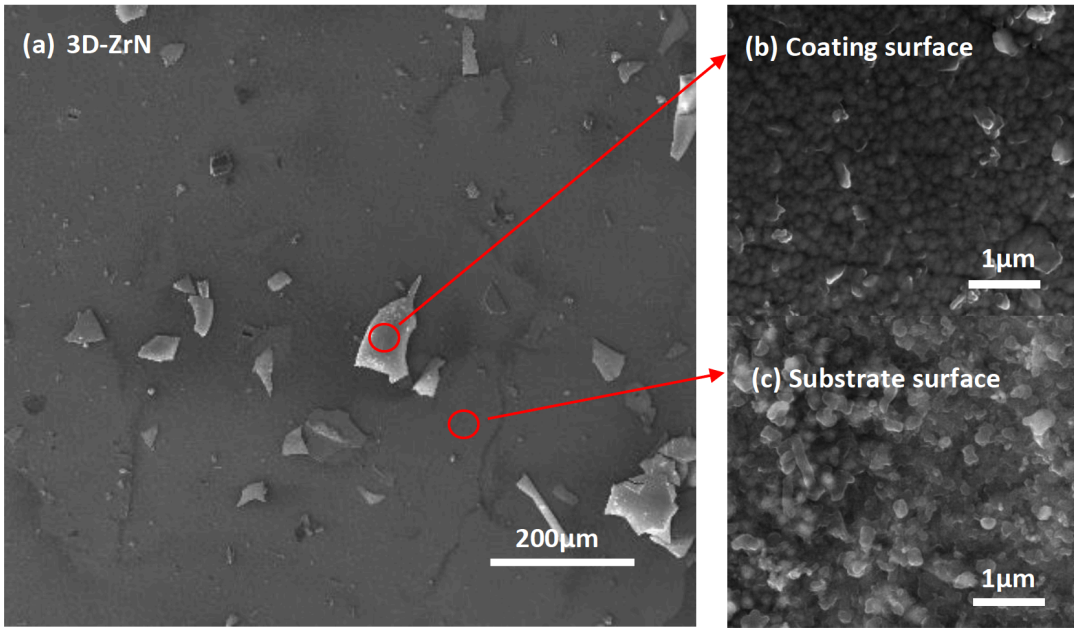

Figure 3-30 (a) Low magnification of surface morphology, high magnification of (b) surface shards (c) coating spalled off area of ZrN coating with Zr substrate after the 3-day autoclave test

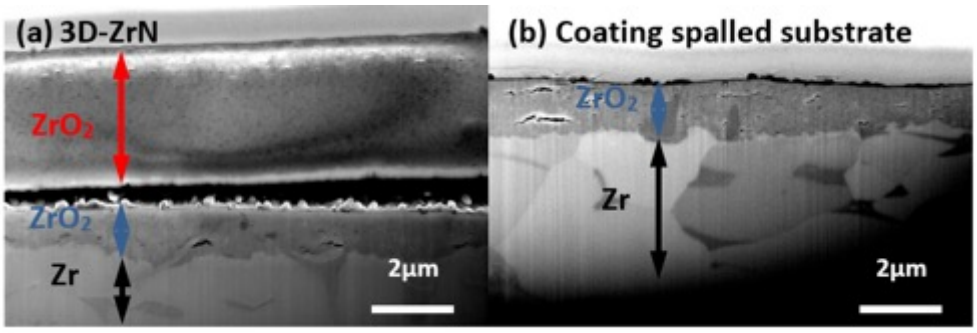

Figure 3-31 SEM image of as-deposit coating cross-section (a) oxidised ZrN coating on Zr alloy substrate, (b) coating spalled substrate cross-section.

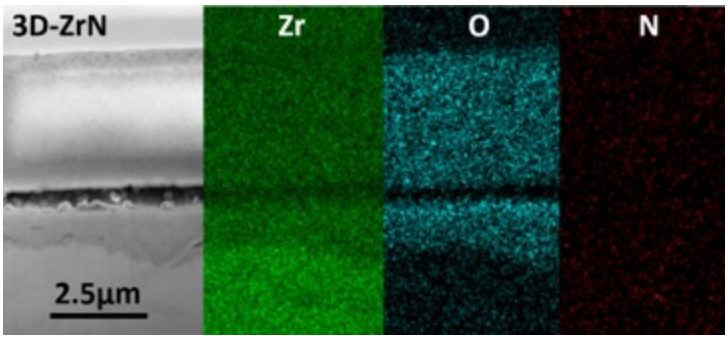

Figure 3-32 Cross-section EDS mapping image of 3-day autoclave tested ZrN coating on Zr substrate

Figure 3-31(a) and (b) showed the FIB cross-section cut through the remained shard. Red arrows index the oxidised ZrN coating. Blue arrows index a layer of oxide formed by oxidation of the substrate after 3-day of water corrosion. Black arrows label the

unaffected Zr alloy substrate. The layer components were also confirmed by the element distribution of 3D-ZrN shown in Figure 3-32. ZrN coating fully oxidised into ZrO_2 associated with the thickness increment to 3.55μm. Apart from the relatively dense surface morphology of ZrN oxidised shards, the oxide layer formed by corrosion of ZrN coating showed a porous structure. Severe delamination and spallation occurred on the ZrN coated Zr sample. There was a thin layer of small oxide particles peeled off from the oxidised ZrN coating during spallation and attached to the Zr substrate. So instead of oxide formed from the Zr substrate, the above observed porous oxide surface where the ZrN spalled surface was the attached nano-oxide particles spalled off from the oxidised ZrN coating. The substrate surface remained smooth even after oxidation, as shown in the cross-section FIB image Figure 3-31. It indicated the delamination occurs along with the ZrN-Zr interface and within the fully oxidised ZrN layer. It can be assumed that the ZrN layers underwent severe oxidation under pressurised water condition, and the oxidised layer could not bear the volume increment induced stress and thermal mismatch which led to delamination of ZrO_2 layer. It led to exposure of the underneath Zr-substrate to the harsh environment directly, which caused oxidation of the Zr alloy substrate.

The Zr-substrate oxide layer contained lateral cracks and porous near the interface of oxide and metal (Figure 3-31). Compare with the area where ZrN coating spalled off, the thickness of oxide formed on the Zr-substrate was slightly less than the buried area under the corroded ZrN layer. It indicated that corrosion starts by attacking ZrN layer during heating and water corrosion and continues to attack the underneath or exposed Zr substrate. It appeared that severe delamination between the ZrN and Zr alloy substrate occurred during the 3-day autoclave test but not at the very beginning heating process.

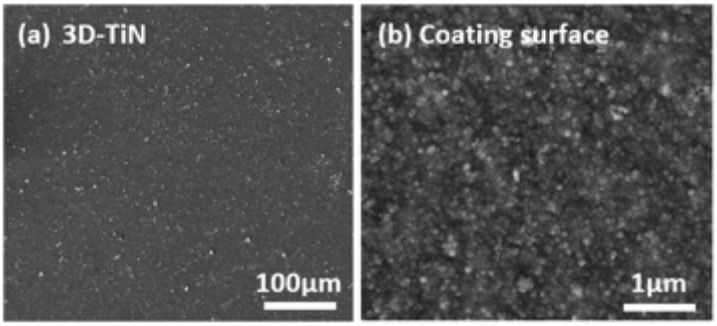

Figure 3-33 (a) Low magnification surface morphology and (b) high magnification morphology of TiN coating with Si substrate after 3-day autoclave test

3.3.2. Corrosion behaviour of TiN and TiSiN

Figure 3-33 presented the surface morphology of the TiN coating after 3-day autoclave test. Relatively smooth surface and randomly distributed particles were visible. No cracks or spallation occurred according to the surface investigation. From the higher magnification SEM image Figure 3-33(b), nano spherical oxide particles uniformly formed on the surface of TiN coating. However, regarding the corrosion behaviour of the TiN-coated sample, neither flaking nor galvanic corrosion appearances were observed at the Si-substrate and sputtering coated interface and sample cutting edges. A thin layer of TiO_2 formed at the top surface with the thickness around 300nm, as confirmed in Figure 3-34.

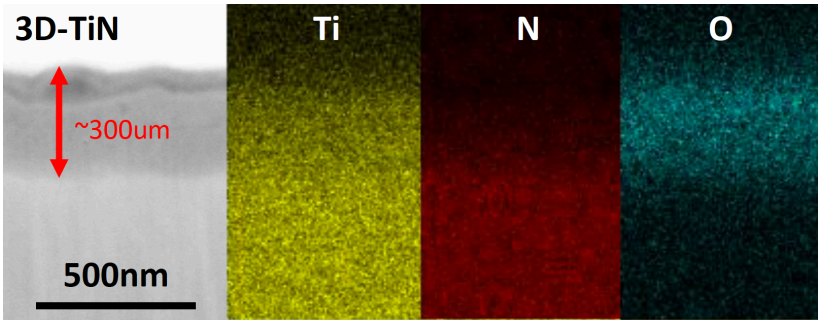

Figure 3-34 Cross-section EDS mapping images of 3-day autoclave tested TiN coatings on Si substrate

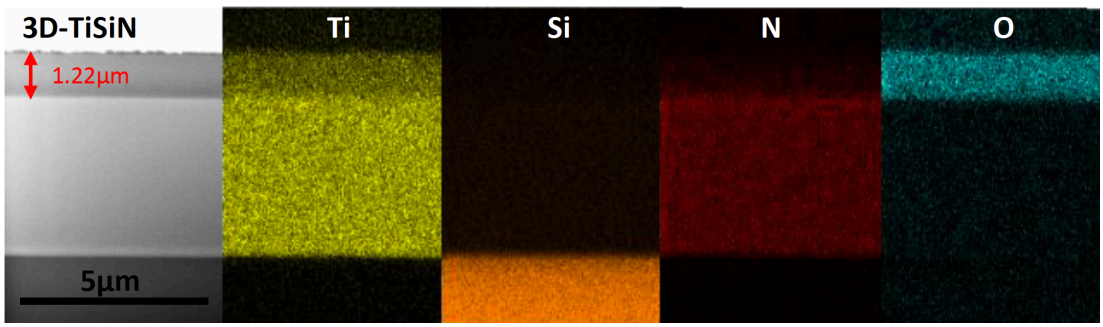

Figure 3-35 Cross-section SEM image of 3-day autoclave tested TiSiN coatings on Si substrate

However, according to the EDS mapping of TiSiN coating with Si substrate, as shown in Figure 3-35, the oxide layer formed showed a thickness of 1.22μm. By comparing 3-day autoclave tested TiN and TiSiN, the remarkable variety of thickness indicated that TiN had better corrosion resistance against water, which was opposite to many existed literatures. Further studies need to focus on the effects of Si content on the corrosion resistance of TiSiN coatings under simulated PWR working condition.

3.3.3. Autoclave corrosion behaviour of $TiSi_xN$/Ti bilayer coating

3.3.3.1. Phase identification

Figure 3-36 listed normalised GIXRD patterns with 2° incidence angle of $TiSi_xN$/Ti coatings (x=0.08, 0.13 and 0.19) after series autoclave tests. The grey lines at the bottom of each graph presented the as-received Zy-4 substrates as a reference to eliminate the Zr peak from $TiSi_xN$/Ti coated samples. And the black lines represented GIXRD patterns with 3° incidence angle of the as-deposited $TiSi_xN$/Ti samples as a reference to determine the TiN phase and compare phase changes after autoclave test. Compared to GIXRD (3°) results of as-deposited $TiSi_xN$/Ti coatings, Zr was no more the main phase detected by GIXRD (2°) results of autoclave test $TiSi_xN$/Ti coatings due to the less penetration depth of X-ray with lower incidence angle. No significant signals from M-ZrO_2 detected from $TiSi_{0.08}N$/Ti and $TiSi_{0.19}N$/Ti coatings after autoclave immersion. Only $TiSi_{0.13}N$/Ti samples after 3-day immersion test showed relatively distinct peaks and shoulder-like peaks of M-ZrO_2 at 28.167° and 34.799° near Zr peak, respectively.

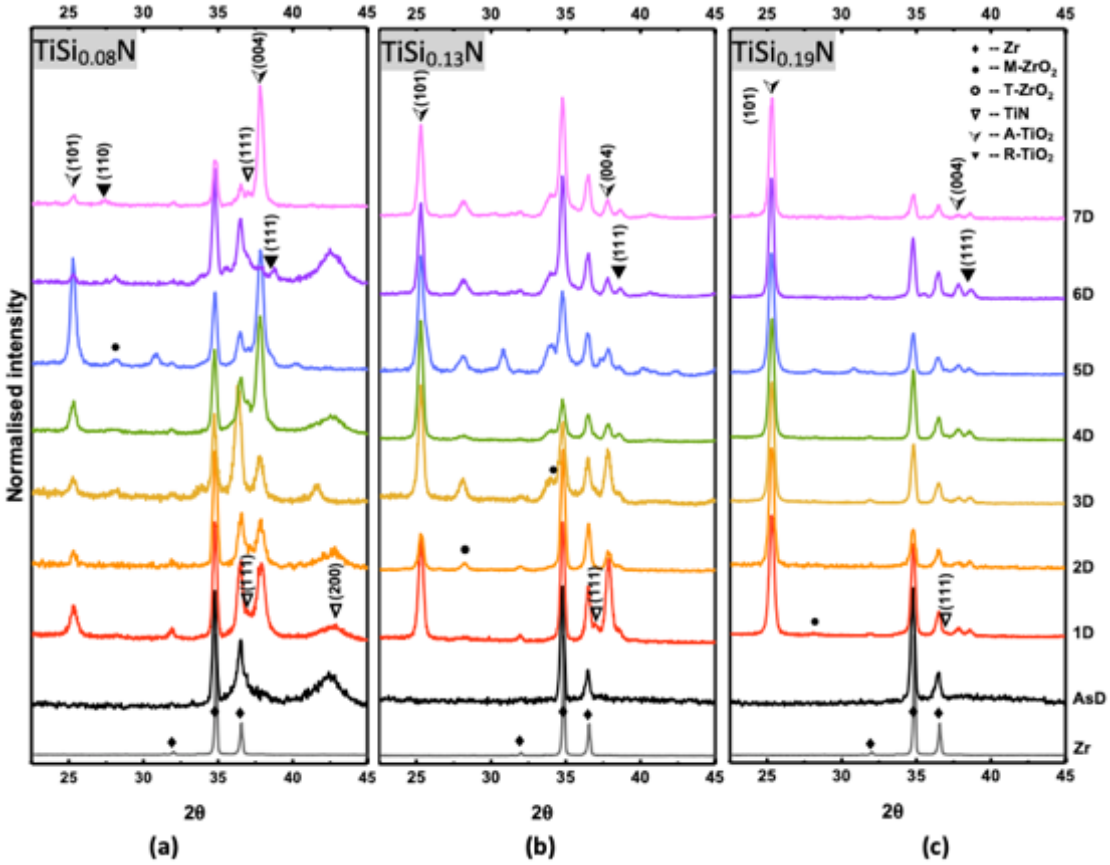

Figure 3-36 Normalised GIXRD patterns of autoclave tested $TiSi_xN$ coating samples for 1 to 7 day, as-deposited and Zr substrate used as reference patterns.

$TiSi_{0.08}N$/Ti coatings, after 1, 2, 4 and 6 days autoclave test, showed broadened TiN (200) peaks at 48.87°. This phenomenon did not happen to $TiSi_{0.08}N$/Ti coatings after 5 and 7 days tests. Accompanied by the SEM cross-section elemental analysis, the reason for the absence of TiN peak in 5- and 7-day tested $TiSi_{0.08}N$/Ti coating was due to the thick surface sedimentation layer of Cr-contained oxide. An x-ray could not reach the un-corroded $TiSi_{0.08}N$ layer through Cr-O layer and oxidised $TiSi_{0.08}N$ layer. $TiSi_{0.08}N$/Ti after 7-day autoclave test still contained TiN phase with diffraction plane (111). The XRD results of $TiSi_{0.08}N$/Ti suggested that still part of $TiSi_{0.08}N$/Ti coating remained uncorroded after 7-day immersion. However, barely no clear bulge at TiN peak positions occurred in $TiSi_{0.13}N$ and $TiSi_{0.19}N$ after 1-7 days series autoclave tests, which was similar as the as-deposited states but different compared to high-temperature steam treatment caused recrystallization and nano-grain growth. It was hard to distinguish if un-attacked $TiSi_{0.13}N$ and $TiSi_{0.19}N$ remained in autoclave test environment, further SEM investigation is needed.

After 1 day autoclave immersion, besides the peak of Zr and TiN, A-TiO_2 (anatase) with diffraction plane (004) was the main phase of all the $TiSi_{0.08}N$/Ti, while intense A-TiO_2 (101) peaks at 25.3° represented as the predominant oxide phase in $TiSi_{0.13}N$ and $TiSi_{0.19}N$ samples. As the immersion test continuous, A-TiO_2 (004) became the dominant phase in $TiSi_{0.08}N$/Ti samples, A-TiO_2 (101) became compatible to Zr signal from substrate in $TiSi_{0.13}N$, while A-TiO2 (101) rather than Zr presented as the dominant phase in $TiSi_{0.19}N$/Ti coating. Intense A-TiO_2 (101) peak at 25.3° s also presented in all the autoclave tested $TiSi_{0.08}N$ samples. We could assume that substitution of Ti with Si caused TiN primary diffraction plane change, which led to the alternation of that in TiO_2.

There was a significant difference in $TiSi_{0.19}N$/Ti between as-deposited states and autoclave tested states. Strong A-TiO_2 was detected from even 1 day tested samples. Each autoclaved tested $TiSi_{0.19}N$/Ti sample after 1 to 7days showed the extreme similarity of the normalised intensity XRD patterns. What's more, the decrease of the substrate Zr signal could be observed as the immersion test continuous. This implied that $TiSi_{0.19}N$/Ti underwent critical oxidation from the first day of the autoclave immersion test, with a thicker oxide layer being formed as the immersion time increase.

3.3.3.2. Morphology and elemental analysis after 2 days autoclave test

A detailed SEM examination was conducted on surfaces, cross-sections and fracture surfaces to investigate the corrosion behaviour of $TiSi_xN$/Ti coated samples with various Si content. Figure 3-37 to Figure 3-39 showed the SEM images of surface morphology, cross-section BSE images and fracture cross section graphs with individual scale bars labelled. The surface morphology of coatings showed remarkably difference by aqueous corrosion attack, see Figure 3-37. For $TiSi_{0.08}N$/Ti and $TiSi_{0.13}N$/Ti, surfaces were relatively smooth. While the surface of $TiSi_{0.08}N$/Ti after 2 days immersion test showed a more grainy structure, with rougher surface compared to that of $TiSi_{0.13}N$/Ti. Similar sized particles or grains were formed on the surface compared to as-deposited TiSiN coatings (see Figure 3-4). In the high-temperature high-pressure water environment (360°C, 19.8MPa), the surface and cross-section morphology of

$TiSi_{0.19}N$/Ti with the highest Si content in this study was strikingly impaired, see Figure 3-37(c) and Figure 3-38(c). Coarse crystal particles were formed on the top of $TiSi_{0.19}N$/Ti surface after 2 days autoclave test, and relatively fine particles are underneath these coarse crystals layer. The significant difference of surface morphology among these three $TiSi_xN$ coatings was believed as a result of the grain size difference in the as-deposited state and the crystalline to amorphous transition due to increased Si composition.

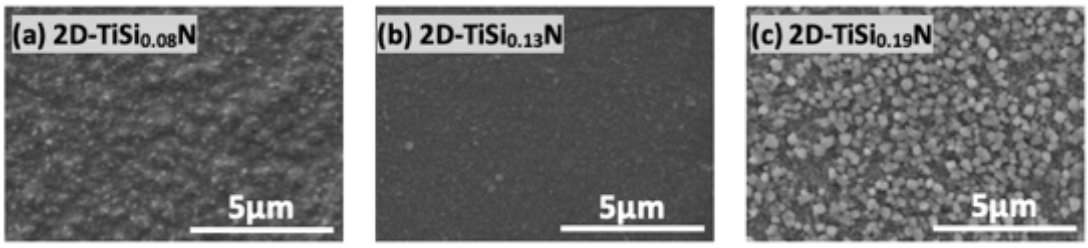

Figure 3-37 Surface morphology of (a) $TiSi_{0.08}N$/Ti, (b) $TiSi_{0.13}N$/Ti and (c) $TiSi_{0.19}N$/Ti coatings after 2 days autoclave test conducted by SEM in SE mode

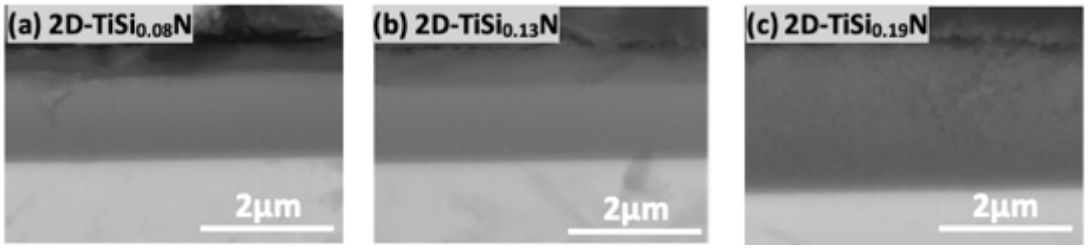

Figure 3-38 Cross-section image of (a) $TiSi_{0.08}N$/Ti, (b) $TiSi_{0.13}N$/Ti and (c) $TiSi_{0.19}N$/Ti coatings after 2 days autoclave test

Based on the contrast of the cross-section SEM images shown in Figure 3-38, oxide layers (darkest grey) exhibited on all three $TiSi_xN$ coatings. The cross-section images could not reveal precise microstructure, but only contrast due to the elemental composition. The darkest grey layers were identified as oxide layer by EDS point analysis. Underneath these oxide layers, the double-layered structure of original $TiSi_{0.08}N$/Ti and $TiSi_{0.13}N$/Ti was revealed in Figure 3-38(a)(b) and Figure 3-39(a)(b). The remained uncorroded $TiSi_{0.08}N$/Ti and $TiSi_{0.13}N$/Ti layers were dark greys. Ti-interlayers were the light grey layer between $TiSi_xN$ and substrate (lightest grey) with the thickness remained similar to the as-deposited state (approximately 100nm). $TiSi_{0.08}N$/Ti showed the best corrosion resistance due to the thinnest oxide layer after 2 days of autoclave test. Oxide layer showed dense and uniform and remained attached

to $TiSi_{0.08}N$/Ti and $TiSi_{0.13}N$/Ti layers. However, $TiSi_{0.19}N$/Ti coating was fully oxidised with porous oxide structure throughout the thickness. The Ti-interlayer of $TiSi_{0.19}N$/Ti remained dense and with no significant oxidation. No sign of oxidation occurred in the Zy-4 substrate. To summary, $TiSi_{0.08}N$/Ti showed the best corrosion resistance after 2 days of water attack, adhesion of the double layer structure was proofed stable in the pressurised water environment.

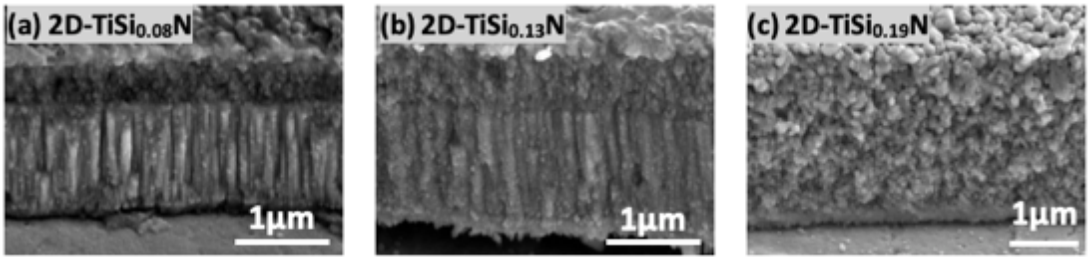

Figure 3-39 SEM images of (a) $TiSi_{0.08}N$/Ti, (b) $TiSi_{0.13}N$/Ti and (c) $TiSi_{0.19}N$/Ti coatings fracture surface morphology after 2 days autoclave test

Delamination and fracture of coatings occurred at the sample edges. From the fracture surface images Figure 3-39, the un-corroded part of $TiSi_{0.08}N$/Ti and $TiSi_{0.13}N$/Ti coatings showed columnar structure, while the oxide layers were uniform nano-sized particles. Also, some small fine particles formed on the fractured columnar surface. Because of the clear columnar structure and a small number of oxide particles, the fracture of coatings occurred during cooling as a result of thermal mismatch during the cooling.

According to the EDS mapping images of 2 days autoclave tested samples, shown in Figure 3-40, Ti, Si and N signals presented in the region of un-corroded $TiSi_xN$ region, and Zr was detected from the substrate area. While O presented at the top surface of $TiSi_{0.08}N$/Ti and $TiSi_{0.13}N$/Ti coatings and the whole part of $TiSi_{0.19}N$/Ti. There showed a gradient of Ti and Zr towards to substrate and coating layer, respectively. Accompanied by the EDS line scan as shown in Figure 3-41, the element atom percentage at the region where labelled Zr showed a decrease of Ti and N and an increase of Zr from the Ti-interlayer to the substrate. It suggested that diffusion took place between $TiSi_xN$/Ti double layer structure and Zy-4 substrate for 2 days autoclave test. Depletion of Si and N happened as a result of oxide layer formation as evident shown in all three EDS

mapping. The total loss of Si in $TiSi_{0.19}N$/Ti coating was attributed to the porous structure of oxide. Nitrogen still existed in the oxide layer and un-corroded coating region. Even with entire scale covered by oxygen, nitrogen signal in $TiSi_{0.19}N$/Ti coating was still active after 2 days autoclave test. It suggested that the coating was forming oxide as well as oxynitride[118]. Accompanied by the XRD results, only titanium oxide was formed, while no evidence showed that silicon oxide was generated during the autoclave test.

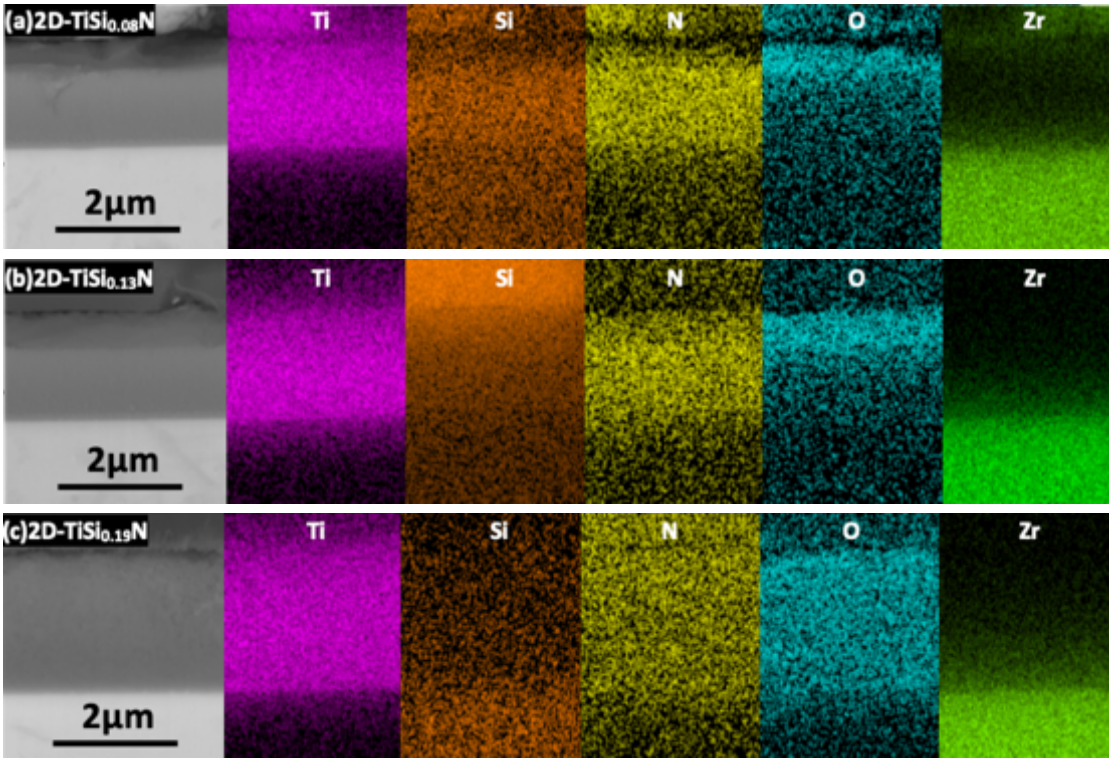

Figure 3-40 Cross-section SEM images and EDS mappings of (a) $TiSi_{0.08}N$/Ti , (b) $TiSi_{0.13}N$/Ti and (c) $TiSi_{0.19}N$/Ti after 2 days autoclave immersion test

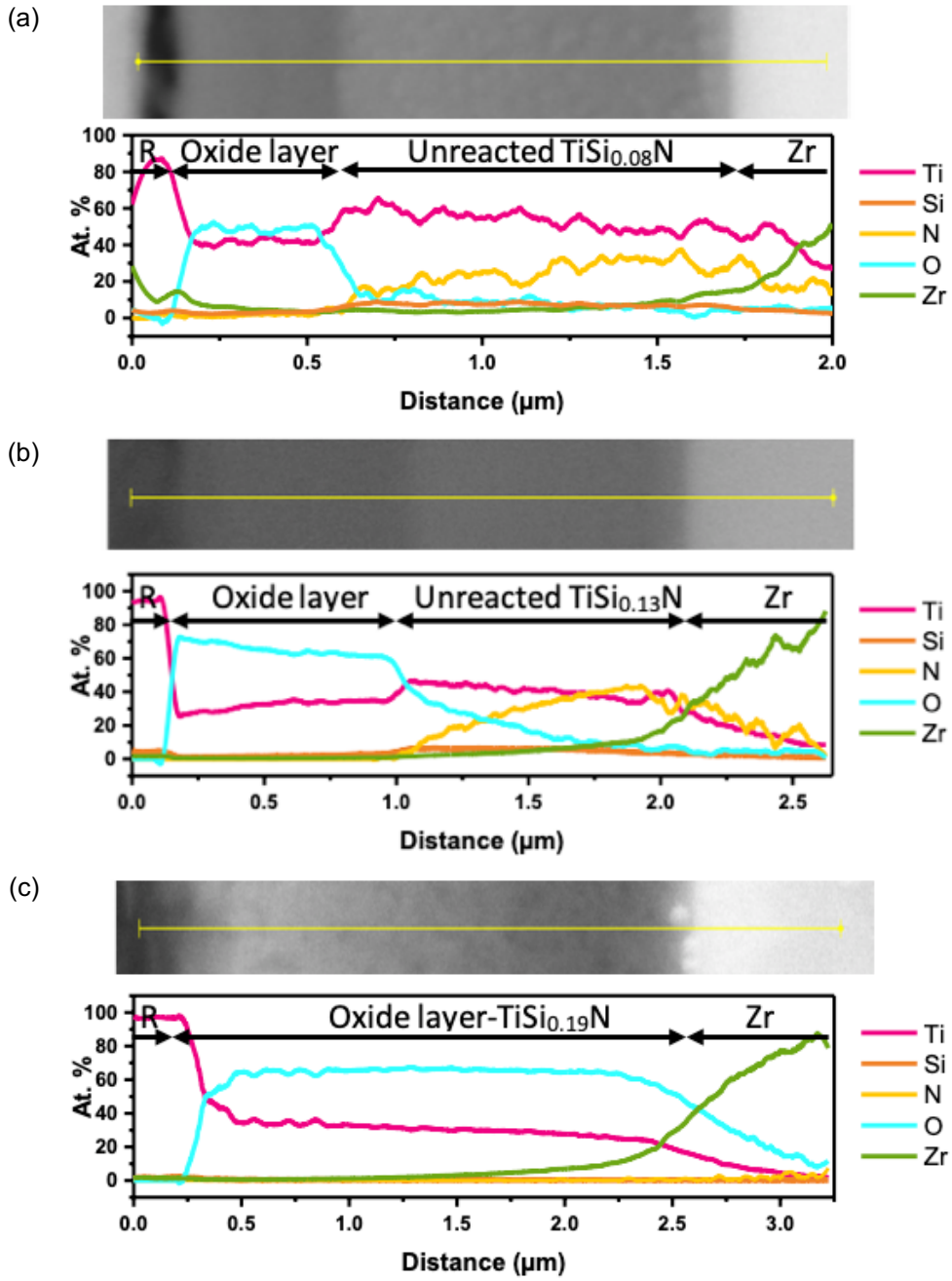

Figure 3-41 EDS line scan of 2 days autoclaved (a) $TiSi_{0.08}N$/Ti, (b) $TiSi_{0.13}N$/Ti and (c) $TiSi_{0.19}N$/Ti coatings

3.3.3.3. Morphology and elemental analysis after 2 days autoclave test

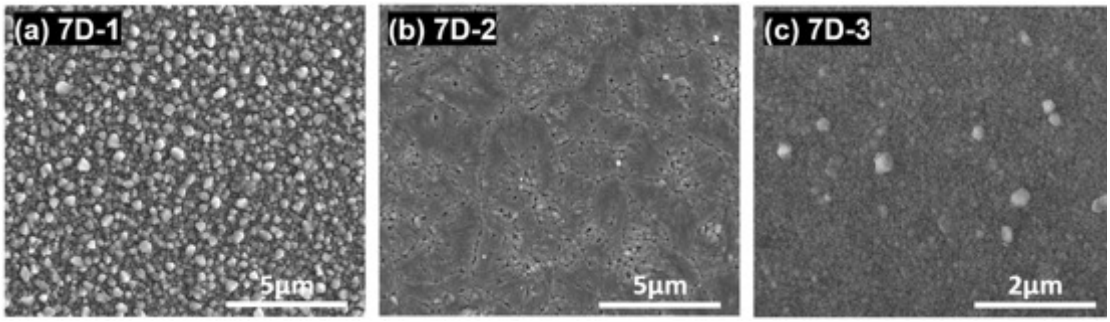

Figure 3-42 SEM images of (a) $TiSi_{0.08}N$/Ti, (b) $TiSi_{0.13}N$/Ti and (c) $TiSi_{0.19}N$/Ti coating surface morphology after 7 days autoclave test

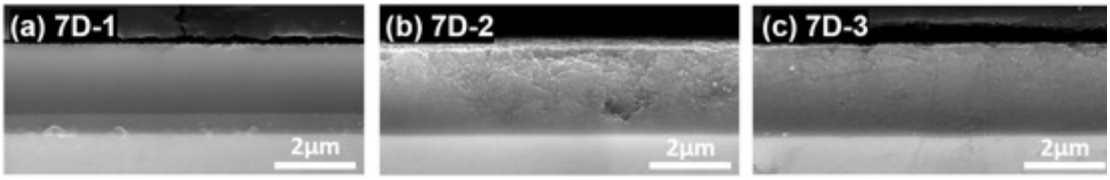

Figure 3-43 SEM polished cross-section images of (a) $TiSi_{0.08}N/Ti$, (b) $TiSi_{0.13}N/Ti$ and (c) $TiSi_{0.19}N/Ti$ coating after 7 days autoclave test

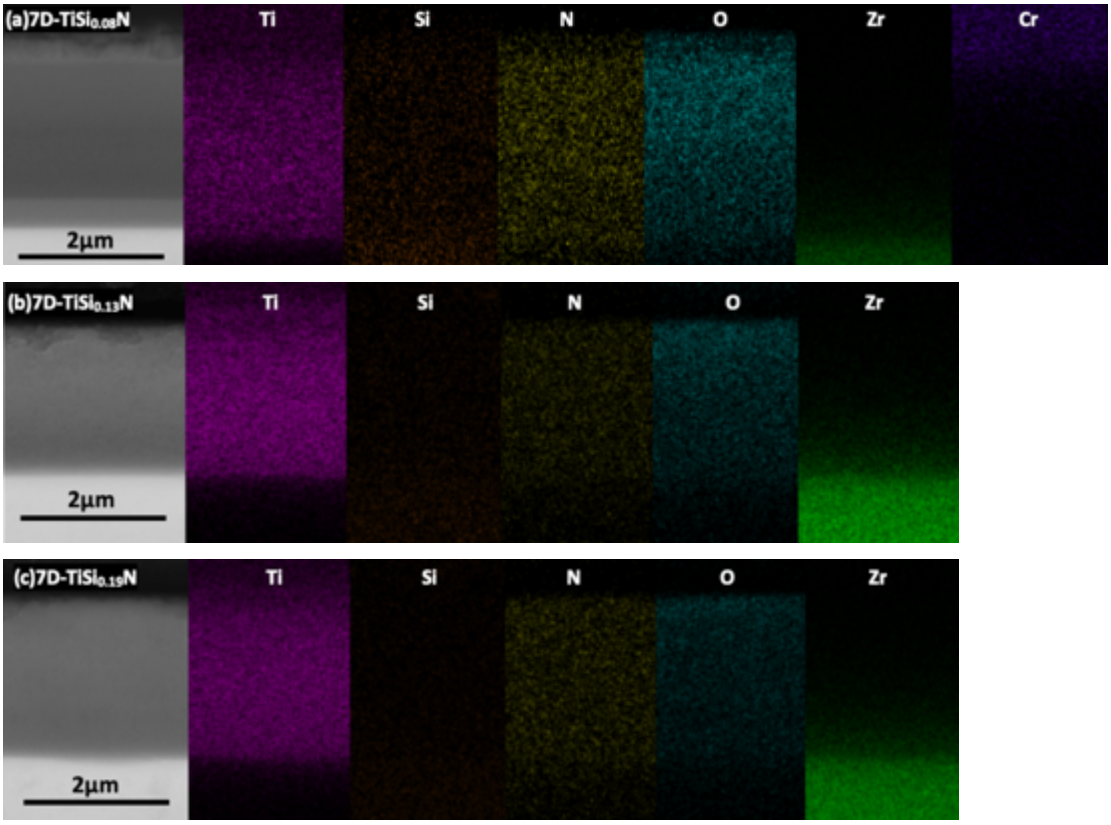

Figure 3-44 Cross-section SEM images and EDS mappings of (a) $TiSi_{0.08}N/Ti$, (b) $TiSi_{0.13}N/Ti$ and (c) $TiSi_{0.19}N/Ti$ after 7 days autoclave test

After 7 days of autoclave test, the surface morphology of each coating showed a significant difference (Figure 3-42). Crystalline particles were uniformly spread all over $TiSi_{0.08}N/Ti$ surface. As observed all surface area in $TiSi_{0.13}N/Ti$ after 7 days autoclave test, granular oxide particles were assembled as a large piece, with clear boundary among each piece. And the oxide particles were presented as the direction towards the centre of each piece and more porous at the centre. For $TiSi_{0.19}N/Ti$, nano-sized uniform oxide particles were formed on the surface, with several large crystal-like particles.

According to the cross-section images of 7 days autoclave tested samples (Figure 3-43), only $TiSi_{0.08}N/Ti$ coating showed two layers with the most dense structure, while $TiSi_{0.13}N$ and $TiSi_{0.19}N$ became fully oxide layer with porous structure. However, as analysed by EDS mapping, the double layered structure of $TiSi_{0.08}N/Ti$ seemed fully

oxidized as well. Si gradient could be seen from after 7-day autoclave tested $TiSi_{0.08}N$/Ti coating, but completely lost of Si in the other two coatings. Cr was detected on the surface of the corroded $TiSi_{0.08}N$/Ti surface, due to the stainless steel made autoclave. Also, diffusion between Zy-4 substrate and $TiSi_xN$/Ti could be observed from all three coatings EDS mappings. Based on the SEM cross-section and EDS mapping, it indicated that $TiSi_xN$ coatings were completely corroded after 7 days autoclave test.

3.3.3.4. Coating thickness change due to corrosion

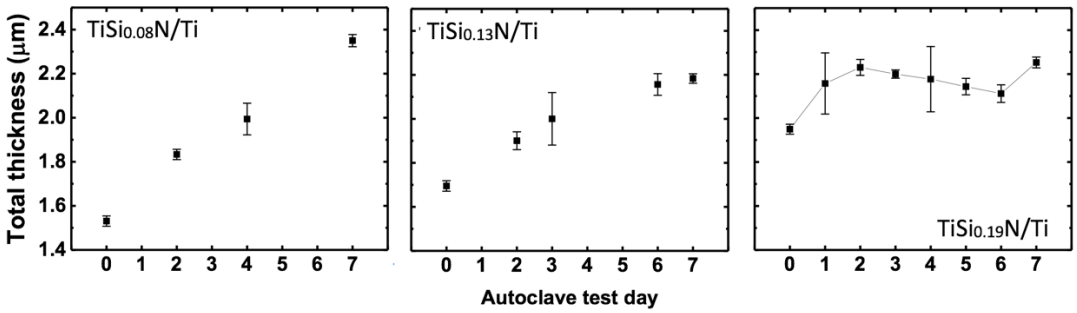

Figure 3-45 Thickness of TiSixN/Ti bilayer after autoclave immersion test

Figure 3-45 showed the thickness change as a function of days in autoclave immersion test. The measured thickness included the corroded oxide layer and the un-corroded $TiSi_xN$/Ti double layer structure. As we expected, the thickness growth occurred in all the immersion tested coatings. $TiSi_{0.08}N$/Ti showed a continuous increase in thickness through 7 days autoclave test, while $TiSi_{0.13}N$ and $TiSi_{0.19}N$ only showed increase in the first 6 days and 3 days. And it followed with decrease in thickness, especially $TiSi_{0.19}N$

During the investigation of this study, some of the tested $TiSi_xN$/Ti coatings, not displayed in the thickness profile, were found unreasonable increase and decrease in thickness with unpredictable contaminates layer formation covering all $TiSi_xN$ surface. Due to the covering contamination layer, the thickness of $TiSi_xN$ measured was not able to present the corrosion kinetics in autoclave immersion test. The SEM and EDS analysis showed the presence of well-grown crystal particles containing Cr and Al. It was due to the corrosion of the FeCrAl wire used to hang samples for immersion and stainless steel autoclave.

3.4. Corrosion mechanism

3.4.1. Si_3N_4 dissolution and volatilisation

$TiSi_xN$/Ti coatings in this study showed excellent water vapour resistance up to 1000°C. Only $TiSi_{0.08}N$/Ti contained the lowest Si fully oxidised in a porous structure after 4-hour steam test at 1000°C, which was consistent with previous studies. The optimal steam resistance of $TiSi_xN$ coating contained 13at% Si. However, the best composition of $TiSi_xN$ and the state of Si_3N_4 existence in $TiSi_xN$ coatings need further investigation.

Si_3N_4 was proved an excellent thermal-chemical corrosion resistance material up to 1200°C. [164] Water-containing environment degradation of Si_3N_4 was clarified as a simultaneous effect of oxidation and volatilisation. The chemical reactions of oxidation and volatilisation follows Equation 3-1 and Equation 3-2[164].

$$\boldsymbol{Si_3N_4(s) + 6H_2O(g) = 3SiO_2 + 2N_2(g) + 6H_2} \quad \text{Equation 3-1}$$

$$\boldsymbol{SiO_2(s) + 2H_2O(g) = Si(OH)_4(g)} \quad \text{Equation 3-2}$$

Apart from above results, autoclave immersion test showed aggressive damage to $TiSi_xN$/Ti coatings. Only $TiSi_{0.08}N$/Ti coating survived a thin layer after 7 days water attack. The corrosion product determined by XRD and SEM were porous nano-sized TiO_2, which meant $TiSi_xN$ coating could not bear water corrosion under this environment.

Similar conditions was discussed; dissolution happened at the amorphous grain boundary of hot pressed Si_3N_4 without additives. The crystalline Si_3N_4 grains were undermined and fall into water, which is so-called ‘inter-granular corrosion’. [165] The corrosion of Si_3N_4 was characterized as the inter-granular attack due to the selective dissolution of amorphous SiO_2 phase, as shown in Equation 3-3. [165] The corrosion mechanism of $TiSi_xN$ could explain as the dissolution of uniformly distributed nano-sized amorphous Si_3N_4 in water condition. The water first undermined amorphous Si_3N_4 located at TiN grain boundary and created interconnected pores. The porous interconnection was due to material loss, such as the dissolution of the SiO_2 corrosion product and formation of gas products (N_2 and H_2). The aggravated corrosion continued

due to the further interaction between water and $TiSi_xN$ coatings. The porous oxide formed after immersion test proved the above theory.

$$\boldsymbol{SiO_2 + OH^- = HSiO_3^-} \qquad \text{Equation 3-3}$$

According to the established thermodynamic data, the order of the Gibbs energy of TiO_2 is less than SiO_2, which means SiO_2 forms before TiO_2. However, despite TiO_2 characterised by GIXRD, no diffraction peaks of SiO_2 existed. This result showed agreement to the former dissolution and volatilisation mechanism.

4. Conclusion

In this thesis, an overview of zirconium alloy claddings in PWR, including its development, properties, and corrosion behaviours in normal coolant and high-temperature water vapour were introduced. New methods and new materials for ATF claddings were studied in recent years to enhance high-temperature water vapour resistance under LOCA. These studies were summarised with details of their advantages and disadvantages. In addition, ZrN single layer and TiSixN/Ti double layer coatings were deposited onto the Zr plate by the magnetron sputtering technique. High-temperature steam and autoclave pressurised water immersion tests were conducted to evaluate the corrosion resistance of coatings. Potential corrosion and failure mechanisms were discussed. The focus points were the coating structure, Si composition and test conditions which determined the adhesion, Si depletion and selective oxidation of coatings. Main conclusions were as follows:

1. Single layer structure (ZrN) coating failed in steam attack tests due to its poor adhesion with Zy-4 substrate and oxidation. Double layered TiSixN/Ti coatings significantly improved adhesion properties under both water vapour and autoclave immersion tests.
2. A significant contradiction between corrosion behaviours of TiSixN/Ti coatings under steam oxidation at high-temperature (LOCA condition) and water corrosion under autoclave immersion (PWR working condition) was found in this study. $TiSi_{0.13}N$/Ti coating could protect Zy-4 substrate from 1000°C steam for up to 4 hours, which could allow sufficient time for further action under accident conditions. However, all TiSixN/Ti was not able to provide corrosion resistance for Zy-4 claddings for 18 months in a PWR environment.
3. The oxidation resistance of magnetron sputtering $TiSi_xN$/Ti coatings was conditioned strictly by the presence of amorphous Si_3N_4. Dissolution of Si_3N_4 in water and volatilisation in high temperature water vapour led to loss of materials and protection.

In summary, for the purpose of designing ATF coatings in PWR claddings, $TiSi_xN$ coating could act as a steam resistant layer. However, its survival under pressurised water needs further investigation and modification.

5. Future work

Future research and development on ATF claddings design are a challenging topic, especially the corrosion resistance during light water coolant immersion as well as the LOCA. Based on this study, several interesting points are given for the deposition of TiSiN coatings and enhancement of corrosion behaviour.

Firstly, $TiSi_xN$ acting as ATF coating could provide corrosion resistance under high-temperature steam. TiSixN coating composition could be modified in order to survive longer in high temperature steam or higher steam temperature. Desired phase, such as TiN, could be reached by modifying parameters of magnetron sputtering technique. Amorphous Si_3N4 could be identified by Raman spectra or X-ray photoelectron spectroscopy (XPS). Transmission electron microscope (TEM) could be used to investigate atomic transportation and explore the combined corrosion mechanism of oxidation with volatilisation and dissolution.

Secondly, the corrosion mechanism of nitride ceramic coatings under high temperature steam and pressurized water conditions worth a deeper and thorough investigation. The difference of oxygen path in ceramic coatings under steam environment and pressurized water is an interesting topic. The difference between ceramic oxidation and its metal oxidation could be compared if the Pilling Bedworth ratio could give any explanation.

Thirdly, the hydrogen pick-up by fuel cladding has been well studied. Its associated embrittlement, hydride induced crack and stress corrosion cracking were concerned as important issues which could affect the durability of materials in PWR environment. The syngenetic effect of oxidation and hydrogen uptake of the coated system would be a subject worthy of study.

Thirdly, since $TiSi_xN$ could not survive in pressurised water, new materials could be further action to protect ATF $TiSi_xN$ layers through lifetime service in PWR. It suggests a triple-layered structure could be the next solution for ATF nitride ceramic coating design. Also, magnetron sputtering parameters could be modified to form gradient

composition between layers, which could ease the thermal mismatch during high temperature operation and cool down.

Reference

[1] Z. Karoutas *et al.*, “The maturing of nuclear fuel: Past to Accident Tolerant Fuel,” *Prog. Nucl. Energy*, vol. 102, pp. 1–11, 2017.

[2] Y. H. Lee and T. S. Byun, “A comparative study on the wear behaviors of cladding candidates for accident-tolerant fuel,” *J. Nucl. Mater.*, vol. 465, pp. 857–865, 2015.

[3] D. J. Park, H. G. Kim, Y. Il Jung, J. H. Park, J. H. Yang, and Y. H. Koo, “Behavior of an improved Zr fuel cladding with oxidation resistant coating under loss-of-coolant accident conditions,” *J. Nucl. Mater.*, vol. 482, pp. 75–82, 2016.

[4] S. J. Zinkle, K. A. Terrani, J. C. Gehin, L. J. Ott, and L. L. Snead, “Accident tolerant fuels for LWRs: A perspective,” *J. Nucl. Mater.*, vol. 448, no. 1–3, pp. 374–379, 2014.

[5] Y.-H. Koo, “KAERI’s Development of LWR Accident-Tolerant Fuel,” *Nucl. Technol.*, vol. 5450, no. October, 2014.

[6] Z. Duan *et al.*, “Current status of materials development of nuclear fuel cladding tubes for light water reactors,” *Nucl. Eng. Des.*, vol. 316, pp. 131–150, 2017.

[7] L. J. Ott, K. R. Robb, and D. Wang, “Erratum : Corrigendum to ‘preliminary assessment of accident-tolerant fuels on LWR performance during normal operation and under DB and BDB accident conditions’ (Journal of Nuclear Materials (2014) 448 (520-533)),” *J. Nucl. Mater.*, vol. 461, no. 1–3, pp. 178–179, 2015.

[8] H. G. Kim, I. H. Kim, Y. Il Jung, D. J. Park, J. Y. Park, and Y. H. Koo, “Adhesion property and high-temperature oxidation behavior of Cr-coated Zircaloy-4 cladding tube prepared by 3D laser coating,” *J. Nucl. Mater.*, vol. 465, pp. 531–539, 2015.

[9] H. G. Kim, J. H. Yang, W. J. Kim, and Y. H. Koo, “Development Status of Accident-tolerant Fuel for Light Water Reactors in Korea,” *Nucl. Eng. Technol.*, vol. 48, no. 1, pp. 1–15, 2016.

[10] J. Y. Park, I. H. Kim, Y. Il Jung, H. G. Kim, D. J. Park, and B. K. Choi, “High temperature steam oxidation of Al3Ti-based alloys for the oxidation-resistant surface layer on Zr fuel claddings,” *J. Nucl. Mater.*, vol. 437, no. 1–3, pp. 75–80, 2013.

[11] M. Nygren and Z. Shen, “On the preparation of bio-, nano- and structural ceramics and composites by spark plasma sintering,” *Solid State Sci.*, vol. 5, no. 1, pp. 125–131, 2003.

[12] K. Yueh and K. A. Terrani, “Silicon carbide composite for light water reactor fuel assembly applications,” *J. Nucl. Mater.*, vol. 448, no. 1–3, pp. 380–388, 2014.

[13] K. A. Terrani, S. J. Zinkle, and L. L. Snead, “Advanced oxidation-resistant iron-based alloys for LWR fuel cladding,” *J. Nucl. Mater.*, vol. 448, no. 1–3, pp. 420–435, 2014.

[14] I. Kim *et al.*, *TiN-based coatings on fuel cladding tubes for advanced nuclear reactors*, vol. 429, no. 1–3. Elsevier B.V., 2012.

[15] L. Hultman, “Thermal stability of nitride thin films,” *Vacuum*, vol. 57, no. 1, pp. 1–30, 2000.

[16] J. K. Shultis, *Fundamentals of Nuclear Science and Engineering*. 2009.

[17] “Nuclear power plants, world-wide, reactor types.” [Online]. Available: https://www.euronuclear.org/info/encyclopedia/n/npp-reactor-types.htm. [Accessed: 06-Dec-2017].

[18] “World Statistics - Nuclear Energy Institute.” [Online]. Available: https://www.nei.org/Knowledge-Center/Nuclear-Statistics/World-Statistics. [Accessed: 05-Dec-2017].

[19] F. Garzarolli and H. Stehle, “Behavior and Properties of Zircaloys in Power Reactors: A Short Review of Pertinent Aspects in LWR fuel,” *Zircon. Nucl. Ind. Elev. Int. Symp.*, pp. 12–32, 1996.

[20] M. Tupin *et al.*, “Hydrogen diffusion process in the oxides formed on zirconium alloys during corrosion in pressurized water reactor conditions,” *Corros. Sci.*, vol. 116, pp. 1–13, 2017.

[21] “Nuclear Power for Everybody - What is Nuclear Power.” [Online]. Available: http://www.nuclear-power.net/. [Accessed: 01-Nov-2017].

[22] “Principal design features of LWR fuel assemblies | CapitalEnergy.” [Online]. Available: http://capitalenergy.biz/?p=20563. [Accessed: 30-Nov-2017].

[23] P. C. I. James, “Surface modification techniques for increased corrosion tolerance of zirconium fuel cladding,” virginia commonwealth university, 2016.

[24] S. Suman, M. K. Khan, M. Pathak, R. N. Singh, and J. K. Chakravartty, “Hydrogen in Zircaloy: Mechanism and its impacts,” *Int. J. Hydrogen Energy*, vol. 40, no. 17, pp. 5976–5994, 2015.

[25] “Zircaloy-4(Alloy Zr4) (UNS R60804).” [Online]. Available: https://www.azom.com/article.aspx?ArticleID=7644. [Accessed: 04-Dec-2017].

[26] J.-Y. Park, T.-H. Na, T.-H. Lee, J.-H. Lee, B.-Y. Lee, and J.-S. Kim, “Effect of applied current on the formation of defect in PWR nuclear fuel rods in resistance pressure welding process,” *J. Nucl. Sci. Technol.*, vol. 52, no. 5, pp. 748–757, 2015.

[27] A. T. Motta, A. Couet, and R. J. Comstock, “Corrosion of Zirconium Alloys Used for Nuclear Fuel Cladding,” *Annu. Rev. Mater. Res.*, vol. 45, no. 1, pp. 311–343, 2015.

[28] G. Sabol, “ZIRLO™ — An Alloy Development Success,” *J. ASTM Int.*, vol. 2, no. 2, p. 12942, 2005.

[29] J. Wei *et al.*, “Autoclave study of zirconium alloys with and without hydride rim,” *Corros. Eng. Sci. Technol.*, vol. 47, no. 7, pp. 516–528, 2012.

[30] P. Bossis, D. Pêcheur, K. Hanifi, J. Thomazet, and M. Blat, “Comparison of the High Burn-Up Corrosion on M5 and Low Tin Zircaloy-4 BT - Comparison of the High Burn-Up Corrosion on M5 and Low Tin Zircaloy-4,” vol. 3, no. 1, pp. 1–32, 2006.

[31] G. P. Sabol, G. R. Kilp, M. G. Balfour, and E. Roberts, “Development of a Cladding Alloy for High Burnup,” *Zircon. Nucl. Ind. 8th Int. Symp. ASTM STP 1023*, pp. 227–244, 1989.

[32] J.-P. Mardon, D. Charquet, and J. Senevat, “Influence of Composition and Fabrication Process on Out-of-Pile and In-Pile Properties of M5 Alloy,” *Zircon. Nucl. Ind. Twelfth Int. Symp.*, pp. 505–524, 2000.

[33] V. Garat, D. Deuble, B. Dunn, and J.-P. Mardon, “Quantification of the margins provided by M5® cladding in accidental conditions,” 2012.

[34] T. Isobe, T. Murai, and Y. Mae, “Anodic Protection Provided by Precipitates in Aqueous Corrosion of Zircaloy,” *11th Int. Symp. Zr Nucl. Ind.*, vol. STP 1295, pp. 203–217, 1996.

[35] M. Billone, Y. Yan, T. Burtseva, and R. Daum, “NUREG/CR-6967: Cladding Embrittlement During Postulated Loss-of-Coolant Accidents,” p. 400, 2008.

[36] D. Charquet, R. Hahn, E. Ortlieb, J. P. Gros, and J. F. Wadier, “Solubility limits and formation of intermetallic precipitates in ZrSnFeCr alloys,” *Zircon. Nucl. Ind. Eighth Int. Symp.*, pp. 405–422, 1988.

[37] R. Meyer and R. Meyer, “United States Nuclear Regulatory Commission Technical Basis for Revision of Embrittlement Criteria in 10 CFR 50.46 Fuels-Cladding Behavior for Regulatory Applications,” 2006.

[38] P. K. Shukla, Y. Pan, R. Torres, T. Ahn, and P. Raynaud, “Assessment of Aging Mechanisms for Zirconium-Based High Burnup Fuel Cladding in Dry Storage Systems,” no. 8939, pp. 1–22.

[39] T. Arima, K. Moriyama, N. Gaja, H. Furuya, K. Idemitsu, and Y. Inagaki, “Oxidation kinetics of Zircaloy-2 between 450°C and 600°C in oxidizing atmosphere,” *J. Nucl. Mater.*, vol. 257, no. 1, pp. 67–77, 1998.

[40] B. Cox, J. P. Pemsler, and D. Bchantillons, “Diffusion of oxygen in growing zirconia films,” *J. Nucl. Mater.*, vol. 28, pp. 73–78, 1968.

[41] X. Ma, C. Toffolon-Masclet, T. Guilbert, D. Hamon, and J. C. Brachet, “Oxidation kinetics and oxygen diffusion in low-tin Zircaloy-4 up to 1523 K,” *J. Nucl. Mater.*, vol. 377, no. 2, pp. 359–369, 2008.

[42] B. Ensor, A. M. Lucente, M. J. Frederick, J. Sutliff, and A. T. Motta, “The role of hydrogen in zirconium alloy corrosion,” *J. Nucl. Mater.*, vol. 496, pp. 301–312, 2017.

[43] N. Ramasubramanian, “Localised electron transport in corroding zirconium alloys,” *J. Nucl. Mater.*, vol. 55, no. 2, pp. 134–154, 1975.

[44] M. Tupin, C. Bisor, P. Bossis, J. Chêne, J. L. Bechade, and F. Jomard, “Mechanism of corrosion of zirconium hydride and impact of precipitated hydrides on the Zircaloy-4 corrosion behaviour,” *Corros. Sci.*, vol. 98, pp. 478–493, 2015.

[45] S. S. Yardley *et al.*, “An investigation of the oxidation behaviour of zirconium alloys using isotopic tracers and high resolution SIMS,” *J. Nucl. Mater.*, vol. 443, no. 1–3, pp. 436–443, 2013.

[46] A. T. Motta *et al.*, “Microstructural Characterization of Oxides Formed on Model Zr Alloys Using Synchrotron Radiation,” *J. ASTM Int.*, vol. 5, no. 3, p. 101257, 2008.

[47] T. Ahmed and L. H. Keys, “The breakaway oxidation of zirconium and its alloys a review,” *J. Less-Common Met.*, vol. 39, no. 1, pp. 99–107, 1975.

[48] J. H. Baek and Y. H. Jeong, “Breakaway phenomenon of Zr-based alloys during a high-temperature oxidation,” *J. Nucl. Mater.*, vol. 372, no. 2–3, pp. 152–159, 2008.

[49] C. Duriez, T. Dupont, B. Schmet, and F. Enoch, “Zircaloy-4 and M5?? high temperature oxidation and nitriding in air,” *J. Nucl. Mater.*, vol. 380, no. 1–3, pp. 30–45, 2008.

[50] O. Coindreau, C. Duriez, and S. Ederli, “Air oxidation of Zircaloy-4 in the 600-1000 °c temperature range: Modeling for ASTEC code application,” *J. Nucl. Mater.*, vol. 405, no. 3, pp. 207–215, 2010.

[51] B. Cox, “Oxidation of Zirconium and its Alloys,” in *Advances in Corrosion Science and Technology*, 1976, pp. 173–391.

[52] A. M. Garde, “Enhancement of Aqueous Corrosion of Zircaloy-4 Due to Hydride Precipitation at the Metal-Oxide Interface,” *Zircon. Nucl. Ind. Ninth Int. Symp.*, pp. 566–594, 1991.

[53] L. Lanzani and M. Ruch, “Comments on the stability of zirconium hydride phases in Zircaloy,” *J. Nucl. Mater.*, vol. 324, no. 2–3, pp. 165–176, 2004.

[54] M. Amaya and T. Fuketa, “Effect of absorbed hydrogen on the stress corrosion cracking (SCC) susceptibility of unirradiated zircaloy cladding,” *J. Nucl. Sci. Technol.*, vol. 41, no. 11, pp. 1091–1099, 2004.

[55] S. A. Nikulin and A. B. Rozhnov, “Corrosion cracking of zirconium cladding tubes. A review. 2. Effect of external factors, structure, and properties of the alloys,” *Met. Sci. Heat Treat.*, vol. 47, no. 9–10, pp. 427–433, 2005.

[56] S. Suman, M. K. Khan, M. Pathak, and R. N. Singh, “Effects of hydrogen on thermal creep behaviour of Zircaloy fuel cladding,” *J. Nucl. Mater.*, vol. 498, pp. 20–32, 2018.

[57] Y. Nishino, A. R. Krauss, Y. Lin, and D. M. Gruen, “Initial oxidation of zirconium and zircaloy-2 with oxygen and water vapor at room temperature,” *J. Nucl. Mater.*, vol. 228, no. 3, pp. 346–353, 1996.

[58] M. Steinbrück, “Hydrogen absorption by zirconium alloys at high temperatures,” *J. Nucl. Mater.*, vol. 334, no. 1, pp. 58–64, 2004.

[59] W. Chen, L. Wang, and S. Lu, “Influence of oxide layer on hydrogen desorption from zirconium hydride,” *J. Alloys Compd.*, vol. 469, no. 1–2, pp. 142–145, 2009.

[60] A. Hermann, “Thermal behaviour of hydrogen in Zircaloy corrosion layers,” *J. Nucl. Mater.*, vol. 302, no. 2–3, pp. 217–219, 2002.

[61] T. Smith, “Kinetics and mechanism of hydrogen permeation of oxide films on zirconium,” *J. Nucl. Mater.*, vol. 18, no. 3, pp. 323–336, 1966.

[62] A. Couet, A. T. Motta, and R. J. Comstock, *Effect of Alloying Elements on Hydrogen Pickup in Zirconium Alloys*. 2015.

[63] A. Couet, A. T. Motta, and R. J. Comstock, “Hydrogen pickup measurements in zirconium alloys: Relation to oxidation kinetics,” *J. Nucl. Mater.*, vol. 451, no. 1–3, pp. 1–13, 2014.

[64] Areva Inc., “Advanced Cladding and Structural Material M5,” 2014.

[65] H. Okamoto, “H-Zr (Hydrogen-Zirconium),” *J. Phase Equilibria Diffus.*, vol. 27, no. 5, pp. 548–549, 2006.

[66] M. Harada, R. Wakamatsu, M. Limback, B. Kammenzind, and S. W. Dean, “The Effect of Hydrogen on the Transition Behavior of the Corrosion Rate of Zirconium Alloys,” *J. ASTM Int.*, vol. 5, no. 3, p. 101117, 2008.

[67] A. M. Garde, G. P. Smith, and R. C. Pirek, “Effects of hydride precipitate localization and neutron fluence on the ductility of irradiated Zircaloy-4,” *11th Int. Symp. Zr Nucl. Ind.*, vol. STP 1295, pp. 407–430, 1996.

[68] B.-C. Cheng, R. M. Kruger, and R. B. Adamson, “Corrosion behavior of Irradiated Zircloy,” *Zircon. Nucl. Ind. Tenth Int. Symp. ASTM STP 1245*, pp. 400–416, 1994.

[69] M. Blat and D. Noel, “Detrimental role of hydrogen on the corrosion rate of zirconium alloys,” *Zircon. Nucl. Ind. 11th Int. Symp. ASTM STP 1295*, pp. 319–335, 1996.

[70] R. Bossis and R. Iltis, “Multi-Scale Characterization of the Metal- Oxide Interface of Zirconium Alloys,” 2012.

[71] B. Hutchinson and B. Lehtinen, “A theory of the resistance of Zircaloy to uniform corrosion,” *J. Nucl. Mater.*, vol. 217, no. 3, pp. 243–249, 1994.

[72] G. . Sabol, R. J. Comstock, R. Weiner, P. Larouere, and R. . Stanutz, “In-reactor corrosion performance of ZIRLO and Zircaloy-4,” *Zircon. Nucl. Ind. Tenth Int. Symp.*, pp. 724–744, 1994.

[73] A. Rozhnov, V. Belov, S. Nikulin, and V. Khanzhin, “Stress corrosion cracking of zirconium cladding tubes: I. Proximate local SCC testing method,” *Russ. Metall.*, vol. 2010, no. 10, pp. 979–983, 2010.

[74] D. A. Powers and R. O. Meyer, “Cladding Swelling and Rupture Models for LOCA Analysis,” no. April, 1980.

[75] R. B. Rebak, “Alloy Selection for Accident Tolerant Fuel Cladding in Commercial Light Water Reactors,” *Metall. Mater. Trans. E*, vol. 2, no. 4, pp. 197–207, 2015.

[76] S. Leistikow and G. Schanz, “Oxidation kinetics and related phenomena of zircaloy-4 fuel cladding exposed to high temperature steam and hydrogen-steam mixtures under PWR accident conditions,” *Nucl. Eng. Des.*, vol. 103, no. 1, pp. 65–84, 1987.

[77] J. H. Baek and Y. H. Jeong, “Steam oxidation of Zr-1.5Nb-0.4Sn-0.2Fe-0.1Cr and Zircaloy-4 at 900-1200 ??C,” *J. Nucl. Mater.*, vol. 361, no. 1, pp. 30–40, 2007.

[78] K. M. McHugh, J. E. Garnier, S. Rashkeev, M. V. Glazoff, G. W. Griffith, and S. M. Bragg-Sitton, “High temperature steam corrosion of cladding for nuclear applications: Experimental,” *Ceram. Eng. Sci. Proc.*, vol. 34, no. 9, pp. 149–160, 2014.

[79] A. F. Brown and T. Healey, “The kinetics of total oxygen uptake in steam-oxidised zircaloy-2 in the range 1273-1673 K,” *J. Nucl. Mater.*, vol. 88, no. 1, pp. 1–6, 1980.

[80] J. H. Back, K. B. Park, and Y. H. Jeong, “Oxidation kinetics of Zircaloy-4 and Zr-1Nb-1Sn-0.1Fe at temperatures of 700-1200°C,” *J. Nucl. Mater.*, vol. 335, no. 3, pp. 443–456, 2004.

[81] L. Luo *et al.*, “Atomic origins of water-vapour-promoted alloy oxidation,” *Nat. Mater.*, vol. 17, no. 6, pp. 514–518, 2018.

[82] M. S. Veshchunov and A. V. Berdyshev, “Modelling of hydrogen absorption by zirconium alloys during high temperature oxidation in steam,” *J. Nucl. Mater.*, vol. 255, no. 2–3, pp. 250–262, 1998.

[83] M. S. Veshchunov and V. E. Shestak, “Models for hydrogen uptake and release kinetics by zirconium alloys at high temperatures,” *Nucl. Eng. Des.*, vol. 252, pp. 96–107, 2012.

[84] J. Carmack, “Accident tolerant fuel development program,” *Nucl. Plant J.*, vol. 32, no. 1, 2014.

[85] S. Massara, “A new NEA expert group on accident-tolerant fuels,” *NEA News*, no. 32, p. 27, 2014.

[86] “NRC: 10 CFR 50.46 Acceptance criteria for emergency core cooling systems for light-water nuclear power reactors.” [Online]. Available: https://www.nrc.gov/reading-rm/doc-collections/cfr/part050/part050-0046.html. [Accessed: 13-Feb-2019].

[87] D. O. Hobson and P. L. Rlttenhouse, “Embrittlement of Zircaloy-Clad Fuel Rods By Steam During Loca Transients,” Oak Ridge, Tennessee, 1972.

[88] D. O. Hobson, “DUCTILE-BRITTLE BEHAVIOR OF ZIRCALOY FUEL CLADDING,” Oak Ridge, Tennessee, 1973.

[89] C. P. Deck *et al.*, “Characterization of SiC-SiC composites for accident tolerant fuel cladding,” *J. Nucl. Mater.*, vol. 466, pp. 1–15, 2015.

[90] M. N. Gussev, T. S. Byun, Y. Yamamoto, S. A. Maloy, and K. A. Terrani, “In-situ tube burst testing and high-temperature deformation behavior of candidate materials for accident tolerant fuel cladding,” *J. Nucl. Mater.*, vol. 466, pp. 417–425, 2015.

[91] H. Yang *et al.*, “Hydrothermal corrosion behavior of SiCf/SiC composites candidate for PWR accident tolerant fuel cladding,” *Ceram. Int.*, vol. 44, no. 18, pp. 22865–22873, 2018.

[92] H. S. Edwards and K. M. Bohlander, “Seventh annual report - AEC Fuels and Materials Development: 10- Physico-chemical studies of Fe-Cr-Al-clad fuel systems,” no. 67, pp. 361–368, 1968.

[93] T. Cheng, J. R. Keiser, M. P. Brady, K. A. Terrani, and B. A. Pint, “Oxidation of fuel cladding candidate materials in steam environments at high temperature and pressure,” *J. Nucl. Mater.*, vol. 427, no. 1–3, pp. 396–400, 2012.

[94] H. Kim, H. Jang, G. Obulan Subramanian, C. Kim, and C. Jang, “Development of alumina-forming duplex stainless steels as accident-tolerant fuel cladding materials for light water reactors,” *J. Nucl. Mater.*, vol. 507, pp. 1–14, 2018.

[95] T. Hirose, K. Shiba, M. Enoeda, and M. Akiba, “Corrosion and stress corrosion cracking of ferritic/martensitic steel in super critical pressurized water,” *J. Nucl. Mater.*, vol. 367–370 B, no. SPEC. ISS., pp. 1185–1189, 2007.

[96] B. A. Pint, K. A. Unocic, K. A. Terrani, B. A. Pint, K. A. Unocic, and K. A. Terrani, “Effect of steam on high temperature oxidation behaviour of alumina-forming alloys Effect of steam on high temperature oxidation behaviour of alumina-forming alloys,” *Mater. High Temp.*, vol. 32:1-2, no. January, pp. 28–35, 2015.

[97] X. Wu, T. Kozlowski, and J. D. Hales, “Neutronics and fuel performance evaluation of accident tolerant FeCrAl cladding under normal operation conditions,” *Ann. Nucl. Energy*, vol. 85, pp. 763–775, 2015.

[98] Brent J.Heuser, T. Kozlowski, and X. Wu, “Engineered Zircaloy Cladding Modifications for Improved Accident Tolerance of LWR Fuel: A Summary,” *Proc. TopFuel 2013*, no. 12, pp. 56–58, 2013.

[99] H. K. Kim, H. G. Kim, J. H. Yang, and Y. H. Koo, “On the minimum thickness of FeCrAl cladding for accident-tolerant fuel,” *Nucl. Technol.*, vol. 198, no. 3, pp. 342–346, 2017.

[100] H. P. Qu, Y. P. Lang, C. F. Yao, H. T. Chen, and C. Q. Yang, “The effect of heat treatment on recrystallized microstructure, precipitation and ductility of hot-rolled Fe-Cr-Al-REM ferritic stainless steel sheets,” *Mater. Sci. Eng. A*, vol. 562, pp. 9–16, 2013.

[101] K. G. Field, S. A. Briggs, K. Sridharan, R. H. Howard, and Y. Yamamoto, “Mechanical properties of neutron-irradiated model and commercial FeCrAl alloys,” *J. Nucl. Mater.*, vol. 489, pp. 118–128, 2017.

[102] B. R. Maier, B. L. Garcia-Diaz, B. Hauch, L. C. Olson, R. L. Sindelar, and K. Sridharan, “Cold spray deposition of Ti2AlC coatings for improved nuclear fuel cladding,” *J. Nucl. Mater.*, vol. 466, pp. 1–6, 2015.

[103] D. J. Tallman, J. Yang, L. Pan, B. Anasori, and M. W. Barsoum, “Reactivity of Zircaloy-4 with Ti3SiC2 and Ti2AlC in the 1100-1300 °c temperature range,” *J. Nucl. Mater.*, vol. 460, pp. 122–129, 2015.

[104] H. Yeom, “High Temperature Corrosion and Heat Transfer Studies of Zirconium-Silicide Coatings for Light Water Reactor Cladding Applications By Hwasung Yeom A dissertation submitted in partial fulfillment of the requirements for the degree of Doctor of Philosophy (,” University of Wisconsin-Madison, 2017.

[105] P. I. B. J. Heuser, “Engineered Zircaloy Cladding Modifications for Improved Accident Tolerance of LWR Fuel,” *OECD/NEA Work. Accid. Toler. Fuels LWRs*, no. 12, p. 1, 2012.

[106] H. G. Kim *et al.*, “Out-of-pile performance of surface-modified Zr cladding for accident tolerant fuel in LWRs,” *J. Nucl. Mater.*, vol. 510, pp. 93–99, 2018.

[107] B. Heuser, “Engineered Zircaloy Cladding Modifications for Improved Accident Tolerance of LWR Nuclear Fuel,” no. 12.

[108] C. Tang, A. Jianu, M. Steinbrueck, M. Grosse, A. Weisenburger, and H. J. Seifert, “Influence of composition and heating schedules on compatibility of FeCrAl alloys with high-temperature steam,” *J. Nucl. Mater.*, vol. 511, pp. 496–507, 2018.

[109] Y. Wang *et al.*, “Behavior of plasma sprayed Cr coatings and FeCrAl coatings on Zr fuel cladding under loss-of-coolant accident conditions,” *Surf. Coatings Technol.*, vol. 344, no. October 2017, pp. 141–148, 2018.

[110] K. A. Terrani *et al.*, “Uniform corrosion of FeCrAl alloys in LWR coolant environments *,” *J. Nucl. Mater.*, vol. 479, pp. 36–47, 2016.

[111] J. C. Brachet *et al.*, “On-going studies at CEA on chromium coated zirconium based nuclear fuel claddings for enhanced Accident Tolerant LWRs Fuel,” *LWR Fuel Performance/TopFuel/WRFPM*, no. November, pp. 31–38, 2015.

[112] K. A. Terrani, C. M. Parish, D. Shin, and B. A. Pint, “Protection of zirconium by alumina- and chromia-forming iron alloys under high-temperature steam exposure,” *J. Nucl. Mater.*, vol. 438, no. 1–3, pp. 64–71, 2013.

[113] H. C. GRAHAM and H. H. DAVIS, “Oxidation/Vaporization Kinetics of Cr2O3,” *J. Am. Ceram. Soc.*, vol. 54, no. 2, pp. 89–93, 1971.

[114] J. H. J. yong Park, H. G. Kim, J. H. J. yong Park, Y. Il Jung, D. J. Park, and Y. H. Koo, “High temperature steam-oxidation behavior of arc ion plated Cr coatings for accident tolerant fuel claddings,” *Surf. Coatings Technol.*, vol. 280, pp. 256–259, 2015.

[115] H.-G. Kim, I.-H. Kim, J.-Y. Park, and Y.-H. Koo, “Application of Coating Technology on Zirconium-Based Alloy to Decrease High-Temperature Oxidation,” *Zircon. Nucl. Ind. 17th Vol.*, pp. 346–369, 2015.

[116] A. Rizzo, M. A. Signore, M. Penza, M. A. Tagliente, F. De Riccardis, and E. Serra, “RF sputtering deposition of alternate TiN/ZrN multilayer hard coatings,” *Thin Solid Films*, vol. 515, no. 2 SPEC. ISS., pp. 500–504, 2006.

[117] J. Zhang, Q. Xue, and S. Li, “Microstructure and corrosion behavior of TiC/Ti(CN)/TiN multilayer CVD coatings on high strength steels,” *Appl. Surf. Sci.*, vol. 280, pp. 626–631, 2013.

[118] I. Milošev, H.-H. Strehblow, and B. Navinšek, “Comparison of TiN, ZrN and CrN hard nitride coatings: Electrochemical and thermal oxidation,” *Thin Solid Films*, vol. 303, no. 1–2, pp. 246–254, 1997.

[119] A. A. Matei *et al.*, “Corrosion resistance appraisal of TiN, TiCN and TiAlN coatings deposited by CAE-PVD method on WC-Co cutting tools exposed to artificial sea water,” *Appl. Surf. Sci.*, vol. 358, pp. 572–578, 2015.

[120] Y. H. Yoo, D. P. Le, J. G. Kim, S. K. Kim, and P. Van Vinh, “Corrosion behavior of TiN, TiAlN, TiAlSiN thin films deposited on tool steel in the 3.5 wt.% NaCl solution,” *Thin Solid Films*, vol. 516, no. 11, pp. 3544–3548, 2008.

[121] E. Alat, A. T. Motta, R. J. Comstock, J. M. Partezana, and D. E. Wolfe, “Multilayer (TiN, TiAlN) ceramic coatings for nuclear fuel cladding,” *J. Nucl. Mater.*, vol. 478, pp. 236–244, 2016.

[122] M. J. Brova, E. Alat, M. A. Pauley, R. Sherbondy, A. T. Motta, and D. E. Wolfe, “Undoped and ytterbium-doped titanium aluminum nitride coatings for improved oxidation behavior of nuclear fuel cladding,” *Surf. Coatings Technol.*, vol. 331, no. April, pp. 163–171, 2017.

[123] F. Movassagh-Alanagh, A. Abdollah-zadeh, M. Aliofkhazraei, and M. Abedi, “Improving the wear and corrosion resistance of Ti–6Al–4V alloy by deposition of TiSiN nanocomposite coating with pulsed-DC PACVD,” *Wear*, vol. 390–391, no. March, pp. 93–103, 2017.

[124] J. H. Hsieh, A. L. K. Tan, and X. T. Zeng, “Oxidation and wear behaviors of Ti-based thin films,” *Surf. Coatings Technol.*, vol. 201, no. 7 SPEC. ISS., pp. 4094–4098, 2006.

[125] N. D. Nam, M. J. Kim, D. S. Jo, J. G. Kim, and D. H. Yoon, “Corrosion protection of Ti/TiN, Cr/TiN, Ti/CrN, and Cr/CrN multi-coatings in simulated proton exchange membrane fuel cell environment,” *Thin Solid Films*, vol. 545, pp. 380–384, 2013.

[126] Q. Wan *et al.*, "Corrosion behaviors of TiN and Ti-Si-N (with 2.9 at.% and 5.0 at.% Si) coatings by electrochemical impedance spectroscopy," *Thin Solid Films*, vol. 616, pp. 601–607, 2016.

[127] C. L. Chang, C. Te Lin, P. C. Tsai, W. Y. Ho, W. J. Liu, and D. Y. Wang, "Mechanical and corrosion properties of (Ti,Si)N coating synthesized by cathodic arc plasma evaporation," *Surf. Coatings Technol.*, vol. 202, no. 22–23, pp. 5516–5520, 2008.

[128] X. Zhao, D. Yan, S. Li, and C. Lu, "The effect of heat treatment on the electrochemical corrosion behavior of reactive plasma-sprayed TiN coatings," *Appl. Surf. Sci.*, vol. 257, no. 23, pp. 10078–10083, 2011.

[129] T. Liu, C. Dong, S. Wu, K. Tang, J. Wang, and J. Jia, "TiN, TiN gradient and Ti/TiN multi-layer protective coatings on Uranium," *Surf. Coatings Technol.*, vol. 201, no. 15, pp. 6737–6741, 2007.

[130] H. Elmkhah, F. Attarzadeh, A. Fattah-alhosseini, and K. H. Kim, "Microstructural and electrochemical comparison between TiN coatings deposited through HIPIMS and DCMS techniques," *J. Alloys Compd.*, vol. 735, pp. 422–429, 2018.

[131] J. Vega, H. Scheerer, G. Andersohn, and M. Oechsner, "Experimental studies of the effect of Ti interlayers on the corrosion resistance of TiN PVD coatings by using electrochemical methods," *Corros. Sci.*, vol. 133, no. December 2017, pp. 240–250, 2018.

[132] E. B. Kashkarov *et al.*, "Hydrogenation behavior of Ti-implanted Zr-1Nb alloy with TiN films deposited using filtered vacuum arc and magnetron sputtering," *Appl. Surf. Sci.*, vol. 432, pp. 207–213, 2018.

[133] N. D. Nam, M. Vaka, and N. Tran Hung, "Corrosion behavior of TiN, TiAlN, TiAlSiN-coated 316L stainless steel in simulated proton exchange membrane fuel cell environment," *J. Power Sources*, vol. 268, pp. 240–245, 2014.

[134] V. Chawla, R. Jayaganthan, and R. Chandra, "A study of structural and mechanical properties of sputter deposited nanocomposite Ti-Si-N thin films," *Surf. Coatings Technol.*, vol. 204, no. 9–10, pp. 1582–1589, 2010.

[135] A. Flink, *Growth and Characterization of Ti-Si-N Hard Coatings*, no. 1270. 2006.

[136] D. Li *et al.*, "Effect of Cr interlayer on the adhesion and corrosion enhancement of nanocomposite TiN-based coatings deposited on stainless steel 410," *Thin Solid Films*, vol. 519, no. 10, pp. 3128–3134, 2011.

[137] F. Movassagh-Alanagh, A. Abdollah-zadeh, M. Asgari, and M. A. Ghaffari, "Influence of Si content on the wettability and corrosion resistance of nanocomposite TiSiN films deposited by pulsed-DC PACVD," *J. Alloys Compd.*, vol. 739, pp. 780–792, 2018.

[138] F. Vaz *et al.*, "Characterisation of Ti1−xSixNy nanocomposite films," *Surf. Coatings Technol.*, vol. 133–134, pp. 307–313, 2000.

[139] S. Veprek and A. S. Argon, "Towards the understanding of mechanical properties of super- and ultrahard nanocomposites," *J. Vac. Sci. Technol. B Microelectron. Nanom. Struct.*, vol. 20, no. 2, p. 650, 2002.

[140] K. Moto, T. Bolom, and S. Veprek, "The Role of nc-TiN Surface Coverage by a-Si_3N_4 for the Control of Room Temperature and In-Dry-Air Oxidation Resistance of nc-TiN/a-Si_3N_4/a- and nc-$TiSi_2$ Nanocomposites," *Mater. Sci. Forum*, vol. 437–438, pp. 403–406, 2003.

[141] F. Khatkhatay *et al.*, "Superior corrosion resistance properties of TiN-based coatings on Zircaloy tubes in supercritical water," *J. Nucl. Mater.*, vol. 451, no. 1–3, pp. 346–351, 2014.

[142] E. B. Kashkarov, O. V. Vilkhivskaya, and S. A. Zakharchenko, “Thermal stability and hydrogenation behavior of Zr-1Nb alloy with TiNxand Ti/TiNxcoatings,” *J. Phys. Conf. Ser.*, vol. 741, no. 1, 2016.

[143] “Zirconium, Zr.” [Online]. Available: http://www.matweb.com/search/DataSheet.aspx?MatGUID=6e8936b3ad994f13bfb29923cc1506a9. [Accessed: 18-Jun-2019].

[144] H. Kim, J. Yang, W. Kim, and Y. Koo, “Development Status of Accident-tolerant Fuel for Light Water Reactors in Korea,” vol. 8, pp. 1–15, 2015.

[145] J. C. Brachet *et al.*, “CEA studies on advanced nuclear fuel claddings for enhanced Accident Tolerant LWRs Fuel(LOCA and beyond LOCA conditions),” *FONTEVRAUD 8-Contrib. Mater. Investig. Oper. Exp. to LWRs’ Safety, Perform. Reliab.*, no. September, p. 10, 2014.

[146] R. Ananthakumar, B. Subramanian, A. Kobayashi, and M. Jayachandran, “Electrochemical corrosion and materials properties of reactively sputtered TiN/TiAlN multilayer coatings,” *Ceram. Int.*, vol. 38, no. 1, pp. 477–485, 2012.

[147] D. Zhou, H. Peng, L. Zhu, H. Guo, and S. Gong, “Microstructure, hardness and corrosion behaviour of Ti/TiN multilayer coatings produced by plasma activated EB-PVD,” *Surf. Coatings Technol.*, vol. 258, pp. 102–107, 2014.

[148] J. Braun *et al.*, “Chemical compatibility between UO2 fuel and SiC cladding for LWRs. Application to ATF (Accident-Tolerant Fuels),” *J. Nucl. Mater.*, vol. 487, pp. 380–395, 2017.

[149] Y. Katoh and K. A. Terrani, *Systematic Technology Evaluation Program for SiC/SiC Composite-Based Accident-Tolerant LWR Fuel Cladding and Core Structures, ORNL/TM-2015/454*, no. August. 2015.

[150] Y. Katoh *et al.*, “Current status and recent research achievements in SiC/SiC composites,” *J. Nucl. Mater.*, vol. 455, no. 1–3, pp. 387–397, 2014.

[151] P. J. Kelly *et al.*, “Comparison of the tribological and antimicrobial properties of CrN/Ag, ZrN/Ag, TiN/Ag, and TiN/Cu nanocomposite coatings,” *Surf. Coatings Technol.*, vol. 205, no. 5, pp. 1606–1610, 2010.

[152] P. J. Kelly, H. Li, K. A. Whitehead, J. Verran, R. D. Arnell, and I. Iordanova, “A study of the antimicrobial and tribological properties of TiN/Ag nanocomposite coatings,” *Surf. Coatings Technol.*, vol. 204, no. 6–7, pp. 1137–1140, 2009.

[153] P. J. Kelly, T. vom Braucke, Z. Liu, R. D. Arnell, and E. D. Doyle, “Pulsed DC titanium nitride coatings for improved tribological performance and tool life,” *Surf. Coatings Technol.*, vol. 202, no. 4–7, pp. 774–780, 2007.

[154] S. Guha, S. Das, A. Bandyopadhyay, S. Das, and B. P. Swain, “Investigation of structural network and mechanical properties of Titanium silicon nitride (TiSiN) thin films,” *J. Alloys Compd.*, vol. 731, pp. 347–353, 2018.

[155] B. hee Park, Y. Kim, and kwang ho Kim, “Effect of silicon addition on microstructure and mechanical property of titanium nitride film prepared by plasma-assisted chemical vapor deposition,” *Thin Solid Films*, vol. 348, no. 1, pp. 210–214, 1999.

[156] D. Pilloud, J. F. Pierson, P. Steyer, A. Mege, B. Stauder, and P. Jacquot, “Use of silane for the deposition of hard and oxidation resistant Ti-Si-N coatings by a hybrid cathodic arc and chemical vapour process,” *Mater. Lett.*, vol. 61, no. 11–12, pp. 2506–2508, 2007.

[157] I. Park, K. H. Kim, and M. Lee, “Role of Amorphous Si 3 N 4 in the Microhardness of Ti-Al-Si-N Nanocomposite Films,” vol. 42, no. 6, pp. 783–786, 2003.

[158] H. Oettel, R. Wiedemann, and S. Preißler, “Residual stresses in nitride hard coatings prepared by magnetron sputtering and arc evaporation,” *Surf. Coatings Technol.*, vol. 74–75, no. PART 1, pp. 273–278, 1995.

[159] C. S. Kumar and S. K. Patel, “Performance analysis and comparative assessment of nano-composite TiAlSiN/TiSiN/TiAlN coating in hard turning of AISI 52100 steel,” *Surf. Coatings Technol.*, vol. 335, no. September 2017, pp. 265–279, 2018.

[160] S. H. Kim, J. K. Kim, and K. H. Kim, “Influence of deposition conditions on the microstructure and mechanical properties of Ti-Si-N films by DC reactive magnetron sputtering,” *Thin Solid Films*, vol. 420–421, pp. 360–365, 2002.

[161] M. Steinbrück, N. Vér, and M. Groe, “Oxidation of advanced zirconium cladding alloys in steam at temperatures in the range of 600-1200 °c,” *Oxid. Met.*, vol. 76, no. 3–4, pp. 215–232, 2011.

[162] H. El Kadiri *et al.*, “Transformations and cracks in zirconia films leading to breakaway oxidation of Zircaloy,” *Acta Mater.*, vol. 61, no. 11, pp. 3923–3935, 2013.

[163] S. Leistikow and S. G. Schanz, “The oxidation behavior of Zircaloy-4 in steam between 600 and 1600°C,” *Mater. Corros.*, vol. 36, no. 3, pp. 105–116, 1985.

[164] X. Hou, E. Wang, B. Li, J. Chen, and K. C. Chou, “Corrosion behavior of porous silicon nitride ceramics in different atmospheres,” *Ceram. Int.*, vol. 43, no. 5, pp. 4344–4352, 2017.

[165] K. Oda, T. Yoshio, Y. Miyamoto, and M. Koizumi, “Hydrothermal Corrosion of Pure, Hot Isostatically Pressed Silicon Nitride,” *J. Am. Ceram. Soc.*, vol. 76, no. 5, pp. 1365–1368, 1993.